HEAT TRANSFER AND FLUID FLOW BEHAVIOR OF NANOPARTICLE DISPERSIONS IN VOLUMETRICALLY HEATED SOLAR THERMAL SYSTEMS

A Thesis submitted in partial fulfillment of the requirements for the award of degree of

Doctor of Philosophy

By

Apoorva Singh
(Registration No.: 951608005)

Under the guidance of

Dr. Vikrant Khullar
Department of Mechanical Engineering,
T.I.E.T., Patiala

&

Dr. Manish Kumar
Mechanical Engineering Department,
MNIT Jaipur

Department of Mechanical Engineering
Thapar Institute of Engineering & Technology
(Deemed to be University)
Patiala – 147004, Punjab (India)
www.thapar.edu

October, 2023

To my friends and family.
To my teachers from school, college and University who always inspired me.

Contents

Certificate

This is to certify that the thesis entitled **"Heat Transfer and Fluid Flow Behavior of Nanoparticle Dispersions in Volumetrically Heated Solar Thermal Systems"** being submitted by Miss Apoorva Singh to Department of Mechanical Engineering, Thapar Institute of Engineering & Technology (Deemed to be University), Patiala for the award of degree of Doctor of Philosophy, is a record of bonafide research work carried out by him under my guidance and supervision and has fulfilled the requirements for the submission of this thesis, which to my knowledge has reached the requisite standard.

The results embodied in the thesis have not been submitted in part or full to any other University or Institute for the award of any degree or diploma.

Dr. Vikrant Khullar
Associate Professor
Department of Mechanical Engineering,
Thapar Institute of Engineering &
Technology (Deemed to be University), Patiala, India

Dr. Manish Kumar
Assistant Professor
Department of Mechanical Engineering,
MNIT, Jaipur, India

Acknowledgements

A Ph.D. is a long, sometimes onerous, other times enthralling but mostly a lonely journey. The relentless pursuit of the completion of *objectives* that we choose in the first year of the program can become overwhelming on some days even for the most resilient of us. And it is on those days, that the weight of hordes of inconveniences around us comes bearing down upon us. It is also on such days that one needs to rest and replenish, reconnect with the bigger picture. And that is when we need people close to us to empathize and remind us that tomorrow is a new day. I am thankful to people around me without whose guidance, support and *love* it would not have been possible for me to accomplish the completion of my thesis.

First and foremost, I am deeply indebted to my Ph.D. supervisors, Dr. Vikrant Khullar and Dr. Manish Kumar. It is said that choosing a Ph.D. supervisor is a very important step as throughout one's career, one emulates his/her supervisor in all their dealings. And I think I have been very lucky in this aspect. My supervisors have been a constant source of motivation for me through my journey. They have encouraged and supported me to go beyond my own limits as a researcher and explore and cross newer and newer limits of my potential. Everyone comes to a point during their research where you feel skeptical and unsure about what needs to be done. The sight of new equations becomes dreadful and at such critical times for me, it was their tenacity at still being able to see the big picture and their ability to offer crucial insights into minute details of any problem that I was stuck with that got me through. As someone who had the chance to work with them so early in my career in research, I consider myself extremely fortuitous.

I would like to express my deepest appreciation to the members of my doctoral committee, Prof. Tarun Kumar Bera, Dr. Madhup Mittal, Dr. Rohit Kumar Singla and Dr. Raj Kumar Gupta at Thapar Institute of Engineering and Technology for providing guidance and motivation throughout the span of my doctorate. I am grateful to the staff and faculty members at Thapar for their assistance in navigating through my day-to-day responsibilities as a teaching associate and a doctoral scholar. I gratefully acknowledge the financial support given by Department of Science and Technology – Science and Engineering Research Board (Sanction order no. CRG/2021/003272). I want to especially thank my family and friends for their love, support, and patience throughout my Ph.D. journey.

I am grateful for being provided with the opportunity to work in solar energy. Delving deeper into the numerical aspects of physical systems has taught me to appreciate the power of mathematics to give voice to the inanimate. I have learnt that however chaotic a physical system may appear in the beginning, a trend emerges once it's peered through, helping us understand why things are the way they are. And this understanding is a source of joy one can live off for a while.

I want to acknowledge the work of all scientists and researchers who dedicate their lives towards the betterment of human life through their endeavors and whose ideals and unyielding efforts have and always shall serve as a beacon light guiding me.

Finally, I am filled with overwhelming gratitude for my Higher Power for taking care of me in *surprising and simple ways* on this journey.

Apoorva Singh

Abstract

This thesis studies the role that volumetric absorption-based systems can play in efficiency enhancement of incumbent solar thermal technologies. Solar energy is considered as the most abundant renewable energy resource, but it accounts for only ~0.04 % of total energy demand globally due to low efficiencies and high costs compared to fossil-fuel based technologies. Currently, solar thermal systems employ surface absorption-based systems in which the surface gets heated and in turn heats up the working fluid flowing inside it. However, these systems suffer from low efficiencies due to high radiative and convective losses. Volumetric systems in which solar radiation is captured by allowing radiation to transmit through a transparent glass such that it interacts directly with the working fluid promise higher efficiencies as losses from the surface of the receiver are considerably reduced. However, studies catering to the employment of such systems in solar thermal technologies are relatively few. The phenomenon of direct volumetric absorption of radiation by the nanofluid and redistribution of the absorbed energy within the nanofluid has been critically analyzed. In particular, transport phenomena in two different flow situations have been considered: firstly, *'transport phenomena in channel flow'* wherein fluid is made to flow through a rectangular channel and at the same time it interacts directly and volumetrically with the incident solar irradiation. Secondly, *'transport phenomena in cavity flow'* wherein direct volumetric interaction of the solar irradiation induces fluid flow in the closed cavity.

A comprehensive theoretical modeling framework was devised to study these systems and investigate the role of pertinent parameters for both cases (forced and natural convection) strictly in the laminar regime. The study of volumetrically heated channels (forced convection) considers the effect of the Reynolds number of flow, the solar concentration ratio, inlet temperature of the fluid, optical properties of the fluid in the cavity and the nature of enveloping surfaces such as glass, heat mirror etc. and compares their performance to channels where energy is supplied through surface heating. Performance characteristics reveal that particularly at high solar concentration ratios, volumetric absorption-based receivers could have 45%–51% higher thermal efficiencies compared to their surface absorption-based counterparts. Further, this could translate into a significant increase (by 15%–18%) in overall energy conversion efficiency of concentrated solar power plants.

The parametric study of volumetrically heated cavities (natural convection) considers two orientations of incident flux: (a). cavities heated from side and (b). cavities heated from bottom, and investigates the effect of Rayleigh, Prandtl and Biot numbers, the optical thickness of the fluid, the aspect ratio of the cavity and linearly varying flux. The concept of heatlines has been extended to this study and the following were the key observations of the study: (1). the existence of regimes (conduction and convection-dominated) is identified for both orientations (side and bottom-heating); in convection-dominated regimes the pattern of heatlines begins to resemble that of the streamlines; (2). nature of the flux distribution (uniformly distributed vs linearly varying) at the transmitting wall can significantly impact the temperature distribution and (3). there exist optimum values of optical thickness (for various Rayleigh numbers), which ensure minimum heat loss and maximum useful energy gain in these systems"

Overall, through the present work key design and operational parameters have been deciphered while quantifying their impact on the performance of volumetrically heated systems especially pertaining to their role in solar thermal technologies.

However, the applications of this work are not limited to solar thermal systems alone. The study of fluid filled enclosures leads us to a better understanding of the environment around us – the natural circulation of the atmosphere enveloping our planet, the circulation of ocean currents, and the movement of the molten core beneath the surface of Earth's crust, can all be studied by choosing an appropriate system.

List of Figures

List of Tables

1. Introduction

The most recent report by Intergovernmental panel on climate change (IPCC, 2023) has shown that human activities have led to the increase of 1.1°C global surface temperatures in the decade from 2011-2020 as compared to1850-1900 principally due to the emission of greenhouse gases. This human-caused climate change has led to widespread and rapid changes throughout the Earth's atmosphere, oceans, cryosphere, and biosphere and is affecting extreme weather conditions across the globe. The unabated rise in greenhouse emissions will lead to increased global warming which is best estimated to increase up to 1.5°C and even this incremental change will intensify multiple and concurrent hazards. Adaptation options which are feasible and effective today will become less and less so with increased warming and we will soon reach our adaptation limits. To limit human-caused global warming, we need net zero CO_2 emissions. The time it takes for us to reach net zero carbon emissions will determine whether we are able to limit the warming to 1.5°C or 2°C.

We need an urgent response because the window of opportunity is rapidly closing for us to secure a livable and sustainable future. One of the ways to reduce greenhouse gas emissions is using renewable energy sources instead of fossil fuels. As per IEA (International Energy Agency) estimates, currently, approximately 82% of the total energy demand is met through fossil fuels (i.e. oil, natural gas, and coal) (IEA, 2013). In this context, solar energy is considered as the most abundant renewable energy resource. Currently, solar energy accounts for only ~0.04 % of total energy demand globally due to low efficiencies and high costs relative to fossil-fuel based technologies (IEA 2013, 2019). One of the most efficient practices in the domain of solar energy harvesting is the use of the concentrated solar thermal technologies. In this, the surface (solar selective/black) absorbs the concentrated solar radiation, and subsequently transfers the absorbed energy to the fluid flowing underneath. While this mechanism is efficient at converting incident radiation to thermal energy, it does not efficiently transfer this energy to the heat carrying fluid due to thermal resistance between the surface and the fluid thereby limiting the transfer rate of energy. In addition, since the surface temperatures are high, large energy loss is incurred in the form of radiative losses. These limitations could be addressed by using volumetric absorption-based receivers (VARs) where sunlight is directly (and volumetrically) absorbed as well as transported directly by the working fluid without the need of an intervening surface. This work focuses on the

improvement of efficiency of solar thermal collectors using volumetric receivers. Figure 1.1 shows a schematic comparing surface absorption-based receivers to volumetric ones. The design and construction of volumetric systems is like that of surface absorption-based systems. Instead of an opaque absorbing surface (black or solar selective); there is transmitting glass which is transparent in the solar wavelength band (i.e., generally glass) - allowing the sunlight to interact directly with the working fluid. Also, these systems may have enveloping surfaces (glass or transparent heat mirrors) to reduce thermal losses.

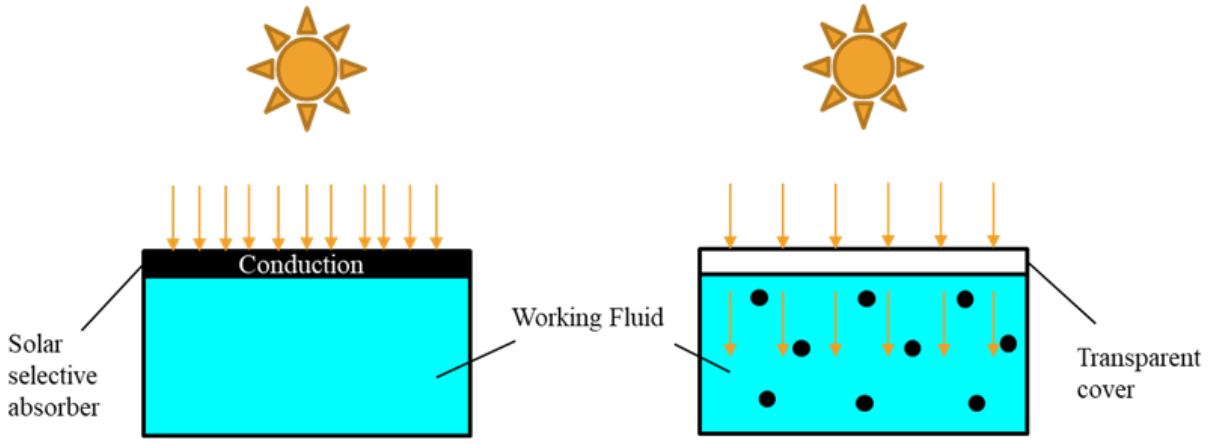

Fig. 1.1: Schematic showing the difference between surface based versus volumetric absorption based solar collectors.

1.1 Thesis Aims

Figure 1.2 shows solar thermal systems operating across the globe using surface absorption-based systems while volumetric systems are still being studied. As can be seen from the figure, these systems have different geometries and operate in a wide range of operating conditions. This thesis examines surface absorption-based and volumetric systems through mathematical modeling and attempts to answer how much better volumetric systems perform over surface absorption-based systems, and under different operating conditions and geometries. The temperature and flow distribution in these systems in different regimes has also been closely investigated. The objectives of this thesis are listed below:

1. Development of a detailed theoretical modeling framework to predict the temperature and flow fields in nanoparticle dispersion based volumetrically heated systems with natural and forced convection.

2. To identify the key operating parameters, thermo-physical and optical properties which impact the heat transfer and fluid flow behavior in these volumetrically heated systems.

3. To validate the developed theoretical model and compare the performance of different volumetrically heated systems.

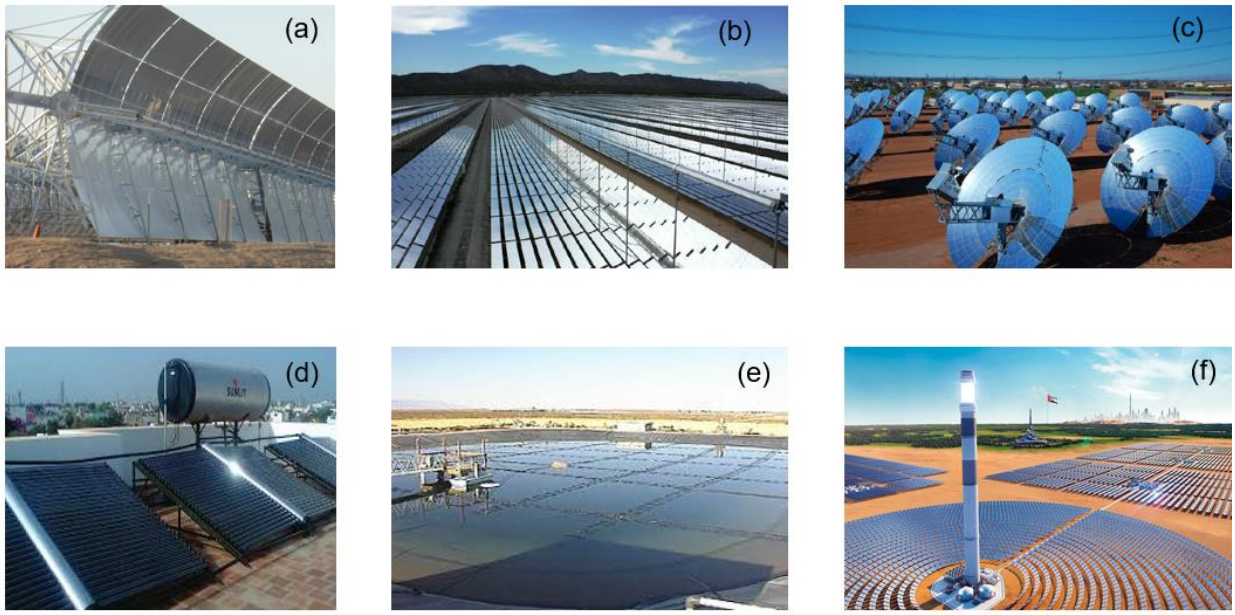

Fig. 1.2: Solar thermal systems operating across the world (a) Parabolic trough, at a plant near Harper Lake, California[1] (b). Linear Fresnel reflector in Spain[2] (c). Parabolic dish collectors in Arizona, USA[2] (d). Evacuated tube collectors in India[3] (e). Solar energy pond in El Paso, Texas[4] (f). Solar power tower in Dubai[5].

[1]https://commons.wikimedia.org/w/index.php?curid=27881587

[2]Taylan, Onur, and Halil Berberoglu. "Fuel production using concentrated solar energy." *Application of solar energy* (2013): 33-67.

[3]https://www.focusunsolar.co.in/evacuated-tube-collector-commercial-solar-water-heater.htm

[4]http://windenergy7.com/turbines/tag/solar-pond/

[5]https://cosmosmagazine.com/technology/solar-power-tower-csp-australia-magazine/

1.2 Thesis Plan

The rest of this thesis is structured into chapters as follows:

- *Chapter 2: Background:* It reviews existing literature germane to direct volumetric absorption systems which provides the necessary information to highlight the novelty and significance of the present work.
- *Chapter 3: Methodology:* It contains the mathematical framework employed to simulate the fluid and heat flow in the systems (of various geometries) subject to different boundary and operating conditions.
- *Chapter 4: Results & Discussion:* It presents the results obtained from modelling various systems which include the temperature and flow distributions and how they vary depending on the values of different governing parameters. The obtained results are analyzed to evaluate optimum designs for solar thermal systems employing volumetric heating.
- *Chapter 5: Conclusions and Future Scope:* It brings together the work presented in previous chapters, discusses its significance and its limitations, and relates the scope for future studies in this sphere.

2. Background

2.1 Aims

This chapter provides relevant background information which is referred to in the rest of this thesis. Details of volumetric and surface absorption-based systems are compared, and existing literature related to direct absorption solar collectors which employ volumetrically heated systems is reviewed. Pertinent technical information is supplied, when necessary, in later chapters.

2.2 Need for volumetrically heated systems

As discussed already, there are a variety of solar thermal technologies which are operating all over the world (Figure 1.2). These technologies comprise of a receiver, a heat transfer fluid, and a power conversion cycle. The heat transfer fluid flows through the receiver which captures the incident solar radiation and transfers the energy to the fluid, thereby raising its temperature (Lenert, 2010). Other parts of these thermal systems are concentrating systems which focus the sunlight on to the receiver and enveloping surfaces which prevent heat loss from the receiver. The idea is to capture and transfer maximum amount of solar energy to the fluid and minimize thermal losses. These current systems utilize surface-based absorption mechanism, in which the receiver surface absorbs the radiation, and gets heated and its energy is transferred to the fluid flowing through it. However, as the surface heats up, the convection losses increase, and the surface also begins to radiate energy proportional to the fourth power of its absolute temperature according to the Stefan Boltzmann law:

$$E = \epsilon \sigma T^4 \tag{2.1}$$

This leads to massive losses particularly at high temperatures. Also, at high temperatures, a thermal barrier is formed between the surface and the fluid such that the fluid is unable to carry all the heat efficiently, leading to a further increase in surface temperature. Reported temperature differences (between the surface and fluid temperatures) have been as high as 500°C (Abdelrahman et al., 1979). As a result, the efficiency of the system suffers. The overall efficiency of these systems is around 15% while those of fossil fueled plants exceeds 50% (Pacheco, 2001). Low efficiencies of solar thermal systems combined with other factors such as the diurnal nature of solar radiation and

their cost makes them an inferior option compared to fossil fuel operated systems for power generation (Dutta, Pradeep, 2017; O Kazaz et al., 2023; Jain, Shubham et al., 2021).

It might seem that a simple way to improve the power output from these systems is by using higher solar concentration ratios (the ratio of collector aperture area to the absorber area), which apparently can be infinitely increased. However, upon applying the second law of thermodynamics to radiative exchange between the Sun and the receiver, the maximum concentration ratio for circular and linear concentrators is calculated as:

$$\left(\frac{A_{aperture}}{A_{receiver}}\right)_{circular,max} = \frac{1}{sin^2\delta} \tag{2.2}$$

$$\left(\frac{A_{aperture}}{A_{receiver}}\right)_{linear,max} = \frac{1}{sin\delta} \tag{2.3}$$

where, 'δ' is the half angle subtended by the Sun (Duffie et al., 2013). For $\delta = 0.27°$, the maximum theoretical possible concentration ratio for circular concentrators is 45,000 and for linear concentrators is 212.

Another way of improving the efficiency of surface-based absorption systems is by employing solar selective surfaces. Made of copper, with a layer of cupric oxide or silicon these surfaces are highly efficient at absorbing short wavelengths which form the bulk of solar radiation; however, they have low emissivity for long wavelengths emitted by the receiver surface. Figure 2.1 shows the spectral characteristics of incident solar radiation by approximating Sun as a black body at 5787K, and those of a blackbody at 1000K, 1250K and 1500K using Planck's law (equation 2.4) alongside emissive properties of an ideal solar selective surface which has an emissivity of 1 for all wavelengths below the cut-off wavelength but transitions to 0 above the cut-off wavelength. A selective surface with a cut-off wavelength at 2 μm would absorb the bulk of the solar radiation. However, at receiver temperatures of 1000K it has low emissivity (as well as absorptivity); as the temperature increases to 1500K, its emissivity (and absorptivity) increases.

$$e_{b\lambda} = \frac{c_1 \lambda^{-5}}{\exp(c_2/\lambda T) - 1} \tag{2.4}$$

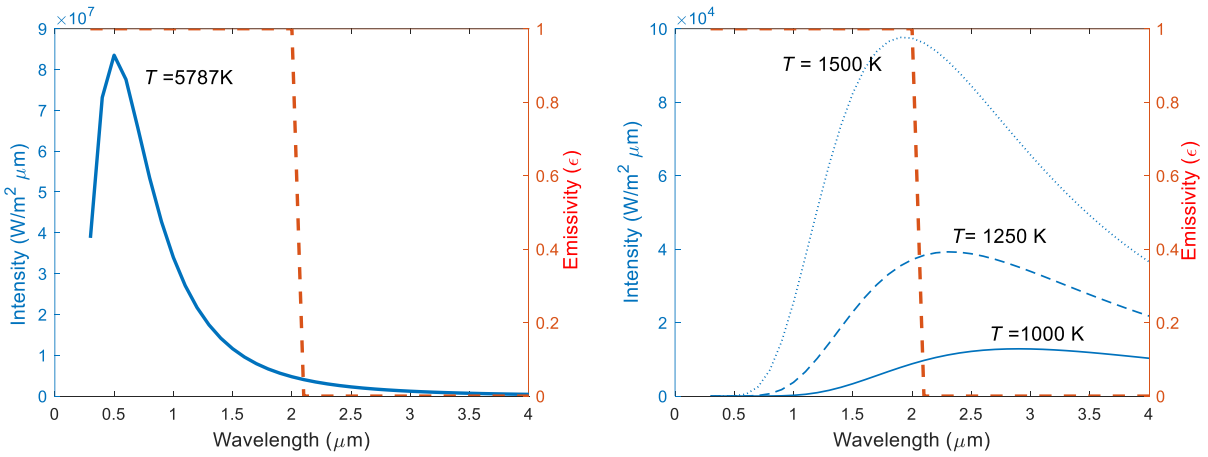

Fig. 2.1: (a). Spectral characteristics of incident solar radiation (blue) by approximating Sun as a black body at 5787K and emissive properties of solar selective surface (red) with a cut-off wavelength (2 µm). (b). Spectral characteristics of black body radiation (blue) at different temperatures (1000K, 1250K, 1500K) and emissive properties of solar selective surface (red) with a cut-off wavelength (2 µm).

Enveloping surfaces such as heat mirrors are also used in solar thermal systems, which allow shorter wavelengths to pass through but reflect long wavelengths such that any radiation emitted by receiver is reflected to receiver (Khullar et al., 2018b; Singh et al., 2023).

Despite all these measures, solar thermal systems with surface absorption-based receivers suffer low efficiencies. Volumetric systems also known as direct absorption solar collectors (DASC's) in theory can replace these systems and give a better performance. In these systems the opaque surface which captures solar radiation is replaced with transparent glass. The fluid flowing inside the receiver has nanoparticles added to it which alters their optical properties to absorb solar radiation. Such fluids are termed *'nanofluids'*, and they can be prepared using a wide variety of base-fluids such as water, paraffin oil, therminol etc. Nanoparticles added to it, as the name

suggests, are nano-sized and they can be carbon-based or metallic because otherwise the basefluid is transparent to a wide range of the solar spectrum (Otanicar et al., 2009; Rose et al., 2017). The particles being nano-sized do not settle down and remain suspended due to Brownian motion. However, their deployment in practical solar photothermal conversion technologies remains challenging due to the harsh operating conditions where the fluid is subject to intense solar radiation, high temperatures and thermal cycling of the fluid which impacts the colloidal stability of the nanofluids, and the nano-sized particles tend to agglomerate and settle down (Pordanjani et al., 2021; Sharaf et al., 2020). There are other practical difficulties such as clogging of pumps and valves, which limits their use (Otanicar et al., 2010). However, recent studies have reported low-cost methods of producing stable nanofluids (Singh et al., 2019). Since the radiation is captured directly by the fluid, the surface temperatures in such systems are not as high as in surface absorption-based systems thus reducing losses.

In the present work, the focus will be on studying the mechanism of heat transfer from incident solar energy directly to the working fluid as happens in volumetric systems. Particularly, the role of convection and interaction of the solar irradiance with the working fluid (nanoparticle dispersion) in dictating the flow field and temperature distribution shall be of interest in systems with forced and natural convection.

However, the applications of this work are not limited to solar thermal systems alone. The study of fluid filled enclosures leads us to a better understanding of the environment around us – the natural circulation of the atmosphere enveloping our planet, the circulation of ocean currents, and the movement of the molten core beneath the surface of Earth's crust, can all be studied by choosing an appropriate system (Kimura, 1983; Bejan, 1984).

In section 2.3, the literature pertaining to volumetrically heated systems with forced and natural convection induced by the penetration of radiation is reviewed.

2.3 Literature Review

As is evident from the above discussion, research pertaining to the phenomenon of volumetric absorption of radiation and its use in direct absorption solar collectors (DASCs) lies at the crossroads of several other research avenues such as radiative energy transfer, nanofluids, optical and thermo-physical properties of the components used in the design and construction of appropriate systems, fluid dynamics, heat transfer etc. The literature review covers research on

these systems by grouping it into different sections, each of which corresponds to one of the above-mentioned elements.

2.3.1 Review of literature on treatment of radiative energy transfer in the study of DASCs

Thermal energy radiated by an object is composed of electromagnetic waves (according to the wave theory) or packets of energy called 'photons' (according to the particle theory) and its speed is related to the speed of light in vacuum, *'c_o'*, by the formula:

$$c = \frac{c_o}{n} \tag{2.5}$$

where 'n' is the refractive index of the medium the wave is traveling in. As the electromagnetic wave travels through any medium (or vacuum) and strikes another medium, it may be either reflected (partially or completely) or the unreflected part travels into the medium where it gets attenuated as it travels through the medium; it may either be completely absorbed by the medium which means the medium is opaque or may pass through without any attenuation which means the medium is fully transparent or it may be attenuated partially which means the medium is semi-transparent. It depends on the material as well as its thickness whether a material is opaque, transparent, or semi-transparent. Thus, there are three fundamental radiative properties as defined below:

$$\textit{Reflectance, } \rho = \frac{reflected\ part\ of\ incoming\ radiation}{total\ incoming\ radiation} \tag{2.6}$$

$$\textit{Absorptance, } \alpha = \frac{absorbed\ part\ of\ incoming\ radiation}{total\ incoming\ radiation} \tag{2.7}$$

$$\textit{Transmittance, } \tau = \frac{transmitted\ part\ of\ incoming\ radiation}{total\ incoming\ radiation} \tag{2.8}$$

Also, since the incoming radiation is either reflected, absorbed, or transmitted, we get,

$$\rho + \alpha + \tau = 1 \tag{2.9}$$

Also, all surfaces emit radiation. At a given temperature, a black surface emits the maximum thermal radiation. A fourth property called *'emittance'* is used to quantify that which is defined as follows:

$$\textit{Emittance, } \epsilon = \frac{energy\ emitted\ from\ a\ surface}{energy\ emitted\ by\ a\ black\ surafce\ at\ the\ same\ temperature} \tag{2.10}$$

The radiative properties described above are dependent on the temperature and the wavelength of radiation. They may also vary in different directions. (Modest, 2021).

Just like solids, gaseous mediums can also absorb and emit radiation. As energy in the form of radiation passes through a gas, it gets attenuated. The decay in the intensity of incident radiation

has been observed to be varying exponentially according to the Beer-Lambert law. The transmissivity of a homogeneous gas layer is written as,

$$\tau = e^{-K_\alpha \cdot s}, \tag{2.11}$$

where *'s'* is the thickness of the layer of gas and *'K_α'* is the absorption coefficient. Also, gas layers either transmit radiation or absorb (reflectivity = 0), therefore, absorptivity of a gas layer can be defined as:

$$\alpha = 1 - e^{-K_\alpha \cdot s} \tag{2.12}$$

The interaction of radiation with particles also needs to be discussed as it is relevant to the study. It is different from the interaction of radiation with homogeneous gas or liquid or solid. As radiation travels through a medium with suspended particles, it may be either transmitted, reflected, or absorbed. Also, on interacting with particles, radiation may also change its path, known as 'scattering'. The equation for transmissivity in that case becomes,

$$\tau = e^{-(K_\alpha + K_s).s} = e^{-(K_e).s}, \tag{2.13}$$

where *'K_α', 'K_s'* and *'K_e'* are the absorption, scattering and extinction coefficients.

The nature of interaction between particles and electromagnetic radiation depends on the value of the size parameter given by,

$$\beta = \frac{\pi d}{\lambda} \tag{2.14}$$

where *'d'* is the effective diameter of the interacting particle. Depending on the value of *'β'*, we can classify the interaction to fall into one of the following regimes:

- B << 1, Rayleigh scattering, which holds true for interaction of radiation with very small particles in which scattering is proportional to ν^4 or $1/\lambda^4$.
- B ≈ 1, Mie scattering which is quantified using a complex and comprehensive theory.
- B >> 1, in which the particle surface can be treated as normal surface and properties can be found using geometric optics.

While working on any problem which involves heat transfer through conduction or convection as is required in the present study, it is important to know the thermophysical properties of the material used in the setup. Through the knowledge of material properties along with the application of law of conservation of energy, one can calculate the energy field in the system and determine the temperature field. Once the temperature field becomes known, one can apply the Fourier Law

to determine the heat flux vector. Similarly, in the case where heat transfer through radiation is involved, we need to know the radiative properties of the materials. The law of conservation of energy can then be applied to determine the energy field. However, the analysis of radiative energy transport is more complicated due to the following reasons: (a). Radiative properties, unlike thermophysical properties, are a function of direction as well as wavelength. (b). The basic variable in the equation of conservation of radiative transport is not temperature but intensity of radiation which is a function of location in space but also the direction.

The Radiative Transfer Equation (RTE) provides the value of radiation intensity along the line of sight by accounting for the three processes which influence it: *absorption*, *emission*, and *scattering*. Let us look at the simple form of Radiative Transfer Equation and how it can be used to find the temperature distribution across a slab.

As discussed above, the intensity of a plane wave propagating in a homogeneous absorbing medium is attenuated as $e^{[-K\lambda\, s]}$ where '$K_{e\lambda}$' is the spectral absorption coefficient and 's' is the path length.

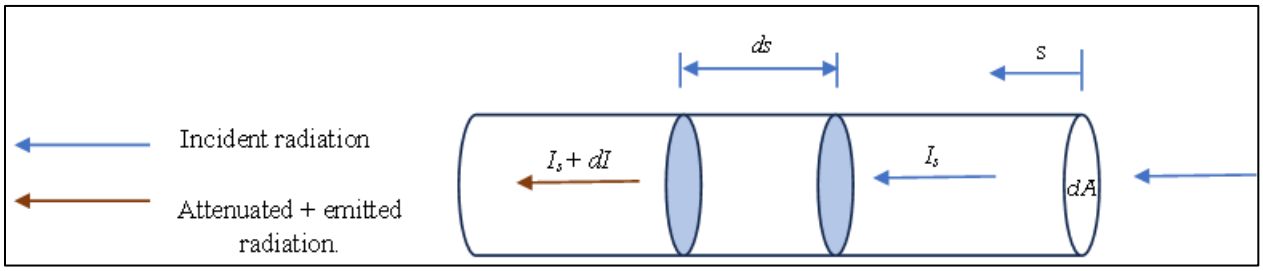

Fig. 2.2: Radiation energy balance along line of sight.

Applying energy balance on the differential volume element in Fig. 2.2.

Energy in - Energy out = Energy absorbed - Energy emitted (2.15)

$$\frac{dI_\lambda}{ds} = -K_{a\lambda}.I_{\lambda(s)} + K_{a\lambda}.I_{b\lambda(T)} \tag{2.16}$$

Integrating with respect to 's', we get the equation:

$$I_{\lambda(s+ds)} = I_{\lambda s}.e^{-K_{a\lambda}.s} + I_{b\lambda(T)}(1-e^{-K_{a\lambda}.s}) \tag{2.17}$$

where,

$$K_{a\lambda} = \lim_{ds\to 0} \frac{energy\ absorbed\ by\ volume\ dV}{energy\ incident\ on\ dV} \tag{2.18}$$

Figure 2.3 shows a slab discretized into volume elements each at different temperatures. The direction of propagation of radiation is given by the value of 'μ'. Positive value of μ implies radiation is travelling upwards (+ve direction) and negative value implies it is travelling downwards (-ve direction).

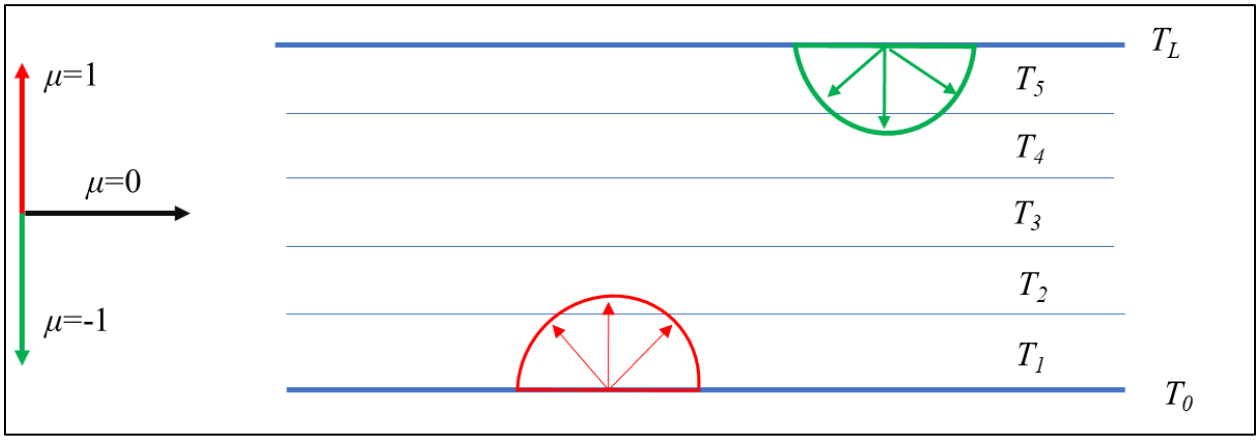

Fig. 2.3: Schematic showing a slab discretized into volume elements.

Since the change in intensity along an arbitrary slant path (s) is cosθ (μ) times the change along the normal path (x).

$$\frac{dI}{ds} = \mu \frac{dI}{dx} \tag{2.19}$$

The transfer equation along a slant path for this problem becomes,

$$\mu \frac{dI_\lambda}{dt} = -I_{\lambda 0} + I_{b\lambda(T)} \tag{2.20}$$

The solution to the equation is,

$$I_\lambda^+(t) = I_{1\lambda}^+ \exp\left(\frac{-t}{\mu}\right) + \int_0^t I_{b\lambda}(t').\exp\left(\frac{t'-t}{\mu}\right)\frac{dt'}{\mu} \tag{2.21}$$

The hemispherical flux at any location is obtained by integrating the intensity field (Fig. 2.4).

$$q_\lambda^+ = 2\pi \int_0^1 I_\lambda^+ \mu d\mu$$
$$q_\lambda^- = 2\pi \int_{-1}^0 I_\lambda^- \mu d\mu \tag{2.22}$$

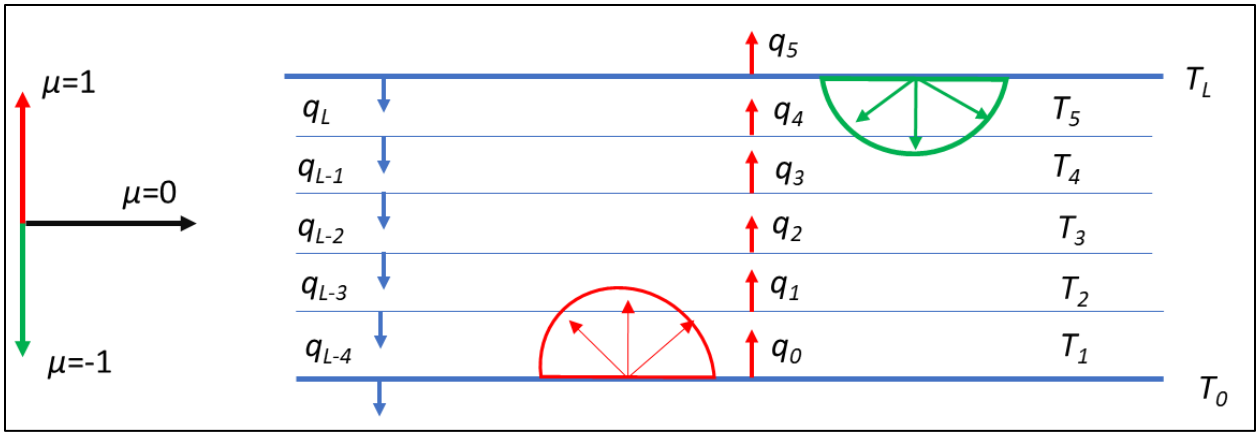

Fig. 2.4: Schematic showing flux at different points in the channel.

Divergence is the net heat flux leaving a control volume. In Fig. 2.4, for example, the divergence (*Div*) for the volume element at the bottom can be given as:

$$Div = q_1 - q_0 + q_{L-5} - q_{L-4} \tag{2.23}$$

The divergence thus calculated can be included in the energy equation to find the temperature distribution in a system.

$$\rho c_p \left[\frac{\partial T}{\partial t} + u\frac{\partial T}{\partial x} + v\frac{\partial T}{\partial y}\right] = k\left[\frac{\partial^2 T}{\partial x^2} + \frac{\partial^2 T}{\partial y^2}\right] - Div \tag{2.24}$$

Equation 2.17 is an over-simplified form of the radiative transfer equation which is an integro-differential equation for radiative intensity consisting of five independent variables (three space and two direction co-ordinates). For a non-gray medium, there is another variable to consider which is wavelength. Moreover, it becomes even harder to solve it when other modes of heat transfer are present. Therefore, the exact solutions to the equations of radiative transfer exist for very simple situations. For more complicated situations different methods are used. Given below is a brief review of the various methods used for solving the Radiative Transfer Equation (RTE) in different situations ranging from the simplest to complicated.

- *Exact Solutions of RTE for One-Dimensional Gray Medium*
  - *Radiative Equilibrium of a Non-Scattering Medium*
    - *Enclosure with black bounding surfaces:* For the case where the medium is placed between two black surfaces, the radiative transfer equation is transformed to the form of a Fredholm integral and can be easily solved. Its solution was first provided by Heaslet & Warming, 1965.

- *Gray, Diffuse Boundaries:* When in the previous case, instead of black boundaries, the problem involves gray, diffuse emitters and reflectors as bounding surfaces, the solution is similar except the flux except the flux entering and leaving the black walls previously is replaced by radiosities.

- *Radiative Equilibrium of a Scattering Medium*
  - *Isotropic Scattering:* For a medium with isotropic scattering, the relations used in the case for non-scattering medium are used as for a non-scattering medium there is no distinction between absorption and isotropic scattering.
  - *Anisotropic Scattering:* The methodology for solving the radiative transfer in a one-dimensional, plane parallel, anisotropically scattering medium has been solved by Modest and Azad, 1980, by considering full Mie-anisotropic scattering for particulate clouds.
- *Plane Medium with Specified Temperature Field:* When the medium is not in radiative equilibrium, which means that conduction and convection heat transfer in the system is not negligible and cannot be disregarded – an iterative procedure is followed to determine the temperature field because intensity of radiation is proportional to the fourth power of temperature, unlike the heat transfer by conduction and convection which is directly proportional to temperature.
- *Radiative Transfer in Spherical Media:* The problem of one-dimensional radiative transfer in a spherical medium was first studied by Sparrow et al., 1961, who investigated radiative equilibrium in a gray, non-scattering medium between two concentric black spheres. The sphere temperatures were constant and equal. A similar problem was solved by Rhyming (1966) without including the heat generation term and assuming the sphere surfaces at different temperatures. Viskanta and Crosbie (1967) solved a problem pertaining to radiative transfer in spherical medium by considering a non-scattering, grey medium with heat generation between two concentric spheres at different temperatures and emittances.
- *Radiative Transfer in Cylindrical Media:* The problem of radiative heat transfer in a cylindrical medium has been studied by Heaslet & Warming (1966) for isotropically scattering medium inside isothermal black cylinder. Azad & Modest (1981) also

worked on the problem for a one-dimensional, gray, anisotropically scattering cylinder with a specified temperature distribution.

- *Approximate Solutions of RTE for One-Dimensional Medium*

  Some of the techniques used for solving the Radiative Transfer Equation (RTE) resort to the use of approximate method as follows:

  - *Optically thick and thin approximation:* By assuming a slab consisting of a medium between two bounding surfaces as optically thick or thin, a simple expression for radiative flux can be obtained.
  - *Schuster Schwarzschild approximation:* The radiative intensity is assumed to be isotropic, but different over upper and lower hemispheres. The method can be generalized to higher order, and it is known as the Discrete Ordinates method.
  - *The Milne Eddington Approximation:* The method is also known as the Differential Approximation method and is used especially when dealing with complicated geometries.
  - *The Exponential Kernel Approximation:* In this method, the integrals in radiative transfer equation are approximated by functions of exponentials.

- *The Method of Spherical harmonics (P-N approximation):* Through this method, we can obtain an approximate solution to RTE by changing the equation into a set of partial differential equations (PDEs).
- *The Method of Discrete Ordinates (S-N approximation):* Like the method of Spherical Harmonics, the RTE is converted into a set of partial differential equations (PDEs).
- *The Zonal Method:* First developed by Hottel and Cohen for an absorbing, emitting, non-scattering gray gas with constant absorption co-efficient; later extended to deal with non-constant, non-gray absorption coefficients and isotropically scattering media. In this method, the enclosure volume is sub-divided into isothermal volumes and surface area zones. An energy balance is performed on radiation exchange between two zones leading to sets of simultaneous equations which can then be solved to find unknown temperature and heat fluxes.
- *Monte Carlo Method:* This method uses statistical sampling techniques to solve the problem of radiative transfer to any degree of accuracy.

Table 2.1 lists the important studies in the field of Direct Absorption Solar Collectors (DASCs chronologically, with a description of the treatment of radiative transfer equation in each study.

Table 2.1: Important studies in the field of (DASCs) with a description of the treatment of radiative transfer equation in each study.

S.No.	Reference	Treatment of Radiative Transfer Equation
1	Tyagi et al., 2009: Predicted efficiency of a low-temperature nanofluid-based DASC.	• The effect of emission by fluid layer is ignored. • To calculate the extinction co-efficient, the effect of in-scattering has not been considered.
2	Taylor et al., 2011: Applicability of Nanofluids in High Flux Solar Collectors.	• The absorption of radiation is modeled in the receiver with one-dimensional radiative transport equation. The optical properties are taken spectrally.
3	Khullar et al., 2012: Solar Energy Harvesting Using Nanofluids-Based Concentrating Solar Collector.	• Beer Lambert law has been applied to solve for radiative flux absorbed by the layers of the medium.
4	Lenert & Wang, 2012: Optimization of Nanofluid Volumetric Receivers for Solar Thermal Energy Conversion.	• The Differential Discrete Ordinate Method has been applied for the radiation transport. The optical properties have been considered in two bands.
5	Saidur et al., 2012: Evaluation of the Effect of Nanofluid-based Absorbers on Direct Solar Collector.	• Beer Lambert law has been applied to solve for radiative flux absorbed by the layers of the medium.
6	Veeraragavan, 2012: Analytical Model for the Design of Volumetric Solar Flow Receivers.	• Uses analytical model to find the effect of different parameters on the performance of volumetric receivers. The analytical model was formulated by modeling the absorption of solar radiation by the suspended nanoparticles as a volumetric heat release inside the flowing HTF.
7	Cregan and Myers, 2015: Modelling the efficiency of a Nanofluid Direct Absorption Solar Collector	• An approximate analytical solution is presented to study the steady state in a direct Absorption based Solar Collector. An approximate power-law function is used for radiative flux.
9	Hewakuruppu et al., 2016: Limits of Selectivity of Direct Volumetric Solar Absorption.	• One dimensional RTE is solved with the transport approximation which simplifies the RTE to a case of isotropic scattering from other directions. The modified two-flux approximation further simplifies the

		1D - RTE to determine the spectral reflectance, transmittance and emittance of a plain parallel layer of an absorbing and scattering medium.
10	Freedman et al., 2018: Analysis of Nanofluid Based Parabolic Trough Collectors for Solar Thermal Applications.	• Incorporation of thermal re-emission in the RTE.
11	Fan et al., 2018: Heat Transfer Analysis of a New Volumetric Based Receiver for Parabolic Trough Solar Collector.	• One dimensional RTE is solved and the elements of the receiver are treated as single entities with a uniform temperature in each.
12	O' Keeffe et al., 2018: Modelling the Efficiency of a Nanofluid based Direct Absorption Parabolic Trough Solar Collector.	• An approximate analytical solution is developed for the efficiency of a Direct Absorption Solar Collector. An approximate function for radiative flux is used to make analytical progress.
13,14	Sharaf et al., 2018a: Direct absorption solar collector (DASC) modeling and simulation using a novel Eulerian-Lagrangian hybrid approach: Optical, thermal, and hydrodynamic interactions. Sharaf et al., 2018b: Impact of nanofluids, radiation spectrum, and hydrodynamics on the performance of direct absorption solar collectors.	• Beer Lambert law has been applied to solve for radiative flux absorbed by the layers of the medium. The optical properties of the medium are considered spectrally.
15	Bonab & Javani, 2019: Investigation and Optimization of Solar Volumetric Absorption Systems Using Nanoparticles.	• Beer Lambert law has been applied to solve for radiative flux absorbed by the layers of the medium.

2.3.2 Review of literature on development of suitable nanofluids to be used as working fluids in DASCs

One of the important elements in the design and construction of volumetric systems is the working fluid. To effectively absorb solar radiation, it should have certain favorable characteristics. The distinguishing features of nanofluids employed in solar thermal systems are briefly discussed as follows (Sharaf et al., 2020):

1) *Low volume fraction of nanoparticles:* Optical properties required in photo-thermal conversion devices can be achieved by dispersing a very small amount of nanoparticles into the base fluid (<10 ppm or 0.1%). This contrasts with using nanoparticles to alter thermo-physical properties of base fluid that require relatively very high volume-fractions.
2) *Small nanoparticle size: Very* small size of nanoparticles (<40 nm) are preferred in volumetric absorption of incident sunlight to minimize the scattering of incident radiation. At such small sizes their scattering cross-section is negligible as compared to the absorption cross-section.
3) *Carbon based nanoparticles:* Carbon based nanoparticles have negligible scattering cross-sections and exhibit wide absorption ranges without peaks. Metal nanoparticles are not preferred because they can exhibit single or multiple sharp absorption peaks. Metal oxide nanoparticles are never used because of high scattering cross-sections.
4) *Water and oil base-fluids:* Water is used as a base-fluid in low-flux solar applications while oil is used for high-flux applications due to its high boiling point. Glycol based fluids (water-glycol mixture) are used in low-to-intermediate flux applications whereas molten salts are proposed for high flux, high-temperature applications.
5) *Composite nanofluids:* To achieve broadband absorption, hybrid nanofluids have been proposed using a blend of different nanoparticles in terms of size, geometry, or material (Hazra et al., 2021). However, they may pose additional complications in terms of colloidal stability as there is an additional component of interaction between different kinds of nanoparticles to consider.

One of the key challenges in building a working DASC with a nanofluid is related to the stability of nanofluids, physical as well as chemical, under the harsh operating conditions which these systems endure for long periods such as high temperatures, thermal and solar cycling, and exposure to intense solar radiation. Some important recent studies investigating the stability of nanofluids, and which yielded positive results are shown in Table 2.2.

Table 2.2: Important recent studies investigating the stability of nanofluids.

S.No.	Reference	Nanofluid Type and stabilizing agent	Stability Test	Results
1	Singh and Khullar, 2019	• Carbon soot nanoparticles in paraffin light oil • Stabilized by dispersion of Polyolefin	• Stored in ambient conditions for 6 months. • Tested at temperatures up to 300°C for 72 hours. • 100 cycles of thermal cycling between ambient temperature and 240°C. • Centrifugation for 90 minutes at 8000 rpm. • UV radiation cycling at 117 W/m^2 for 5 cycles at 8 h per cycle equivalent to 124 days of UV exposure	• Negligible changes in optical properties after ambient storage, centrifugation, and accelerated UV cycling. • Aggregation and sedimentation of particles at high temperatures of 300°C. • Under airtight conditions, particle aggregation does not occur after 12 hours at 300°C and after 100 thermal cycles.
2	Liu et al., 2018	• Reduced graphene oxide sheets (thickness of 1nm and few microns in length and width) mixed in water. • Graphene oxide reduced with L Ascorbic acid.	• Stored in ambient conditions for 10 days. • High particle volume fraction up to 10 ppm. • Radiated with Xenon lamp radiation (strength of 7 Suns) for 60 minutes. • Evaporation phase change by xenon lamp radiation	• Nanofluid stable without the need for a stabilizing agent. • Absorbance spectra before and after evaporation phase change remains same.
3	Sharaf et al., 2019	• Gold (Au) nanospheres in water. • Functionalized with PEG; coated with citrate	• Ambient storage for 16 months. • Increased particle concentration up to 0.358 mg/L. • Thermal cycling between ambient temperature and 75°C	• Nanofluids stable without the need for stabilizing agents. • PEG functionalized nanoparticles stable over time and with thermal cycling.

			for 2 cycles; 1 cycle consists of 12 hours of heating followed by 12 hours of cooling.	
4	Choi et al., 2018	• Multi-walled carbon nanotubes (diameter = 20 nm, length = 1-25 μm) in water.	• Storage at ambient temperatures for > 1 month. • Working temperature of 85°C for 5 hours and 10°C for greater than 2 days	• Nanofluids with SDBS and Triton most stable under ambient storage. • All nanofluids stable at 85°C except the one stabilized with Triton. • Nanofluids with SDBS and Triton stable at 10°C.

2.3.3 Review of literature on DASCs classified on the basis of geometry/orientation and type of flow.

The literature review has been broadly divided into two parts: a). Forced convection (Table 2.3) and, b). Natural convection (Table 2.4). Table 2.3 shows studies pertaining to flow in channels (forced convection) where the fluid is heated volumetrically. Most of these studies deal with the laminar regime of flow with Reynolds number up to 2000. The solar concentration ratio in these studies goes up to 100. Some of these studies consider radiative exchange between fluid layers which is important to consider at high temperatures. Studies are also classified based on the nature of nanoparticles (carbon-based or metallic).

Table 2.4 shows studies pertaining to natural convection in closed cavities. While there are numerous studies dealing with natural convection due to surface heating in enclosures (Ravi et al., 1994), literature pertaining to penetrative convection (convection caused by direct absorption of radiation by fluid) remains scant. The initial literature pertaining to the study of penetrative convection included cavities of different geometries (viz., rectangular, triangular, wedge-shaped etc.) being heated from the top mimicking lakes and reservoirs which receive solar radiation (Lenert et al., 2010; Kefayati et al., 2023; Krishnamurti et al., 1998; Moroni et al., 2006; Farrow et al., 1994; Mao et al., 2009; Hattori et al., 2014; Hattori et al., 2015a; Hattori et al., 2015b; Lei et al., 2003; Webb et al., 1987; Lenert et al., 2012). As research progressed, studies were conducted for other geometries such as tubes with circular/square cross-section with forced convective flow being heated volumetrically (Amber et al., 2018; Khullar et al., 2012; Khullar et al., 2014;

Freedman et al., 2018; Sharaf et al., 2018; Singh et al., 2020) simulating flow in a channel. More recent studies, however, are being conducted on cavities heated from the bottom and side thus causing a natural convective motion in the fluid filled cavity (Wang et al., 2021). There have been studies in the past catering to similar systems with internal natural convection, however most of them treated the effects of radiation on a fluid contained within differentially heated walls where buoyant enclosure flow will exist anyway (Kim et al., 1984; Larson et al., 1976) except for a handful of studies which took into consideration the attenuation of incident radiation as it falls on a cavity with a transmitting wall and gets deposited in consecutive layers (Webb et al., 1987a; Webb et al., 1987b). These few studies focused more on the phenomenon of natural convection taking place in volumetrically heated systems rather than concentrating on the performance of any application where this can be gainfully employed. Therefore, the present study tries to address this gap by focusing on the phenomenon of natural convection in volumetrically heated cavities and looks at where the study can be useful.

The literature pertaining to penetrative in general can be classified qualitatively according to the research methodology (viz. experimental, numerical, analytical), the shape of the cavity and the direction of incident radiation. Further classification can be carried out on a quantitative basis depending on the magnitude of incident radiation, fluid properties etc. From the table 2.4 it is evident that while there have been a lot of studies related to cavities being heated from top as happens in natural water bodies such as lakes and oceans and direct absorption solar collectors irradiated from the top, there are very few studies related to heating a cavity from the bottom and from side. While these studies deal with volumetrically heated cavities but only a few of them focus on their use in direct absorption solar collectors.

Table 2.3: Modeling of volumetric absorption receivers: (a) selected reported works for various flow conditions and SCRs, (b) modeling assumptions in relation to the optical properties and radiation exchange, and (c) selected reported works relevant to the nanoparticle materials and volume fractions.

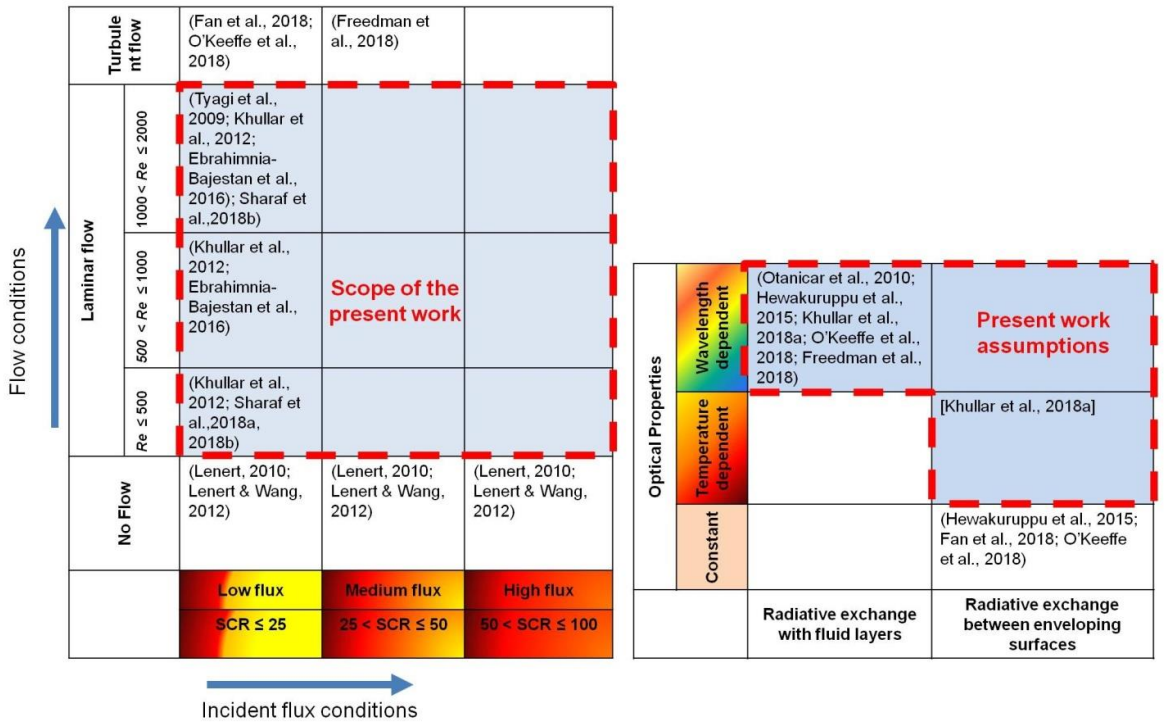

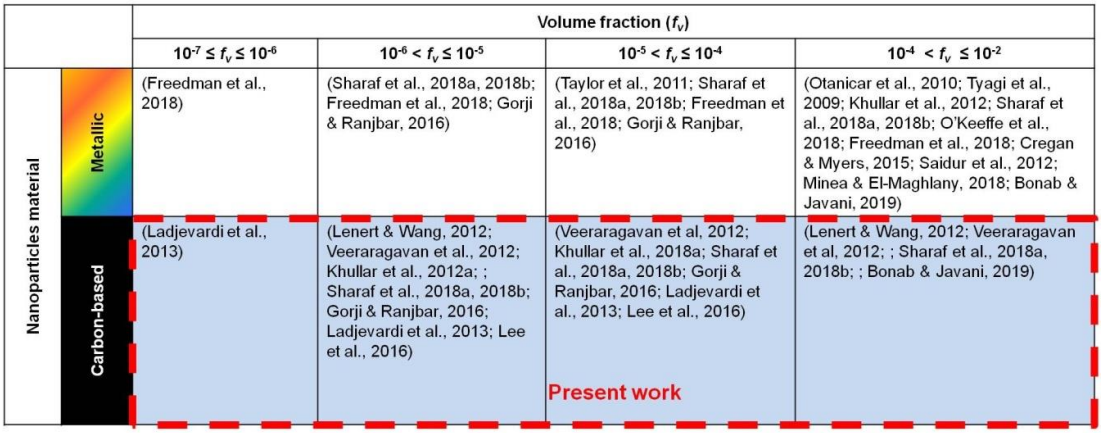

Table 2.4: Table detailing selected studies relevant to volumetrically heated cavities irradiated from bottom, top and side. These have further been categorized depending on the methodology employed (viz numerical, experimental, or analytical), visualization techniques used, direction of incident radiation, cavity shape and the scope of the present study.

	THEORETICAL			EXPERIMENTAL
	ISOTHERMS	STREAMLINES	HEATLINES	
HEATING FROM BOTTOM 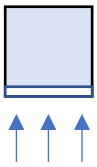	**Singh et al., 2023**	**Singh et al., 2023**		Lepot et al., 2018, Wang et al., 2019, Wang et al., 2020a, Wang et al., 2020b, Wang et al., 2021
HEATING FROM TOP 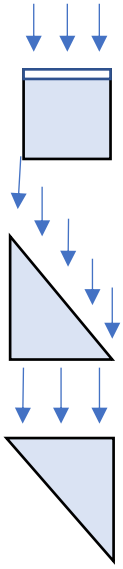	Coates & Patterson, 1993[rec], Krishnamurti, 1993[rec], Farrow & Peterson, 1994[wedge], Farrow & Peterson, 1993[wedge], Mao et al., 2009[tri] , Hattori et al., 2015[rec], Lei & Patterson, 2003[wedge], Lei & Patterson, 2002[wedge] , Onyegegbu 1990[rec], Vervochkin & Startsev 2000[rec], Hattori et al. 2014[par], Bednarz et al., 2009[wedge], Amber & O'Donavan 2017[rec], Wu et al., 2009[rec], **Singh et al., 2022**, **Lenert & Wang, 2012[rec]**	Coates & Patterson, 1993[rec], Onyegegbu 1990[rec], Vervochkin & Startsev 2000[rec], Hattori et al. 2014[par], Bednarz et al., 2009[wedge], Amber & O'Donavan, 2017[rec], Wu et al., 2009[rec], **Singh et al., 2022**		Coates & Patterson 1993[rec], Moroni & Cenedese, 2006[rec], Lei & Patterson, 2002[wedge], Wang et al., 2021[cyl], Wu et al., 2009[rec], **Lenert & Wang, 2012[rec]**
HEATING FROM SIDE 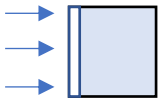	Webb & Viskanta, 1987a[rec], Webb & Viskanta, 1987b[rec]	Webb & Viskanta, 1987a[rec], Webb & Viskanta, 1987b[rec]		Webb & Viskanta, 1987a[rec], Wang et al., 2021[cyl]
NON-UNIFORM HEAT FLUX 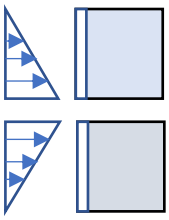				

SCOPE OF THE PRESENT STUDY

SCOPE OF THE PRESENT STUDY

cyl: cylindrical cavity; rec: rectangular cavity; tri: triangular cavity; wedge: wedge shaped cavity; par: parallelopiped cavity; Bold font: studies which relate to direct absorption solar collectors

Throughout the literature studies have shown the superiority of direct absorption-based collectors over surface absorption-based solar collectors. However, the number of studies is few, and they do not cover all aspects of operation. In studies where forced convection in channels is considered (Table 2.3), very few studies have investigated the role of other optical elements used in the construction of direct absorption systems; studies have also been limited in their scope by considering limited values of operational parameters such as flow conditions, incident heat flux etc.; also mathematical models used in many numerical studies have been over simplified and do not consider emission by fluid layers etc. Studies pertaining to natural convection in cavities (Table 2.4) due to direct absorption of incident radiation catering to solar thermal systems are even fewer. Only a handful of such studies exist. This thesis tries to fill this gap in literature and studies both kinds of systems (forced convection in channels and natural convection in cavities). The present work studies forced convection in channels and natural convection in cavities heated volumetrically. We have only pursued the avenue of laminar flows in the present work and that limits its applications to special circumstances. The study of transition and turbulent regimes is important as the heat transfer characteristics in case of turbulent flow differs greatly from that of laminar flow. However, the mathematical formulation to study turbulence is markedly different from that used to study laminar flow and to include them both in a single study would be a mammoth undertaking. Therefore, in present work only laminar flow situation is investigated.

The next chapters deal with the mathematical framework used to study these systems, the results and their analysis obtained from the study and finally the conclusion and the future scope for the work.

3. Methodology

3.1 Aims

This chapter provides the primary data used in the study and the details of the modeling framework. The chapter is divided into two parts: (1). details pertaining to the study of forced convection in channels and (2). details pertaining to the study of natural convection in cavities.

3.2 Forced convection in channels

3.2.1 Constructional details

In the present study, different designs of volumetric and surface absorption-based systems with different configurations of optical elements are studied which can be employed as solar collectors. The designs consist of fluid flowing in a channel through forced convection, enveloped by an outer casing. Figures 3.1(a) and (b) show volumetric absorption-based receiver (VAR) design configurations and 3.1 (c) and (d) show surface absorption-based receiver (SAR) designs.

In the volumetric systems, nanofluid flows through a rectangular conduit with transparent top (glass) surfaces so that solar radiation passes through and interacts directly with the working. In surface absorption-based systems, the working fluid (base fluid) flows through a rectangular conduit with an opaque top surface (black or solar selective) which absorbs the incident energy and heats up. Subsequently, the fluid in the channel absorbs energy from the top surface. The casing of the channel is made up of either glass or heat mirror. Although, all the receiver configurations are distinct; they ensure absorbing maximum incident solar energy and reducing losses.

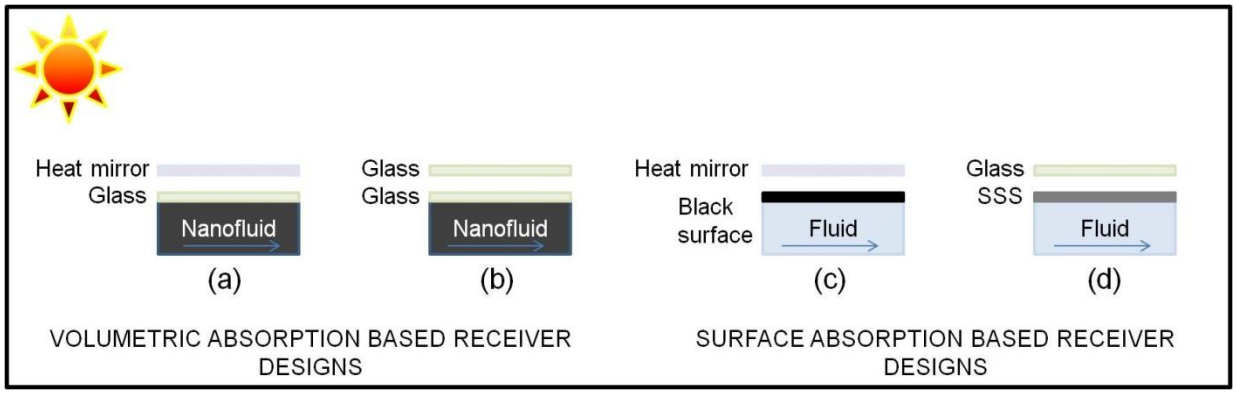

Fig. 3.1: Schematic showing the different designs: (a) glass - heat mirror (G-HM), and (b) glass - glass (G-G); (c) black surface - heat mirror (BS-HM), and (d) solar selective surface - glass (SSS-G).

3.2.2 Theoretical modeling framework

(a). Spectral optical properties of constituent elements

Venn diagram detailing broad optical characteristics of the constituent optical elements' viz., nanofluid, solar selective surface, black surface, basefluid, heat mirror, and glass is shown in Fig. 3.2(a). Optical elements could be broadly categorized into 'enveloping surfaces' and 'solar energy absorbing elements'.

(b). Enveloping surfaces (glass and heat mirror)

Enveloping surfaces, whether for volumetric or surface absorption-based systems should be highly transparent to the incident sunlight (short wavelength radiations) so that maximum amount of sunlight is able to reach the absorbing medium/surface [see Fig. 3.2(d) and high absorptivity (glass) or reflectivity (heat mirror) values in the long wavelength infrared region [see Fig. 3.2(c)] such that they do not allow radiation emitted by the receiver to escape. The spectral transmissivity values for glass have been calculated (detailed in appendix A) utilizing data from Rubin, 1985. The transmissivity values for heat mirrors have been taken from Khullar et al., 2018a.

Both glass and heat mirror have high transmissivity values at short wavelengths (Khullar et al., 2018a.; Rubin, 1985). However, at wavelength beyond 1μm (cut-off wavelength), the transmissivity of heat mirror falls rapidly. This leads to a considerably lesser solar weighted transmissivity [defined by Eq. (3.1)] for heat mirrors (τ_{sw} = 0.872) than for glass (τ_{sw} = 0.978) and thus allows more solar radiation to pass through in the systems with a glass cover. Moreover, transmissivity and reflectivity of heat mirror are not independent from each other. This becomes

clear if we carefully look at the constructional details of the heat mirror. Heat mirror is made of a thin layer of IR reflecting material (such as indium tin oxide) coated on glass. For a given coating material, more the coating thickness, lesser is the transmissivity and vice-versa. Therefore, trade-offs need to be made at different receiver operating temperatures (by tuning the value of cut-off wavelength, which depends on the coating material, and the coating thickness) to ensure optimum performance.

$$\tau_{sw} = \frac{\int_{\lambda=0.3\mu m}^{\lambda=30\mu m} \tau_\lambda S_\lambda d\lambda}{\int_{\lambda=0.3\mu m}^{\lambda=30\mu m} S_\lambda d\lambda} \approx \frac{\sum_{\lambda=0.3\mu m}^{\lambda=30\mu m} \tau_\lambda S_\lambda d\lambda}{\sum_{\lambda=0.3\mu m}^{\lambda=30\mu m} S_\lambda d\lambda} \tag{3.1}$$

where S_λ is the spectral solar irradiance (AM 1.5) and τ_λ is the corresponding spectral transmissivity value of the enveloping surface (glass/heat mirror)

(c). Solar energy absorbing elements (nanofluid, solar selective surface, black surface)

These are characterized by high values of extinction coefficients in the short wavelength solar irradiance region to ensure efficient photo-thermal energy conversion (detailed calculation is presented in appendix A). In the present work, due to broad absorption characteristics and high temperature requirements, amorphous carbon nanoparticles (d = 30nm) dispersed in Therminol 66 (a high temperature heat transfer fluid) are selected to form the nanofluid. Figure 3.2(b) shows the spectral extinction coefficient of the nanofluid as a function of nanoparticles volume fraction. Additionally, solar selective surfaces are engineered to have low emissivity in the long wavelength infrared wavelength band to ensure low radiative losses. Since both nanofluids and black surfaces have high emissivity in the infrared region, the enveloping surfaces [particularly heat mirrors, as shown in Figs. 3.2(a) and 3.2(c)] are required to mitigate radiative losses. The emission spectra of black surface at temperatures 1000K and 1500K are also laid out in the graph showing the wavelengths at which peak emission occurs in each instance. The peak shifts towards the left as the temperature rises [Fig. 3.2(c)].

In essence, any combination of optical elements which ensures high photo-thermal energy conversion in conjunction with low thermal losses is suitable for solar thermal applications.

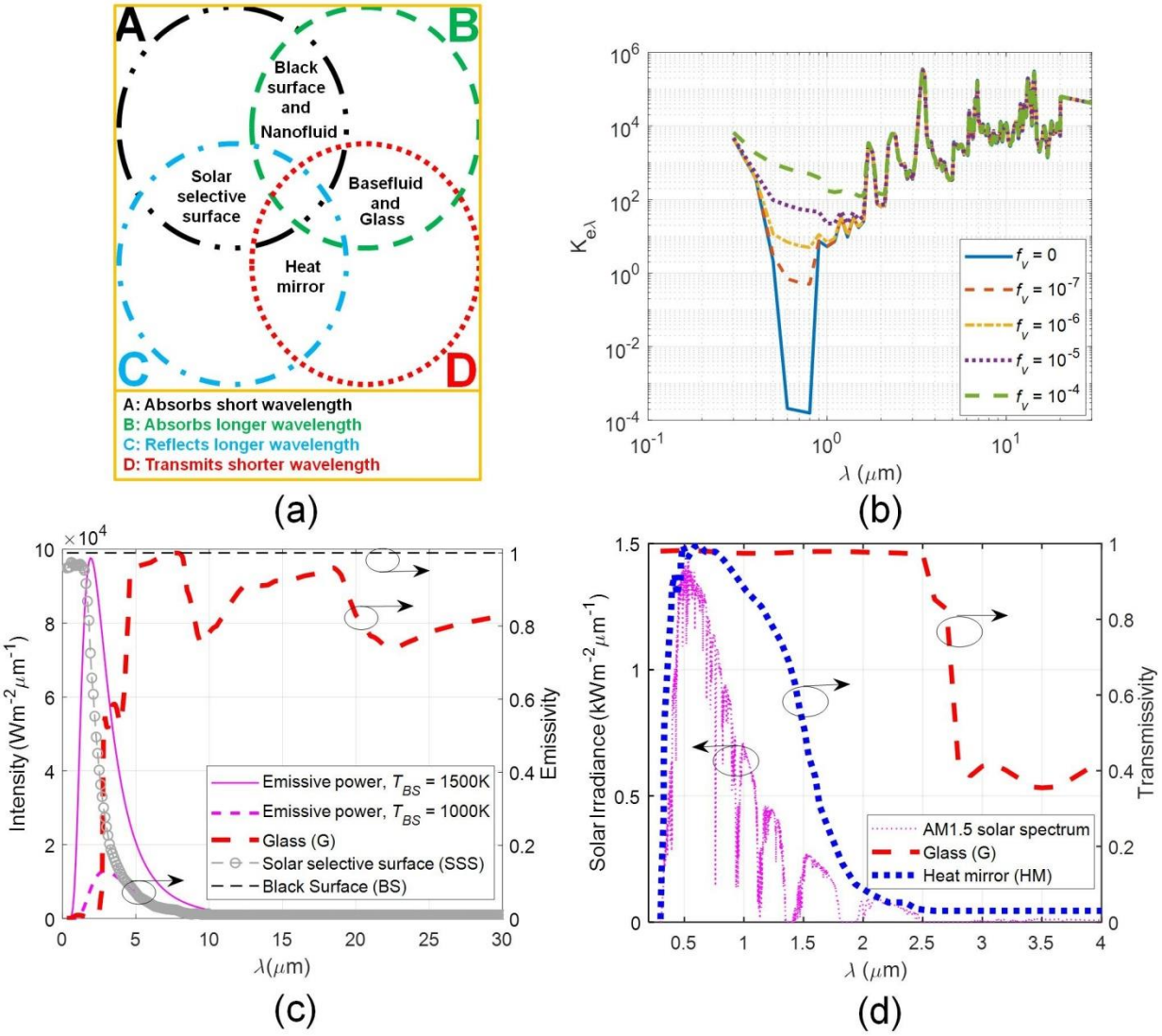

Fig. 3.2: (a) Venn diagram showing typical optical property characteristics of receiver constituent materials, (b) spectral extinction coefficients as a function of nanoparticles volume fraction, (c) spectral emissive power at various black body temperatures and spectral emissivity of various optical surfaces, and (d) AM 1.5 solar spectrum and spectral transmissivity of glass and heat mirror.

(d). Modeling heat transfer mechanisms

Once the spectral optical properties of various constituent elements are ascertained, the next step is to model heat transfer mechanisms involved in these systems.

Figure 3.3 shows the schematic detailing the heat transfer mechanisms involved in volumetric and surface absorption-based receivers.

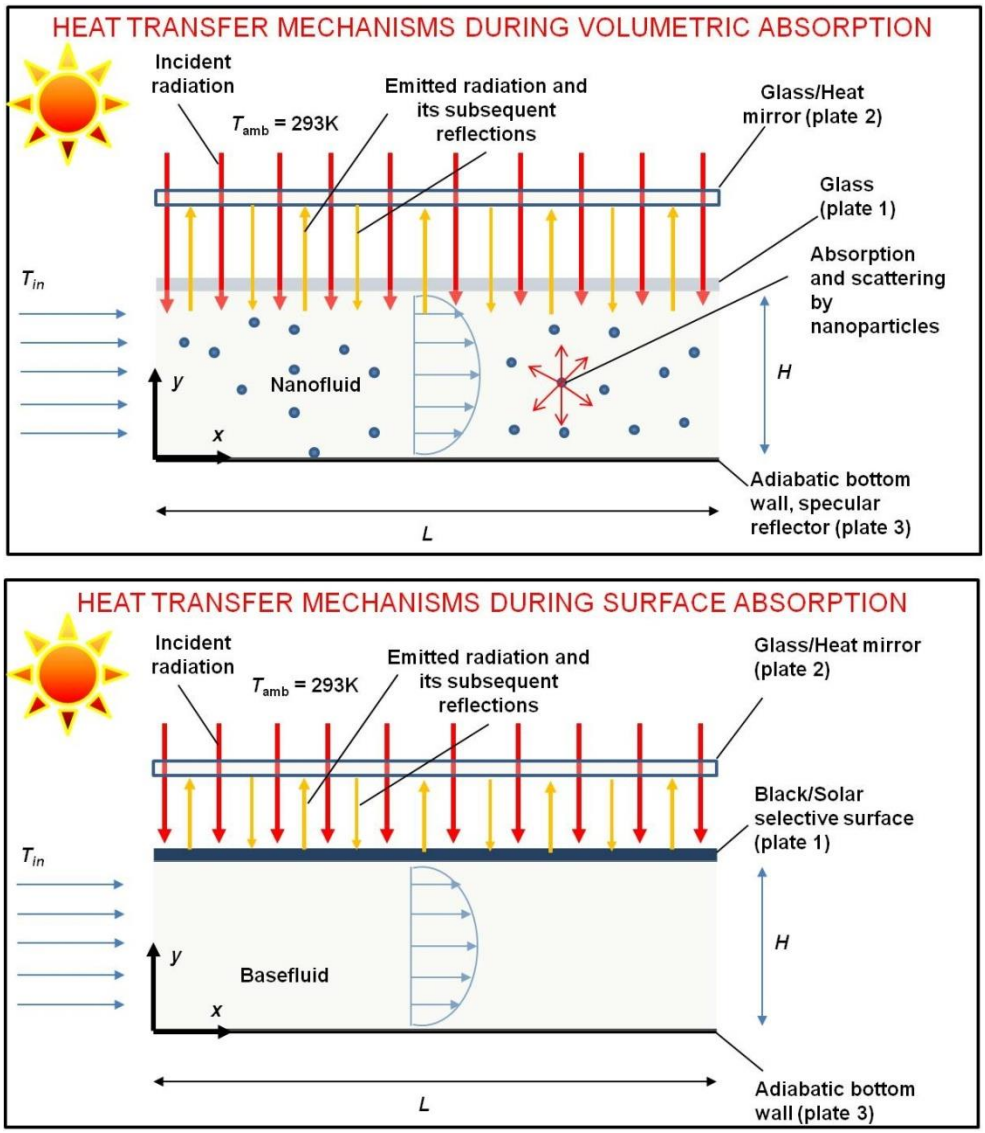

Fig. 3.3: Schematic showing the heat transfer mechanisms involved in (a) volumetric absorption-based receivers (VARs), and (b) Surface absorption-based receivers (SARs).

The developed models are based on certain simplifying assumptions which apply to both volumetric and surface absorption-based systems. Certain aspects such as radiation exchange

between the covers are common to both VARs and SARs; and have been described in detail in 3.2.2(e). However, there are some aspects which are specific to the nature of absorption mechanisms and subsequent heat transfer routes involved (i.e., characteristics of volumetric and surface absorption-based systems); therefore, these have been treated separately in detail (subsections 3.2.2(f) and 3.2.2(g)).

(e) Underlying assumptions

Following are the modeling assumptions which are common to both VARs and SARs:

- The flow inside the channel is assumed to be laminar (Re < 1600), steady and fully developed with a parabolic velocity profile given by Eq. (3.2). The y-component of velocity is assumed to be zero (Sharaf et al., 2018c).

$$u_y = 6u_{av}\left[\frac{y}{H} - \left(\frac{y}{H}\right)^2\right] \tag{3.2}$$

where,

$$u_{av} = \frac{\mathrm{Re}.\mu_f}{D_f.(H)} \tag{3.3}$$

- Heat transfer by conduction in the x-direction has been ignored as convection from the moving fluid is the predominant mode of heat transfer.
- The bottom plate of the channel is assumed to be completely reflective to maximize absorption of radiation by the working fluid.
- The heating of the channel from the top will not induce natural convection in the channel which has been thereby ignored in the formulated model.
- There is nearly a vacuum between the two cover plates, i.e., no convective heat transfer between plate 1 and plate 2.
- Heat transfer coefficient between the casing and the atmosphere is assumed to be $10 Wm^{-2}K^{-1}$ (Duffie & Beckman, 2013).
- Thermophysical properties of the nanofluid are assumed to be same as that of the base fluid and also constant with respect to temperature.

(f). Radiation exchange between two parallel cover plates (plate 1 and plate 2)

The objective of this section is to outline the procedure involved in calculating radiation exchange between the cover plates. A system of two plates with known spectral optical properties is considered. The net heat lost by the top plate of the conduit (referred to as plate 1) and the heat gained by the cover plate (referred to as plate 2) where one or both are semi-transparent is explained in this section. As a result of multiple reflections taking place between the two plates, and the fact that the radiation is spectral in nature and two-way coupling exists between the optical behavior and plate temperatures; parameters such as effective emissivity, absorptivity, reflectivity, and transmissivity are required to be defined to quantitatively determine the overall optical characteristics of the interacting plates (detailed procedure for calculating these optical parameters is provided in appendix B).

It is important to note that in case of radiation exchange between semi-transparent plates (unlike opaque surfaces), the net heat lost by one plate does not equal the net heat gained by the second plate. Figure 3.4 shows radiation exchange process taking place between two semitransparent or one semitransparent and one opaque plates. Figure 3.4(a) shows the passage of the radiation emitted by plate 1 – some of it is absorbed by plate 1 ($i_1, j_1, k_1 \ldots\ldots \infty$) and 2 ($o_1, p_1, q_1, r_1 \ldots\ldots \infty$), some is transmitted through plate 1 ($l_1, m_1, n_1 \ldots\ldots \infty$), and 2 ($s_1, t_1, u_1, v_1 \ldots\ldots \infty$). Similarly, figure 3.4(b) details the passage of the radiation emitted by plate 2. To summarize the 'red lines' show the radiation emitted by plates 1 and 2 which keep getting reflected between the two plates (until it is either absorbed by or transmitted through the plates); green and blue lines show the fraction of radiation absorbed and transmitted through plate 1 and plate 2, respectively.

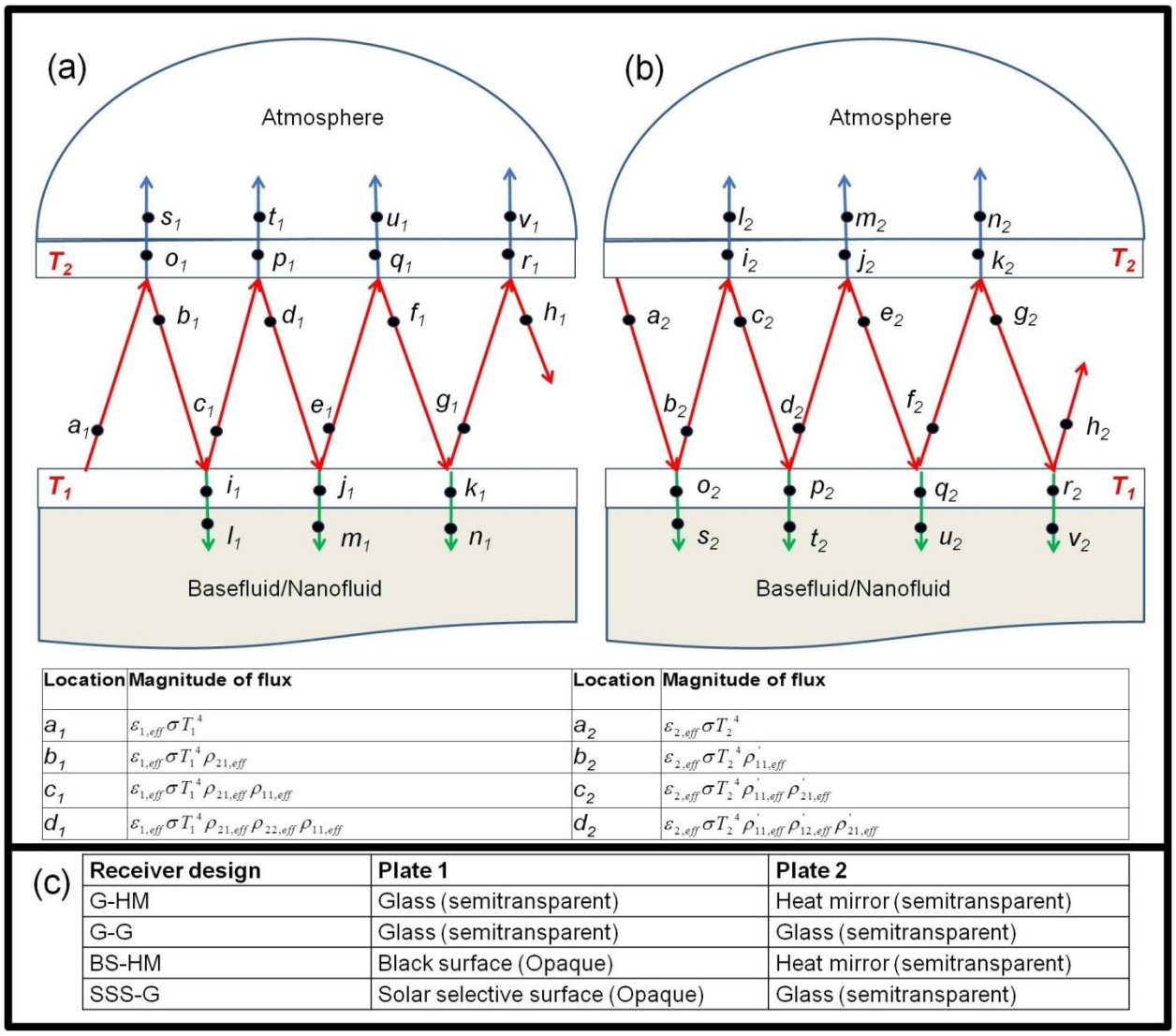

Location	Magnitude of flux	Location	Magnitude of flux
a_1	$\varepsilon_{1,eff}\sigma T_1^4$	a_2	$\varepsilon_{2,eff}\sigma T_2^4$
b_1	$\varepsilon_{1,eff}\sigma T_1^4 \rho_{21,eff}$	b_2	$\varepsilon_{2,eff}\sigma T_2^4 \rho'_{11,eff}$
c_1	$\varepsilon_{1,eff}\sigma T_1^4 \rho_{21,eff} \rho_{11,eff}$	c_2	$\varepsilon_{2,eff}\sigma T_2^4 \rho'_{11,eff} \rho'_{21,eff}$
d_1	$\varepsilon_{1,eff}\sigma T_1^4 \rho_{21,eff} \rho_{22,eff} \rho_{11,eff}$	d_2	$\varepsilon_{2,eff}\sigma T_2^4 \rho'_{11,eff} \rho'_{12,eff} \rho'_{21,eff}$

(c)

Receiver design	Plate 1	Plate 2
G-HM	Glass (semitransparent)	Heat mirror (semitransparent)
G-G	Glass (semitransparent)	Glass (semitransparent)
BS-HM	Black surface (Opaque)	Heat mirror (semitransparent)
SSS-G	Solar selective surface (Opaque)	Glass (semitransparent)

Fig. 3.4: Schematic showing radiation exchange between two parallel plates: ray tracing (and corresponding equations) of the energy emanating from the (a) plate 1, and (b) plate 2.

Calculation of radiation exchange inherently requires the temperatures of the two plates to be known and to know the plate temperatures radiation exchange values should be known 'a priori'. Also, the plate 1 is in thermal contact with the nanofluid (whose temperature is unknown) - thus there is a complex coupled interaction.

This was circumvented by first computing the temperature of plate 2 (T_2) as a function of plate 1 temperature (T_1); then it is used to calculate the energy absorbed by plate 1 through radiation exchange (Fig. 3.4) and employed it in the energy equation for the nanofluid flow in the conduit.

Now, in order to find a functional relationship between the temperature of top cover (plate 2) and the temperature of the top plate of conduit (plate 1); a relationship for energy balance (assuming each instant in time to represent a quasi-steady-state condition) is invoked by equating the energy gained by the plate 2 from the plate 1 with the energy lost by the plate 2 due to radiation and convection [given by Eq. (3.4)]. In other words, plate 1 temperature is treated as an independent input variable to the function defined by Eq. (3.4).

$$2\varepsilon_{2,eff}\sigma {T_{2,avg}}^4 - \alpha_{atm,eff}\sigma T_{amb}^4 + h_{wind}(T_{2,avg} - T_{amb}) = \varepsilon_{2,eff}\sigma {T_{2,avg}}^4[\rho'_{11,eff}\alpha'_{21,eff} + \rho'_{11,eff}\rho'_{12,eff}\rho'_{21,eff}\alpha'_{22,eff} + ...\infty] + \varepsilon_{1,eff}\sigma T_{1,avg}^4[\alpha_{21,eff} + \rho_{11,eff}\rho_{21,eff}\alpha_{22,eff} + \rho_{11,eff}\rho_{12,eff}\rho_{21,eff}\rho_{22,eff}\alpha_{23,eff} + ...\infty] \quad (3.4)$$

Here, the energy gained by plate 2 from radiation exchange with plate 1 is given by adding flux at locations o_1, p_1, q_1, $r_1...\infty$ and i_2, j_2, $k_2...\infty$ (the RHS of Eq. (3.4)). Energy lost by plate 2 due to radiation and convection is given by the LHS of Eq. (3.4). From equating the two, temperature T_2 of plate 2 as a function of plate 1 temperature T_1 is obtained.

Figure 3.5 shows the relationship between the top and bottom plate temperatures for various combinations of plate materials. By treating T_1 as an independent input variable in Eq. (3.4), the relationship between plate 1 and plate 2 temperatures is quantified without having the need to solve the coupled overall energy balance equations for the cover plates and the nanofluid.

Once the relationship between the two plate temperatures is known, Eqs. (3.5) and (3.6) are used to calculate $q_{loss,1}$ and $q_{\text{trans}\rightarrow\text{nf}}$ and subsequently use them to solve overall energy equations for plates and the nanofluid.

$$q_{loss,1} = \varepsilon_{1,eff}\sigma {T_{1,avg}}^4[1 - \rho_{21,eff}\alpha_{11,eff} - \rho_{21,eff}\rho_{22,eff}\rho_{11,eff}\alpha_{12,eff} - \rho_{21,eff}\rho_{22,eff}\rho_{23,eff}\rho_{11,eff}\rho_{12,eff}\alpha_{13,eff} - .....\infty] - \varepsilon_{2,eff}\sigma T_{2,avg}^4[\alpha'_{11,eff} + \rho'_{11,eff}\rho'_{21,eff}\alpha'_{12,eff} + \rho'_{11,eff}\rho'_{12,eff}\rho'_{21,eff}\rho'_{22,eff}\alpha'_{13,eff} + ...\infty] \quad (3.5)$$

where, the term '$q_{loss,1}$' represents the net loss from plate 1 and is calculated by computing the net flux leaving the plate 1. In other words, subtracting the fluxes absorbed by plate 1 (i_1, j_1, k_1...∞ and o_2, p_2, q_2 ...∞) from the initial flux radiated by plate 1 (flux value at a_1).

Similarly, the value of energy transmitted through to the nanofluid ($q_{\text{trans}\rightarrow\text{nf}}$) flowing underneath the plate 1 can be computed by summing fluxes at points l_1, m_1, n_1….∞ and s_2, t_2, u_2, v_2 ….∞ and it value is as given in Eq. (3.6).

$$q_{trans\rightarrow nf} = \varepsilon_{1,eff}\sigma T_1^4\left[\rho_{21,eff}\tau_{11,eff} + \rho_{21,eff}\rho_{22,eff}\rho_{11,eff}\tau_{12,eff} + \rho_{21,eff}\rho_{22,eff}\rho_{23,eff}\rho_{11,eff}\rho_{12,eff}\tau_{13,eff} + ...\infty\right] + \varepsilon_{2,eff}\sigma T_2^4\left[\tau'_{11,eff} + \rho'_{11,eff}\rho'_{21,eff}\tau'_{12,eff} + \rho'_{11,eff}\rho'_{12,eff}\rho'_{21,eff}\rho'_{22,eff}\tau'_{13,eff} + ...\infty\right] \quad (3.6)$$

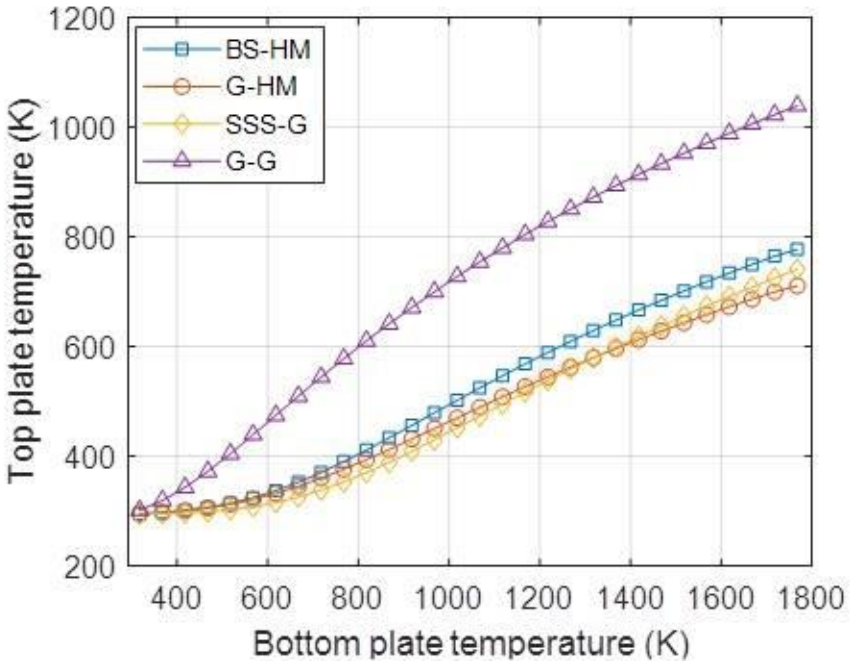

Fig. 3.5: Top plate (plate 2) temperature as a function of bottom plate (plate 1) temperature for various combinations of plate materials.

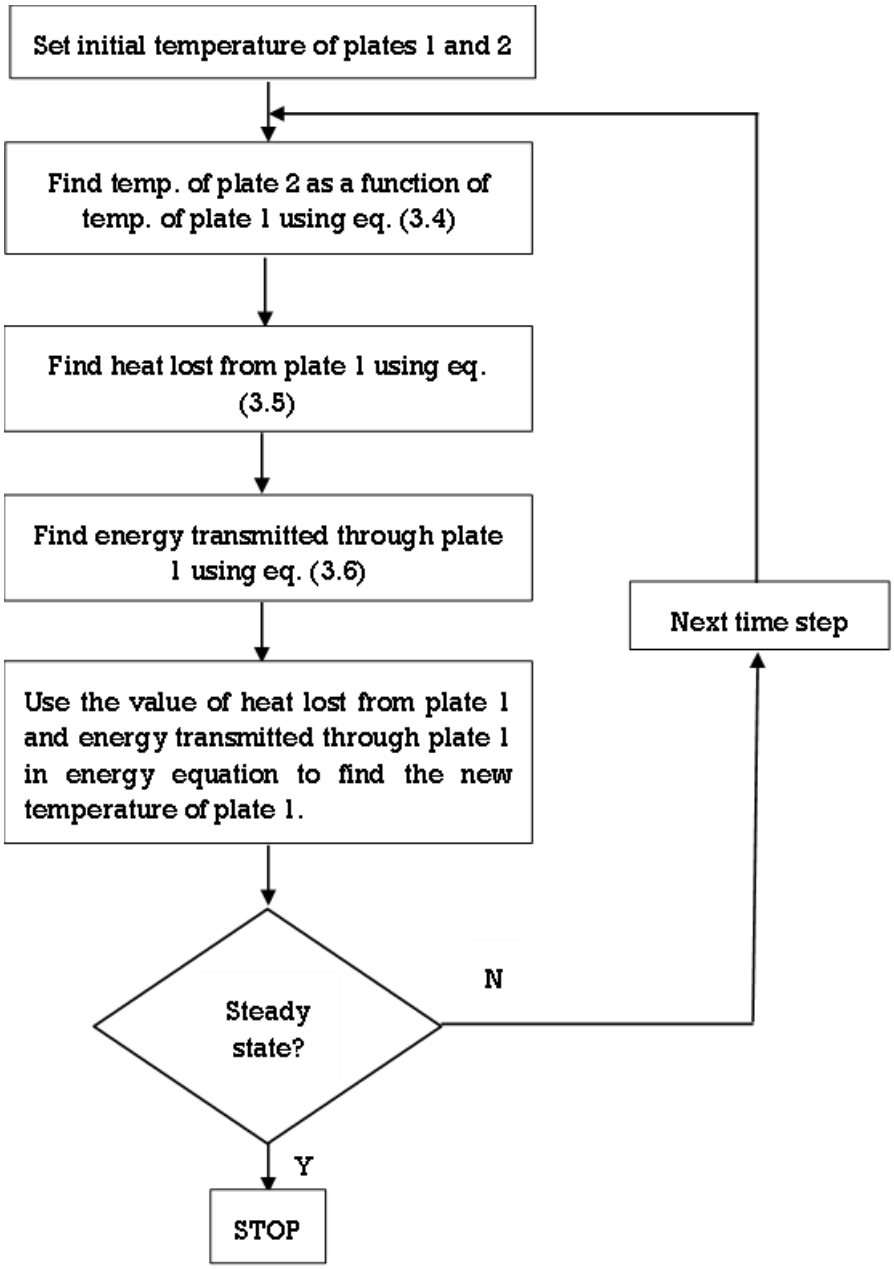

Fig. 3.6: Flowchart outlining the methodology for calculation of flux from radiation exchange between the two plates to be used in energy equation for calculation of temperature.

(g). Volumetric absorption based solar thermal systems: The flowchart in Fig. 3.7 gives a brief overview of the process of theoretical modeling pertinent to volumetric systems.

On its way to the nanofluid, sunlight interacts with the two cover plates. The outer cover (plate 2) could be made of glass or heat mirror, whereas the plate in contact with the nanofluid is essentially

made of glass (plate 1). The heat gain by plate 2 due to radiation exchange with plate 1 and the heat loss to the atmosphere (via convection and radiation) represents the overall energy balance for plate 2 and is given by Eq. (3.4). However, plate 1, in addition to experiencing heat loss due to radiation exchange with plate 2, is also in thermal contact with the nanofluid (i.e., conjugate heat transfer exists between plate 1 and nanofluid). Equations (3.7)–(3.10) describe the governing, initial and boundary conditions for the plate 1. It may be noted that the term $q_{\text{loss},1}$ is based on the temperatures of the two cover plates, which in turn requires solving Eq. (3.7) subjected to initial and boundary conditions [Eqs. (3.8)–(3.10)]. Further, to solve Eq. (3.10), RTE and the overall energy equations for the nanofluid have been solved.

$$\frac{\partial T}{\partial t} = \frac{k_1}{D_1 c_{p1}}\left[\frac{\partial^2 T}{\partial y^2}\right] - \frac{1}{D_1 c_{p1}}\frac{\partial q_{loss,1}}{\partial y} + \frac{1}{D_1 c_{p1}}\frac{\partial}{\partial y}\int \tau_{2\lambda} S_\lambda \left(1 - e^{-K_{a\lambda,1}(H+t_1-y)}\right) d\lambda \tag{3.7}$$

Here, the first term (on the right-hand side) is the diffusion term and the second and third terms combined represent the source term.

$$T(y)\big|_{t=0} = T_{amb} \tag{3.8}$$

$$q\big|_{y=H+t_1} = \int \tau_{2\lambda} S_\lambda d\lambda - q_{loss,1} \tag{3.9}$$

$$\begin{aligned} q\big|_{y=H} &= \frac{k_1}{D_1 c_{p1}}\left[\frac{\partial T}{\partial y}\right] + \int \left(1 - e^{-K_{a\lambda,1}(t_1)}\right)\left(q^-_{\lambda(H)} - q^+_{b\lambda[T_{y=H}]}\right) d\lambda \\ \text{where } q^+_{b\lambda[T_{y=H}]} &= 2\pi \int_0^1 I^+_{b\lambda[T_{y=H}]} \phi d\phi \end{aligned} \tag{3.10}$$

Within the nanofluid, the sunlight interacts primarily with nanoparticles through absorption and scattering mechanisms. Interaction of the incident electromagnetic radiation (sunlight) with the nanoparticles could broadly be of two types: radiative and non-radiative decay. Radiative decay involves re-emission of absorbed photon i.e., scattering of the incident photon. On the other hand, non-radiative decay involves conversion of the absorbed photon into the thermal energy of the nanoparticles. Due to the small size of the nanoparticles, the non-radiative decay mechanism is

predominant, i.e., nanoparticles are predominantly absorbers of incident sunlight (Nuemann et al., 2013; Sönnichsen et al., 2002). The RTE provides the value of radiation intensity along the line of sight by accounting for the processes of absorption, emission, and scattering. A numerical method for solving the RTE has been used to calculate the value of intensity at various points in the positive and negative directions. Once the values of intensity in the positive and negative directions are known across the fluid depth, the value of the net heat flux leaving a control volume is computed along with the divergence of radiative flux. The details of the discretization strategy along with procedure for solving radiative transfer equation (RTE) are provided in appendices C and D, respectively.

Once RTE has been solved for initial temperature distribution and the value of divergence is known *'a priori'*; this value of divergence is substituted into the energy equation as energy generation term the values of temperature field at new instant of time are established. Explicit form of finite difference formulation has been used to numerically compute the energy equation. With the solving of the energy equation, a new temperature distribution is obtained for the next time step. Once again, radiation exchange between the plates (as detailed in subsection 3.2.2(e)) and the RTE is solved, and new values of divergence are calculated for input to the energy equation. This process gives a transient temperature distribution at different time intervals, and it is repeated until steady state has been reached. It may be noted that two-way coupling exists between RTE and the energy equation - temperature field calculated using the energy equation (whose solution requires RTE solution as 'a priori') is an input to RTE (to compute the emission term); and output of RTE (which depends on temperature field calculated using the energy equation) forms the input (source term) to the energy equation.

Equations (3.11)–(3.14) represent the governing, initial and boundary conditions for the nanofluid.

$$\frac{\partial T}{\partial t} = \frac{k_{nf}}{D_{nf} c_{p,nf}} \left[\frac{\partial^2 T}{\partial y^2} \right] - \frac{1}{D_{nf} c_{p,nf}} \frac{\partial q_{rad,nf}}{\partial y} + \frac{1}{D_{nf} c_{p,nf}} \frac{\partial q_{trans \to nf}}{\partial y} - u_y \frac{\partial T}{\partial x} \tag{3.11}$$

Here, the first term on the right-hand side is the diffusion term; second and third terms combined represent the source term; the fourth term is the advection term. The values of $q_{\text{trans}\to nf}$ and $q_{rad,nf}$ can be obtained from Eqs. (3.6) and (D10), respectively.

$$T(y)\big|_{t=0} = T_{amb} \tag{3.12}$$

$$q\big|_{y=H} = \frac{k_{nf}}{D_{nf} c_{pnf}} \left[\frac{\partial T}{\partial y} \right] + \int q^{+}_{\lambda[y=H]} d\lambda \tag{3.13}$$

$$q\big|_{y=0} = \int \rho_{\lambda 3} q^{+}_{\lambda[y=0]} d\lambda \tag{3.14}$$

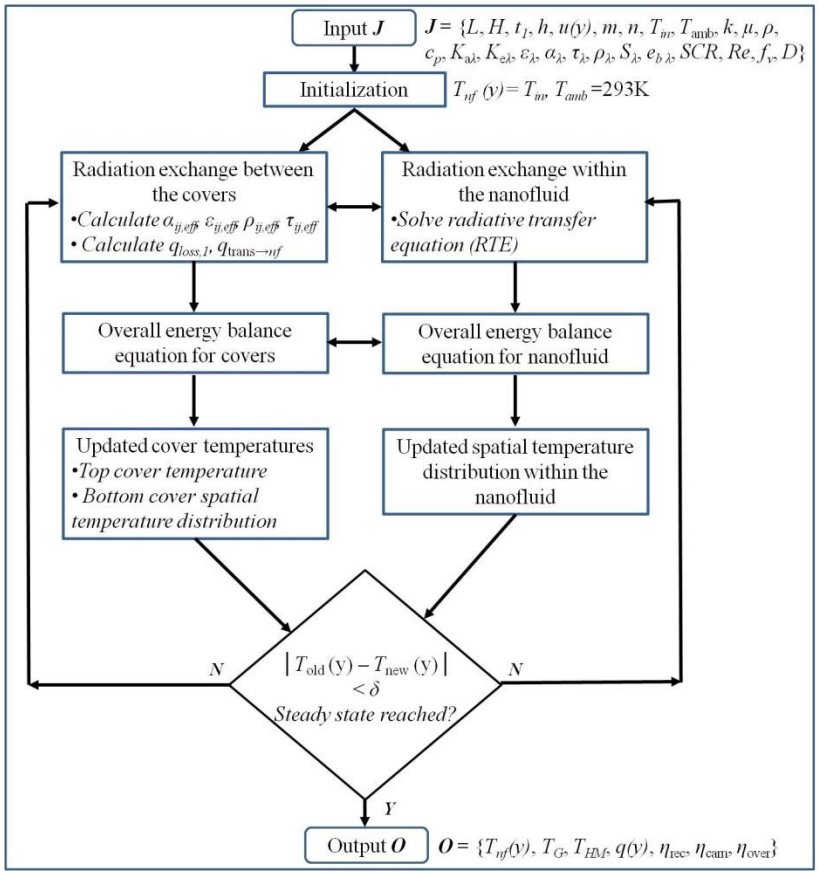

Property/Parameter	Value/Range
Length of receiver [*L*]	8m
Height of receiver [*H*]	0.01m-0.1m
Width of receiver [*W*]	0.07m
Thickness of plate 1 [t_1]	0.002m
Ambient Temperature [T_{amb}]	293K
Inlet fluid temperature [T_{in}]	293K-593K
Heat Transfer coefficient between plate 2 and atmosphere [*h*]	$10 Wm^{-2}K$
Specific heat of nanofluid/ basefluid [$c_{p,nf} = c_{p,bf}$]	$1580 Jkg^{-1}K^{-1}$
Density of nanofluid/basefluid [$D_{nf} = D_{bf}$]	$1000 kgm^{-3}$
Thermal conductivity of nanofluid/basefluid [$k_{nf} = k_{bf}$]	$0.117 Wm^{-1}K^{-1}$
Dynamic viscosity of nanofluid /basefluid [μ]	$0.0708 kgm^{-1}s^{-1}$
Specific heat of plate 1 (glass, solar selective surface and black surface) [c_{p1}]	$840 Jkg^{-1}K^{-1}$, $385 Jkg^{-1}K^{-1}$, and $385 Jkg^{-1}K^{-1}$
Density of plate 1 (glass, solar selective surface and black surface) [D_1]	$4000 kgm^{-3}$, $8933 kgm^{-3}$, and $8933 kgm^{-3}$
Thermal conductivity of plate 1(glass, solar selective surface and black surface) [k_1]	$0.8 Wm^{-1}K^{-1}$, $400 Wm^{-1}K^{-1}$, and $400 Wm^{-1}K^{-1}$
Solar concentration ratio [SCR]	5-100
Reynolds number [*Re*]	100-1600
Nanoparticles volume fraction [f_v]	10^{-7}-10^{-2}

Fig. 3.7: Flowchart to calculate the performance parameters in relation to volumetric absorption-based receivers. An in-house code has been developed in MATLAB® to implement the algorithm.

(h). Surface absorption based solar thermal systems: In this configuration, the sunlight first interacts with the outer cover plate (plate 2, glass/heat mirror) and is subsequently absorbed by the plate 1 (solar selective/black surface). The absorbed energy is then transferred to the fluid through conduction and convection. Radiation exchange between the two cover plates (one semi-transparent and one opaque in case of surface absorption-based receivers) could be handled in a manner like that for volumetric absorption-based receivers. The governing equation and boundary conditions pertinent to the heat transfer processes in plate 1 and 2 are given by equations (3.15)–(3.18).

$$\frac{\partial T}{\partial t} = \frac{k_1}{D_1 c_{p1}}\left[\frac{\partial^2 T}{\partial x^2} + \frac{\partial^2 T}{\partial y^2}\right] + \frac{\int \tau_{2\lambda}\alpha_{1\lambda} S_\lambda d\lambda}{D_1 c_{p1}} \tag{3.15}$$

Here, the first term on the right-hand side is the diffusion term and the second term represents the source term.

$$T(y)\big|_{t=0} = T_{amb} \tag{3.16}$$

$$q\big|_{y=H+t_1} = \int \tau_{2\lambda} S_\lambda d\lambda - q_{loss,1} \tag{3.17}$$

$$q\big|_{y=H} = \frac{k_1}{D_1 c_{p1}}\left[\frac{\partial T}{\partial y}\right] \tag{3.18}$$

The temperature distribution across the conduit depth and length is found by solving the overall energy equation [Eq. (3.19)] subject to initial and boundary conditions [Eqs. (3.20) – (3.22)].

$$\frac{\partial T}{\partial t} = \frac{k_f}{D_f c_{p,f}}\left[\frac{\partial^2 T}{\partial y^2}\right] - u_y \frac{\partial T}{\partial x} \tag{3.19}$$

Here, the first and second terms on the right-hand side represent diffusion and advection terms, respectively.

$$T(y)\big|_{t=0} = T_{amb} \tag{3.20}$$

$$q\big|_{y=H} = \frac{k_f}{D_f c_{p,f}}\left[\frac{\partial T}{\partial y}\right] \tag{3.21}$$

$$q\big|_{y=0} = \frac{k_f}{D_f c_{p,f}}\left[\frac{\partial T}{\partial y}\right] = 0 \tag{3.22}$$

All the differential equations have been solved numerically using explicit form of finite difference technique. The details of the grid independence test and validation of the developed numerical models has been presented in appendices C and E, respectively.

3.3 Natural convection in cavities

In the study of natural convection in cavities, two scenarios are considered: (a). cavities heated from the side and (b). cavities heated from the bottom.

3.3.1 Constructional details

Figure 3.8 shows the schematic of a 2d cavity heated volumetrically from the side (a) and bottom (b). Cavity heated from the side has a transmitting glass wall on the left vertical side and an isothermal opaque wall on the right vertical side. Radiation enters the transparent glass wall (x = 0) and is absorbed by the liquid inside the cavity. Any radiation which is unabsorbed by the fluid layer is assumed to be directly absorbed by the opaque wall on the right ($x = L$). The top and bottom horizontal walls are assumed adiabatic.

Cavity heated from the bottom has a transmitting glass wall at the bottom and an isothermal opaque wall at the top. Radiation enters the transparent glass wall (y = 0) and is absorbed by the liquid inside the cavity. Any radiation which is unabsorbed by the fluid layer is assumed to be directly absorbed by the opaque wall on the top ($y = H$). The side walls are assumed adiabatic.

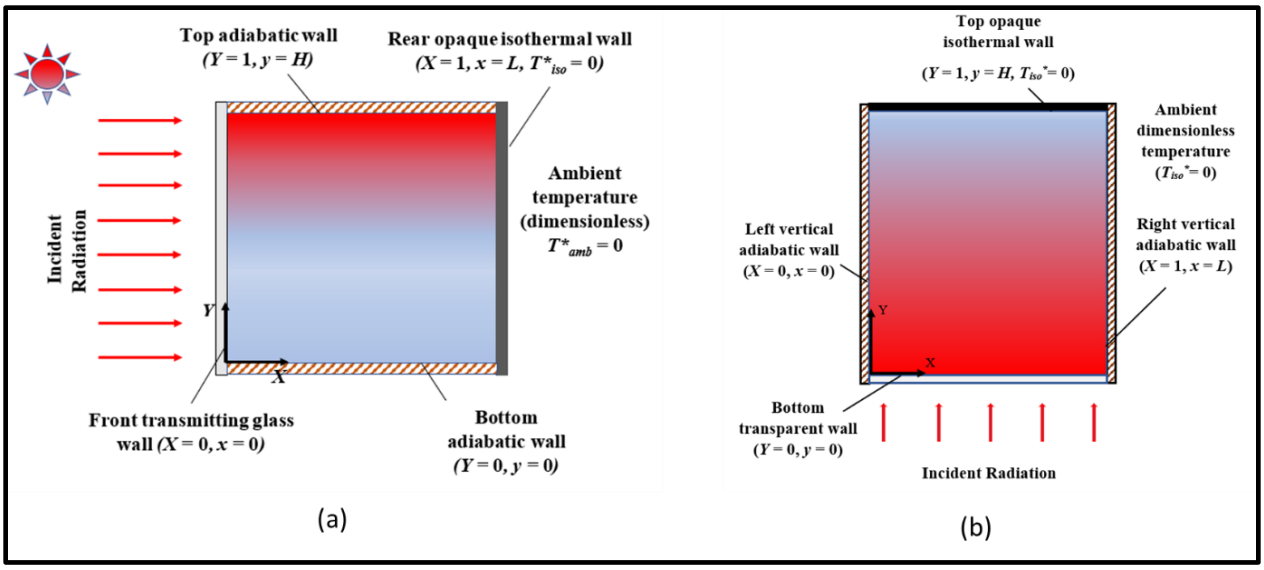

Fig. 3.8: Volumetric heating of fluid confined in a cavity (a) irradiated from side (b) irradiated from below.

3.3.2 Theoretical modeling framework

(a). Assumptions

The following assumptions were made while developing the theoretical model:

- The fluid in the cavity is assumed to be Newtonian.
- The flow is assumed to be two-dimensional, steady, and laminar.
- Thermophysical properties are assumed to be unchanging with temperature.
- Incident flux is assumed to strike normally at the transparent vertical side wall / horizontal bottom wall of the cavity.
- Emission and scattering of incident radiation by fluid layers has been neglected and heating of fluid layers is assumed to be taking place by absorption of incident radiation in accordance with Beer lambert law This is a valid assumption as the temperature rise of the confined fluid is not drastic enough and any radiation emitted is in the long wavelength range which is readily absorbed by the working fluid. This is consistent with the previous experimental as well as theoretical studies reported in the literature.

- The vertical side/ top horizontal wall facing the transmitting wall has been assumed to be completely black which can absorb any unattenuated radiation passing through the participating medium and is assumed to be isothermal.
- The fluid in the cavity is modeled as single phase semi-transparent medium.
- Boussinesq approximation is invoked.

(b). Mathematical model

The governing equations for incompressible two-dimensional fluid flow and energy in Cartesian co-ordinates are as follows:

$$\frac{\partial u}{\partial x}+\frac{\partial v}{\partial y}=0 \tag{3.23}$$

$$\frac{\partial u}{\partial t}+u\frac{\partial u}{\partial x}+v\frac{\partial u}{\partial y}=-\frac{1}{D_l}\frac{\partial p}{\partial x}+\upsilon\left[\frac{\partial^2 u}{\partial x^2}+\frac{\partial^2 u}{\partial y^2}\right] \tag{3.24}$$

$$\frac{\partial v}{\partial t}+u\frac{\partial v}{\partial x}+v\frac{\partial v}{\partial y}=-\frac{1}{D_l}\frac{\partial p}{\partial y}+\upsilon\left[\frac{\partial^2 v}{\partial x^2}+\frac{\partial^2 v}{\partial y^2}\right]+gB(T-T_0) \tag{3.25}$$

$$\frac{\partial T}{\partial t}+u\frac{\partial T}{\partial x}+v\frac{\partial T}{\partial y}=a_l\left[\frac{\partial^2 T}{\partial x^2}+\frac{\partial^2 T}{\partial y^2}\right]-\frac{\partial F}{\partial x} \quad \text{(Side heating)} \tag{3.26(a))}$$

$$\frac{\partial T}{\partial t}+u\frac{\partial T}{\partial x}+v\frac{\partial T}{\partial y}=a_l\left[\frac{\partial^2 T}{\partial x^2}+\frac{\partial^2 T}{\partial y^2}\right]-\frac{\partial F}{\partial y} \quad \text{(Bottom heating)} \tag{3.26(b))}$$

where '$\partial F/\partial x$' and '$\partial F/\partial y$' are the source terms.

Initial conditions:

$$t=0:\ T=0;\ u=v=0 \tag{3.27}$$

Boundary conditions:

Transparent side glass wall:

$$x = 0 :\ u = v = 0 ;\ \ - \frac{dT_g}{dx} = \frac{h}{k_g}(T_g - T_0) \qquad \text{(Side heating)} \qquad (3.28(a))$$

Transparent bottom glass wall:

$$x = 0 :\ u = v = 0 ;\ \ - \frac{dT_g}{dy} = \frac{h}{k_g}(T_g - T_0) \qquad \text{(Bottom heating)} \qquad (3.28(b))$$

Isothermal rear wall-liquid interface:

$$x = L :\ u = v = 0 ;\ T = T_{amb} \qquad \text{(Side heating)} \qquad (3.28(c))$$

Isothermal top wall-liquid interface:

$$x = L :\ u = v = 0 ;\ T = T_{amb} \qquad \text{(Bottom heating)} \qquad (3.28(d))$$

Adiabatic bottom wall:

$$y = 0 :\ u = v = 0 ;\ \ \frac{dT}{dy} = 0 \qquad \text{(Side heating)} \qquad (3.28(e))$$

Adiabatic top wall:

$$Y = H :\ u = v = 0 ;\ \ \frac{dT}{dy} = 0 \qquad \text{(Side heating)} \qquad (3.28(f))$$

Adiabatic left wall:

$$x = 0 :\ u = v = 0 ;\ \ \frac{dT}{dx} = 0 \qquad \text{(Bottom heating)} \qquad (3.28(g))$$

Adiabatic right wall:

$$X = L:\ u = v = 0;\ \frac{dT}{dx} = 0 \qquad \text{(Bottom heating)} \qquad (3.28(h))$$

Similarly, the one-dimensional equation for energy transfer in the glass wall is given by Eq. (3.29). The transmitting wall is assumed very thin and as such heat transfer through conduction is considered one-dimensional.

$$\frac{\partial T}{\partial t} = a_g \left[\frac{\partial^2 T_g}{\partial x_g^2}\right] - \frac{\partial \phi}{\partial x_g} \qquad \text{(Side heating)} \qquad (3.29(a))$$

$$\frac{\partial T}{\partial t} = a \left[\frac{\partial^2 T_g}{\partial y_g^2}\right] - \frac{\partial \phi}{\partial y_g} \qquad \text{(Bottom heating)} \qquad (3.29(b))$$

The above equations are further non-dimensionalised and the following equations are obtained:

$$\frac{\partial U}{\partial X} + \frac{\partial V}{\partial Y} = 0 \qquad (3.30)$$

$$\frac{\partial U}{\partial t^*} + U\frac{\partial U}{\partial X} + V\frac{\partial U}{\partial Y} = -\frac{\partial P}{\partial X} + Pr\left[\frac{\partial^2 U}{\partial X^2} + \frac{\partial^2 U}{\partial Y^2}\right] \qquad (3.31)$$

$$\frac{\partial V}{\partial t^*} + U\frac{\partial V}{\partial X} + V\frac{\partial V}{\partial Y} = -\frac{\partial P}{\partial Y} + Pr\left[\frac{\partial^2 V}{\partial X^2} + \frac{\partial^2 V}{\partial Y^2}\right] + Ra^*.Pr.T^* \qquad (3.32)$$

$$\frac{\partial T^*}{\partial t^*} + U\frac{\partial T^*}{\partial X} + V\frac{\partial T^*}{\partial Y} = \left(\frac{\partial^2 T^*}{\partial X^2} + \frac{\partial^2 T^*}{\partial Y^2}\right) - \frac{\partial e^{-EX}}{\partial X} \qquad \text{(Side Heating)} \qquad (3.33(a))$$

$$\frac{\partial T^*}{\partial t^*} + U\frac{\partial T^*}{\partial X} + V\frac{\partial T^*}{\partial Y} = \left(\frac{\partial^2 T^*}{\partial X^2} + \frac{\partial^2 T^*}{\partial Y^2}\right) - \frac{\partial e^{-EY}}{\partial Y} \qquad \text{(Bottom Heating)} \qquad (3.33(b))$$

Initial conditions:

$$T^* = 0;\ U = V = 0 \qquad (3.34)$$

Boundary conditions:

Transparent front glass wall:

$$X = 0 : U = V = 0 ; \; - \frac{dT^*}{dX} = Bi^* (T^* - T^*_{amb}) \qquad \text{(Side heating)} \qquad (3.35(a))$$

Transparent bottom glass wall:

$$Y = 0 : U = V = 0 ; \; - \frac{dT^*}{dY} = Bi^* (T^* - T^*_{amb}) \qquad \text{(Bottom heating)} \qquad (3.35(b))$$

Isothermal rear wall:

$$X = 1 : U = V = 0 ; \; T^* = 0 \qquad \text{(Side heating)} \qquad (3.35(c))$$

Isothermal rear wall:

$$Y = 1 : U = V = 0 ; \; T^* = 0 \qquad \text{(Bottom heating)} \qquad (3.35(d))$$

Adiabatic bottom wall:

$$Y = 0 : U = V = 0 ; \; \frac{dT^*}{dY} = 0 \qquad \text{(Side heating)} \qquad (3.35(e))$$

Adiabatic top wall:

$$Y = 1 : U = V = 0 ; \; \frac{dT^*}{dY} = 0 \qquad \text{(Side heating)} \qquad (3.35(f))$$

Adiabatic left-side wall:

$$X = 0 : U = V = 0 ; \; \frac{dT^*}{dX} = 0 \qquad \text{(Bottom heating)} \qquad (3.35(g))$$

Adiabatic right-side wall:

$$X = 1 : U = V = 0 ; \ \frac{dT^*}{dX} = 0 \qquad \text{(Bottom heating)} \qquad (3.35(h))$$

To solve the incompressible NS equations, a code was written in MATLAB® to implement the solution algorithm (SOLA) for staggered grid framework. Once the velocity distribution is obtained – it is substituted in the energy equation to find the temperature distribution. The explicit method is implemented, and the above steps are repeated till the final steady state solution is reached. The flowchart in Fig. 3.9 lays out the procedure for building the mathematical model.

Also appendix F and G provide the validation of the mathematical model and the results of grid independence test.

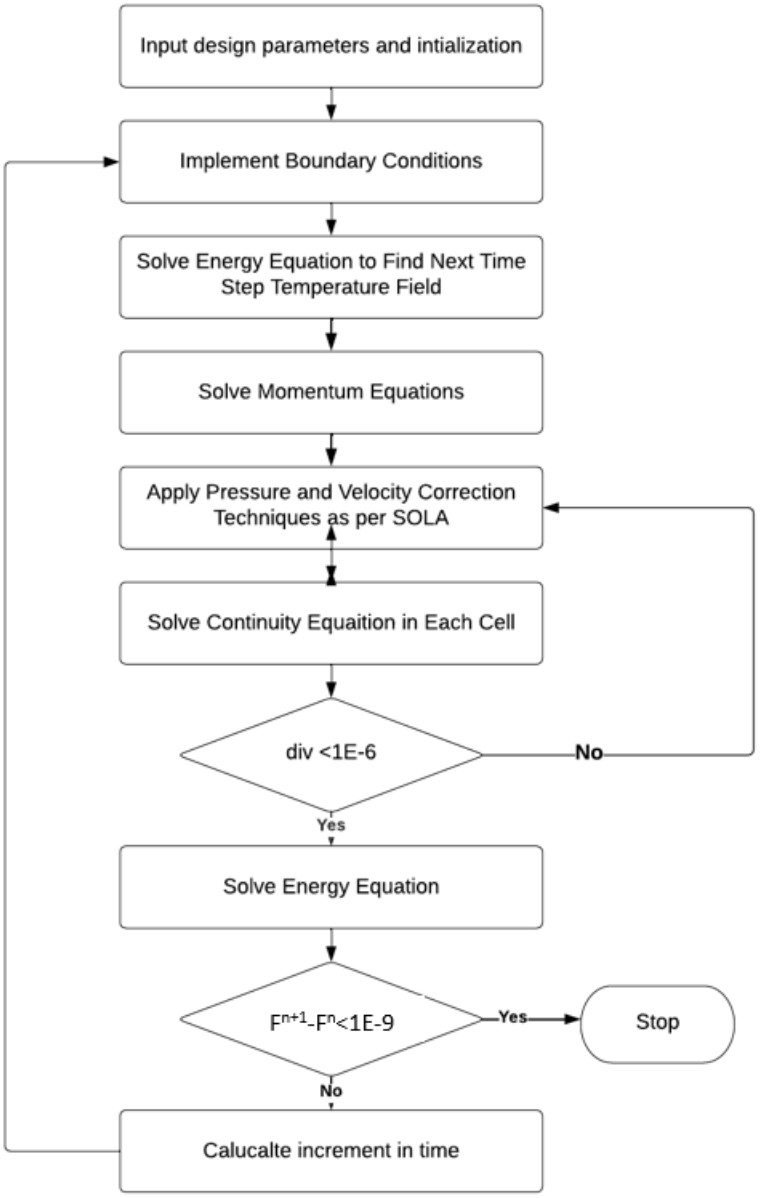

Fig. 3.9: Flowchart showing the methodology employed in the study of natural convection in cavities.

4. Results & Discussion

4.1 Aims

In this chapter the results of the study are presented and thereafter analyzed with respect to their applicability in solar thermal systems The chapter is divided into two sections: the *first* section deals with the results from the study of forced convection in a channel irradiated from the top employed as a solar receiver; the *second* section deals with the results from the study of natural convection in closed cavities irradiated from the side and bottom. The temperature and flow distributions in various systems, their dependence on the different parameters and their effect on the performance characteristics of the system are examined.

4.2 Forced convection in channels

This section delves into several aspects related to the working of volumetric absorption-based systems and surfaces absorption-based systems which include the impact of enveloping surfaces, volume fraction of nanoparticles (in case of volumetric systems), solar concentration ratios, Reynolds number, and inlet fluid temperatures on the performance characteristics of solar thermal receivers based on volumetric and surface absorption-based systems.

4.2.1 Performance characteristics of volumetric and surface absorption-based systems

The performance parameters, viz. receiver, Carnot, and overall efficiencies are considered to evaluate the performance of volumetric and surface absorption-based receivers. Moreover, attempt has been made to identify the key operating, constructional, and design parameters or/and the combination of these parameters which affects the performance characteristics the most.

The performance parameters, viz. receiver, Carnot, and overall efficiencies are defined by Eqs. (4.1), (4.2), and (4.3), respectively.

$$\eta_{rec} = \frac{\rho c_p \int_0^H u_y \left(T_{y,ex} - T_{y,in}\right) dy}{L \int S_\lambda d\lambda} \tag{4.1}$$

$$\eta_{carn} = 1 - \left(\frac{T_{amb}}{T_{ex,avg}} \right) \tag{4.2}$$

$$\eta_{over} = \eta_{rec} . \eta_{carn} . \eta_{II} \tag{4.3}$$

where η_{II} is the second-law efficiency (which accounts for irreversibilities in the power generation cycle) whose value is taken as 0.66 (Lenert & Wang, 2012).

4.2.2 Study parameters

Table 4.1 shows the different parameters and the range in which they are varied in studying forced convection in a channel which is irradiated from the top. The liquid flowing through the channel is heated through volumetric as well as surface absorption of radiation. Four different designs of receivers constructed with different enveloping surfaces are studied including two designs of volumetric absorption-based systems where the fluid flows through a glass channel enveloped by a glass/ heat mirror and two designs of surface absorption-based systems where fluid flows through a channel whose top surface is black/ solar selective enveloped by a heat mirror/ glass, respectively.

Table 4.1: Parameters of the study on forced convection in a channel.

Parameters	**Range**
Solar Concentration ratio (abbr. SCR, number of suns)	5-100
Reynolds Number (*Re*)	100-1600
Nanoparticle volume fraction	10^{-7} - 10^{-2}
Inlet fluid temperature (*K*)	293 - 593
Height of channel (*m*)	0.01 – 0.1

4.2.3 Effect of nanoparticle volume fraction on the receiver efficiency of volumetric absorption-based systems

Figure 4.1 shows surface plots for the two volumetric absorption-based receiver designs (of a given height, H = 0.07m). At a given solar concentration ratio (SCR) and Reynolds number (*Re*), the receiver efficiency initially increases with increase in volume fraction of the nanoparticles and

attains a maximum value at an optimum value (10^{-5} in the present case) beyond which it decreases. This is because at very low volume fractions, radiation remains un-captured by the absorbing fluid whereas at very high volume-fractions most of the radiation is captured near the surface (emulating surface absorption) and does not percolate down to the lower fluid layers in the receiver. This leads to lower average bulk fluid temperatures and higher thermal losses at the top surface. This is consistent with experimental (Otanicar et al., 2010; Singh and Khullar, 2019) as well as modeling results (Otanicar et al., 2010; Sharaf et al., 2018b) reported in the literature. At high SCR (= 25) and low Reynolds number (= 200), the receiver efficiency decreases steeply at values of volume fraction higher than the optimum. This decrease is more pronounced in case of G-G design owing to high thermal losses relative to the G-HM design. It was found that for a given receiver height (0.07m), the value of the optimum nanoparticles volume fraction is independent of SCR, *Re* and receiver design.

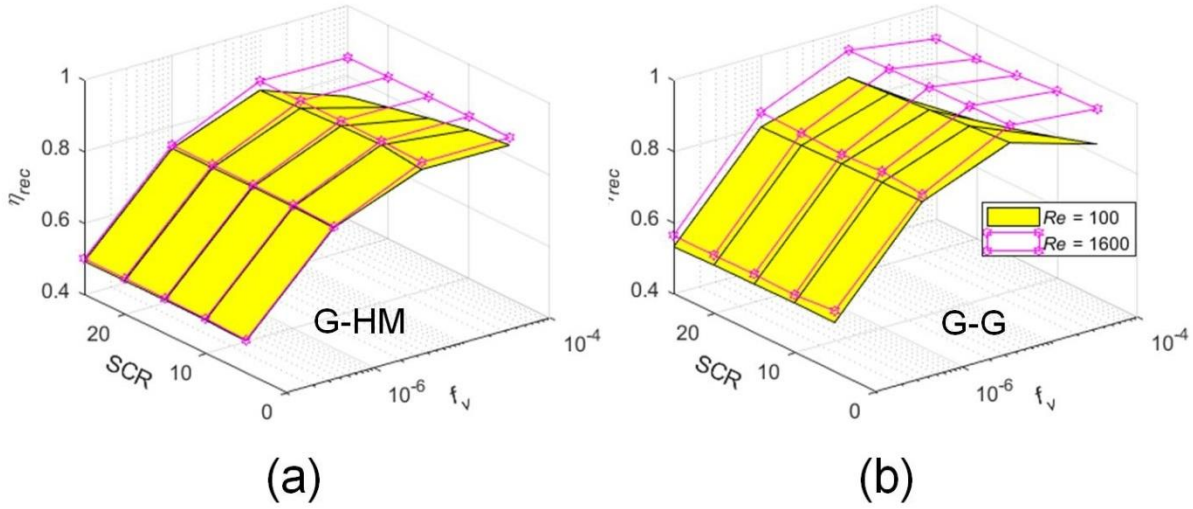

Fig. 4.1: Effect of nanoparticles volume fraction on receiver efficiency for volumetric absorption-based receivers: (a) G-HM design, and (b) G-G design.

4.2.4 Effect of conduit height on the receiver efficiency of volumetric absorption-based systems

Figure 4.2 shows the effect of conduit height over a range of nanoparticles volume fraction for the two volumetric absorption-based receiver designs. For a given receiver design, the value of optimum nanoparticles volume fraction increases with decrease in conduit height. It was observed

that at lower volume fraction of nanoparticles, the receiver efficiency increases with increase in conduit height and this trend reverses at higher volume fractions. This is because at lower volume fractions radiation remains unabsorbed, and increasing the conduit height helps with greater absorption of the radiation leading to better efficiency while at higher volume fraction of particles, radiation is captured close to the surface leading to more losses. Figure 4.3 further shows that at higher volume fraction, the temperature at the surface is higher and the system simulates surface heating. This is consistent with the observations reported in the literature (Lenert & Wang, 2012), where the effect of receiver height was studied only at a single nanoparticles volume fraction.

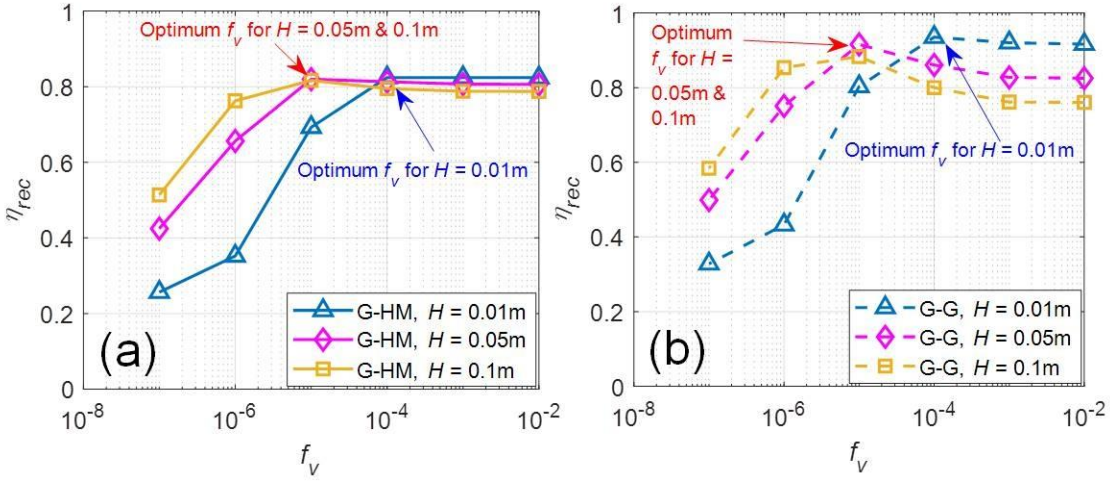

Fig. 4.2: Effect of conduit height on receiver efficiency of VAR designs: (a) G-HM, and (b) G-G. SCR = 5, *Re* = 100.

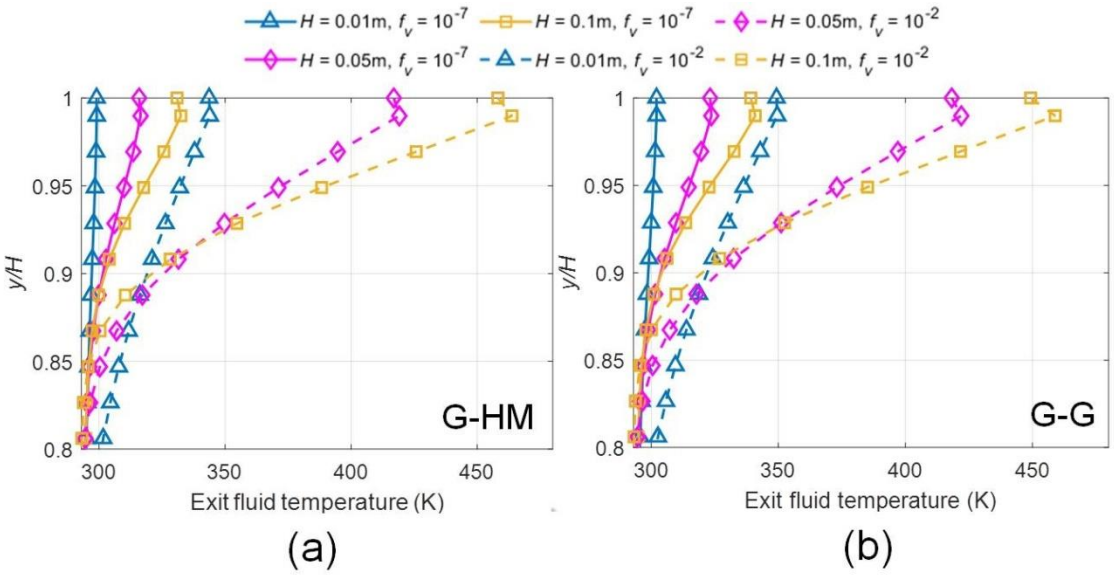

Fig. 4.3: Effect of conduit height on the temperature distribution in VAR designs: (a) G-HM, and (b) G-G. SCR = 5, *Re* = 100.

4.2.5 Effect of Reynolds number and solar concentration ratio on the receiver efficiencies of volumetric and surface absorption based receivers

Figure 4.4 gives contour plots showing receiver efficiencies for a range of solar concentration ratios and Reynolds numbers for different designs of volumetric and surface absorption-based systems at a fixed inlet fluid temperature (T_{in} = 293K). In all cases higher efficiencies are obtained at higher Reynolds numbers and lower solar concentration ratios due to lower thermal losses incurred. However, the surface absorption-based systems are more sensitive to the variation of SCR and *Re* as the surface of the systems quickly reaches high temperatures because of the creation of a thermal barrier between the surface and fluid. It is also observed that designs with heat mirror casings perform better than the designs with glass casings at high concentration ratios and low rate of fluid flow - conditions when the temperatures at the top surface are exorbitantly high resulting in emission of radiation of relatively shorter wavelengths which is reflected by the heat mirror casing.

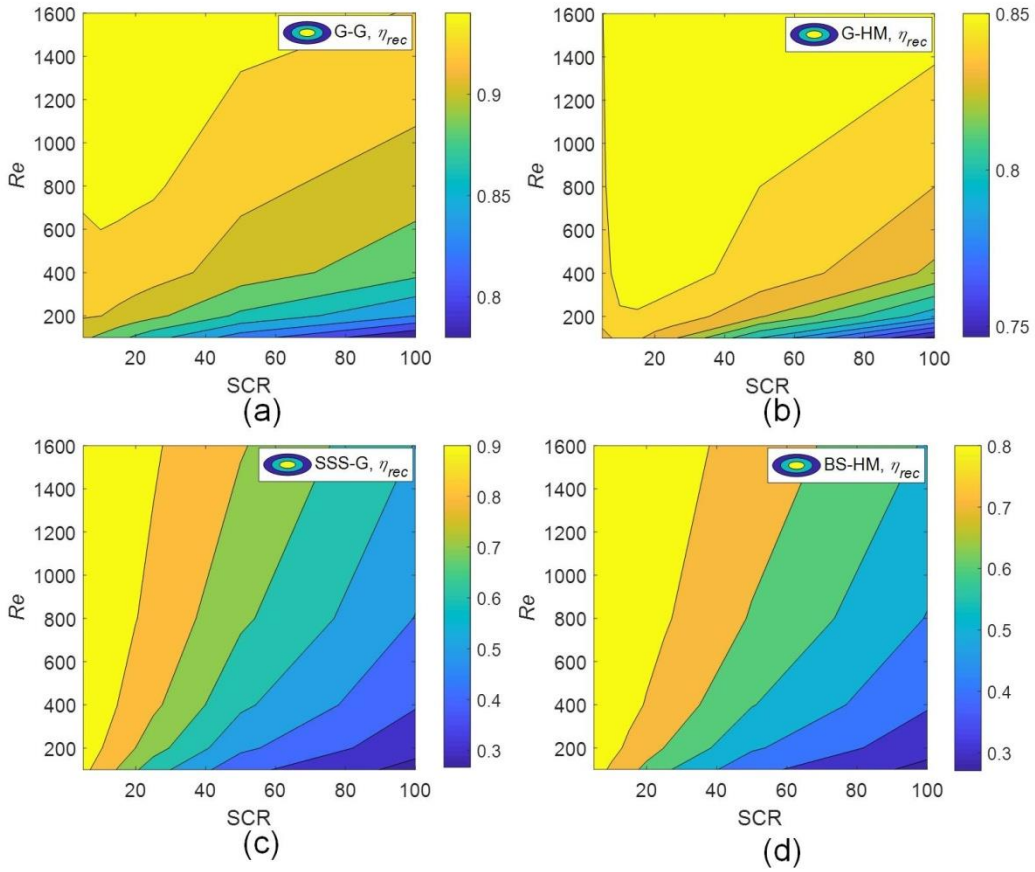

Fig. 4.4: Effect of Reynolds number and SCR on receiver efficiency of VARs and SARs: (a) G-G, (b) G-HM, (c) SSS-G, and (d) BS-HM.

4.2.6 Effect of inlet fluid temperature on receiver and overall efficiencies of volumetric and surface absorption based receivers

Figure 4.5 compares the receiver and overall efficiencies for the two designs of volumetric absorption-based systems (i.e., the glass-heat mirror (G-HM) and the glass-glass (G-G) design) at *Re* = 100 and 1600 for two solar concentration ratios (=5 and 100) at different inlet fluid temperatures. At low inlet fluid temperature, the designs with glass casings fare better (in terms of receiver efficiency) compared to heat mirror casings but the scenario reverses as the efficiency of glass cased systems drops steeply as compared to heat mirror casings. The critical inlet fluid temperature at which the receiver efficiency for G-HM exceeds the G-G design depends strongly on solar concentration ratio and *Re*, and shifts to higher values of inlet fluid temperatures at higher values of concentration ratios and *Re*. This is because the effectiveness of heat mirrors is exhibited

when the magnitude of the radiative losses (which the heat mirror curbs) is high which occurs at high fluid temperatures and low Reynolds numbers. Throughout the range of inlet fluid temperatures, the two receiver designs involve similar order of magnitude of average fluid temperatures - resulting in similar Carnot efficiencies and hence the overall efficiencies. However, at low SCR (= 5) and high inlet fluid temperatures there is a conspicuous difference in the overall efficiency of glass-heat mirror design due to higher receiver efficiencies.

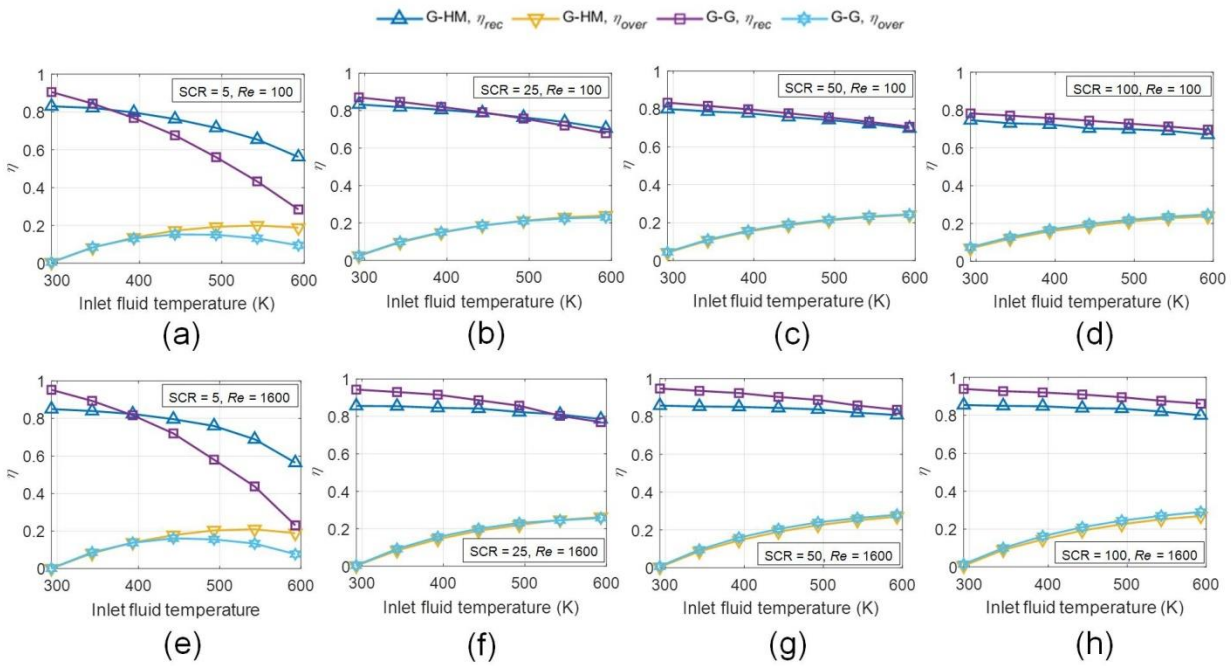

Fig. 4.5: Comparison of receiver, and overall efficiencies at different inlet fluid temperatures in case of VARs (a) SCR = 5, *Re* = 100 (b) SCR = 25, *Re* = 100 (c) SCR = 50, *Re* = 100, (d) SCR = 100, *Re* = 100, (e) SCR = 5, *Re* = 1600 (f) SCR = 25, *Re* = 1600 (g) SCR = 50, *Re* = 1600, and (h) SCR = 100, *Re* = 1600;

Figure 4.6 compares the receiver efficiency and overall efficiency for two designs of surface absorption-based receivers (i.e., the black surface-heat mirror (BS-HM) and the solar selective surface-glass (SSS-G) design) for two SCRs (5 and 100) at *Re* = 100 and 1600 at different inlet fluid temperatures. At low Reynolds number (*Re* = 100), the receiver efficiencies are considerably lower than volumetric systems even at low inlet fluid temperatures and they further decrease with increase in inlet fluid temperatures and concentration ratio. This is because at low Reynolds numbers and high solar concentration ratios, a staggering amount of thermal energy gets

accumulated at the surface due to low convection rates at low Reynolds number - the fluid is unable to take this energy with it, therefore resulting in huge temperature overheat (i.e., surface temperatures are significantly higher than the temperature of the fluid layer in contact with it). This leads to escalation of thermal losses. Similar trends are observed at high Reynolds number as well. However, the magnitudes of temperature overheat, and emission losses are diminished as compared to the case of low *Re*.

Although, the receiver efficiency is higher for solar selective surface-glass design for nearly the entire range of inlet fluid temperatures due to the high transmissivity of glass casing for visible light, the efficiency curves for the two designs (SSS-G and BS-HM) tend to converge at high inlet fluid temperatures particularly at high solar concentration ratio (> 25). The receiver efficiencies are lower for the case of BS-HM design because of the lower amount of incident radiation that passes through to the receiver as heat mirrors have lower solar weighted transmissivity. Also, due to the presence of a solar selective surface in the SSS-G design, the radiation emitted by a solar selective surface is much lower than it is for a black surface in the BS-HM design. But at higher inlet fluid temperatures and concentration ratios, losses due to radiation increase which is minimized due to use of heat mirror in the BS-HM design, thus bringing its efficiency closer to that of SSS-G which lacks provisions to prevent radiation losses at high temperatures. The overall efficiency curves follow the trends like those observed in case of volumetric absorption-based systems.

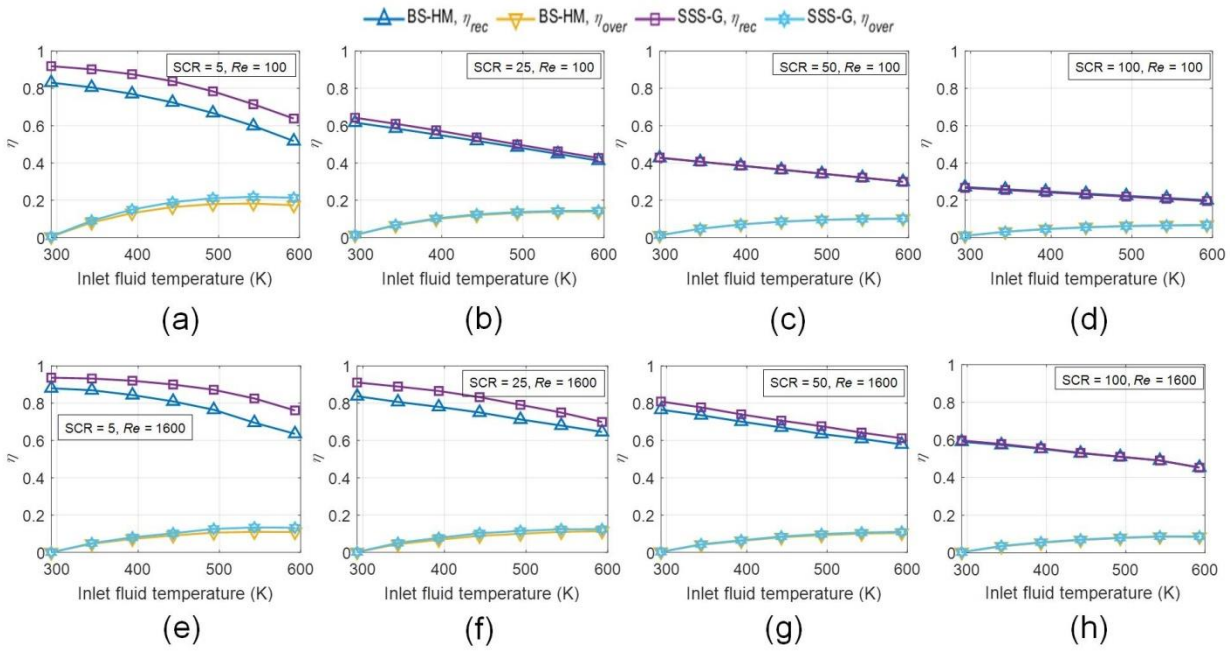

Fig. 4.6: Comparison of receiver, and overall efficiencies at different inlet fluid temperatures in case of SARs (a) SCR = 5, *Re* = 100 (b) SCR = 25, *Re* = 100 (c) SCR = 50, *Re* = 100, (d) SCR = 100, *Re* = 100, (e) SCR = 5, *Re* = 1600 (f) SCR = 25, *Re* = 1600 (g) SCR = 50, *Re* = 1600, and (h) SCR = 100, *Re* = 1600.

4.2.7 Delineating optimal range of operating and design parameters for volumetric and surface absorption based receivers: The overall picture

Figure 4.7 shows how receiver efficiencies compare between volumetric (i.e. the black surfaces-heat mirror and the solar selective surface-glass) and surface absorption based systems (i.e. the glass-heat mirror and the glass-glass design). It is seen that as the solar concentration ratios increase, the receiver efficiencies drop rapidly for surface absorption-based receivers (both for T_{in} = 293K and 593K). Whereas, in case of VARs, two distinct trends are observed: while efficiencies decrease slightly or (remain almost constant) at low inlet fluid temperatures (T_{in} = 293K); at high inlet fluid temperatures (T_{in} = 593K), efficiencies first increase and then stagnate with increase in solar concentration ratios.

Similar trends are observed in case of overall efficiencies (Fig. 4.8); there is an enhancement of 15%–18% in volumetric systems over surface absorption-based systems. This is a significant

improvement in relation to solar thermal platforms - narrowing the gap between solar thermal and fossil fuel-based systems.

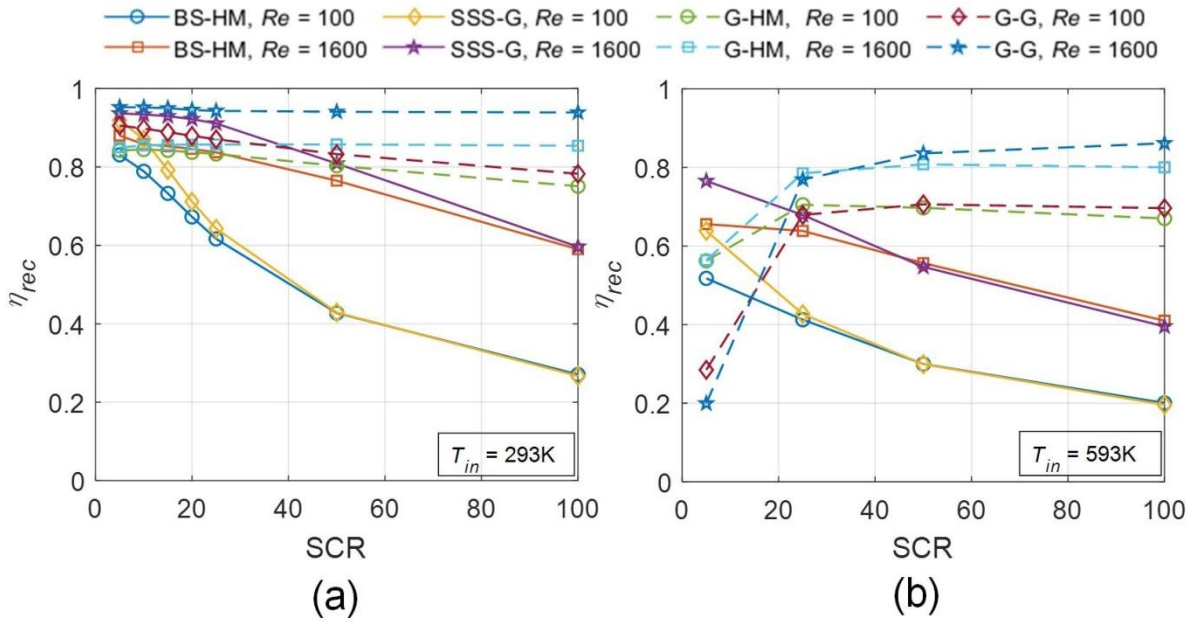

Fig. 4.7: Difference in efficiencies between volumetric and surface absorption based receivers (a) receiver efficiency, T_{in} = 293K, and (b) receiver efficiency, T_{in} = 593K.

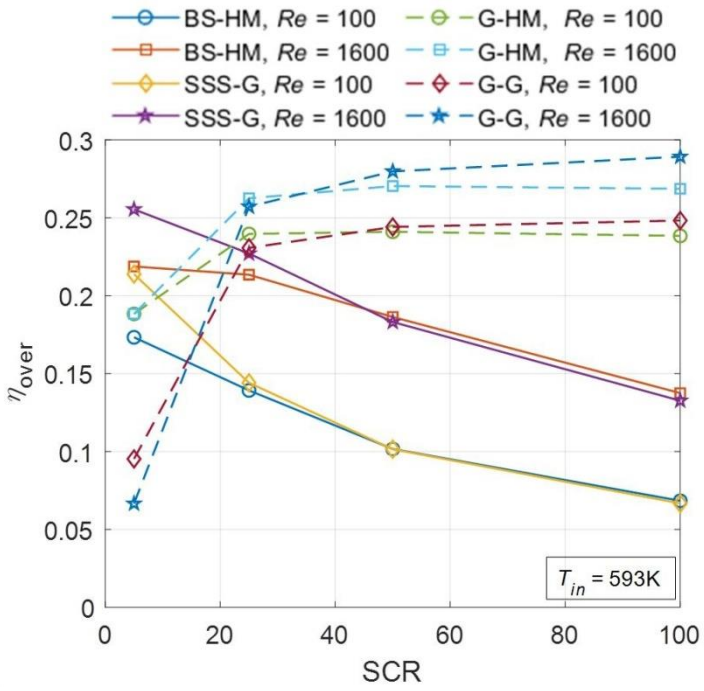

Fig. 4.8: Difference in overall efficiencies between volumetric and surface absorption based receivers, T_{in} = 593K.

To understand the heat transfer mechanisms involved in volumetric and surface absorption-based systems, the exit temperature field for these at different Reynolds numbers and inlet fluid temperatures are plotted. Figure 4.9 compares the exit temperature field plots for black surface-heat mirror design (surface absorption-based receiver) with those of glass-heat mirror design (volumetric absorption-based receiver). These two cases were chosen as they are similar in all aspects except for the mechanisms of heat transfer involved. One can see that the maximum temperature for the case of surface absorption-based system is at the surface and there is a very steep difference in temperature between the surface and the topmost layer of the fluid in contact with it (i.e., significant overheat temperature exists). On the contrary, the temperature of the top glass plate for the case of VAR design is lower than the temperature of topmost layer of fluid in the conduit (i.e., there exists a temperature inversion in case of VARs) which leads to lower emission losses and better distribution of energy across the fluid layers – resulting in higher efficiencies for volumetric absorption-based receivers.

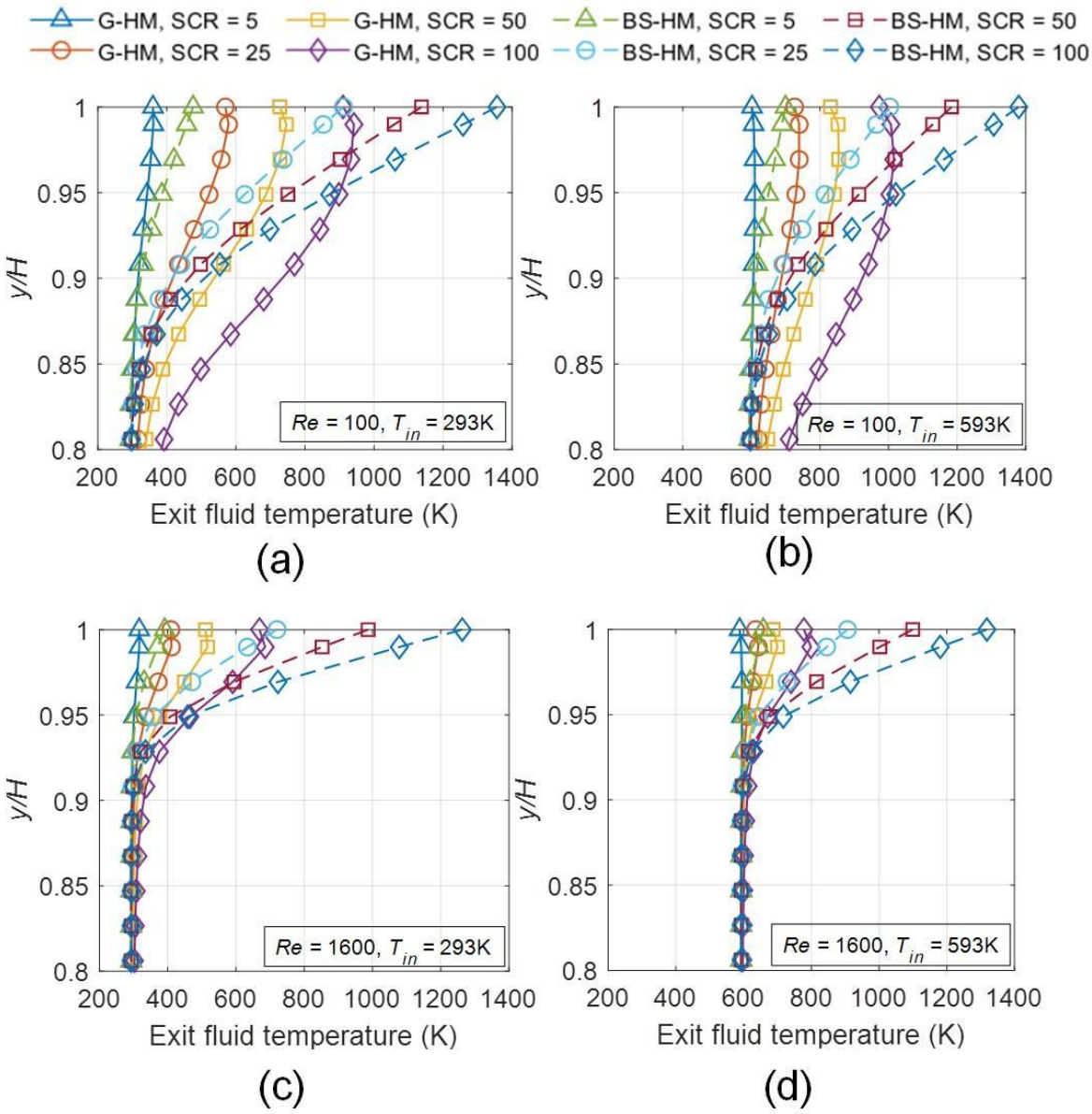

Fig. 4.9: Comparison of exit temperature distribution between volumetric and surface absorption based receivers (a) Re = 100, T_{in} = 293K (b) Re = 100, T_{in} = 593K (c) Re = 1600, T_{in} = 293K, and (d) Re = 100, T_{in} = 593K.

Receiver efficiency enhancements of ~45% @Re = 1600 to 51% @ Re = 100 could be achieved in case of VARs relative to their SAR counterparts at SCR = 100.

Table 4.2 presents a performance comparison of different designs in various operating regimes. Depending on the operating conditions, appropriate VAR/SAR design variant should be chosen to ensure high receiver efficiencies in solar thermal systems.

Table 4.2: Receiver efficiencies for VAR/SAR design variants in various operating regimes.

@ T_{in} = 293K	***Re* = 200**	***Re* = 1600**
SCR ≤ 25	$\eta_{G\text{-}G} > \eta_{SSS\text{-}G} > \eta_{G\text{-}HM} > \eta_{BS\text{-}HM}$	$\eta_{G\text{-}G} > \eta_{SSS\text{-}G} > \eta_{BS\text{-}HM} > \eta_{G\text{-}HM}$
25 < SCR ≤ 100	$\eta_{G\text{-}G} > \eta_{G\text{-}HM} > \eta_{SSS\text{-}G} > \eta_{BS\text{-}HM}$	$\eta_{G\text{-}G} > \eta_{G\text{-}HM} > \eta_{SSS\text{-}G} > \eta_{BS\text{-}HM}$
@ T_{in} = 593K	***Re* = 200**	***Re* = 1600**
SCR ≤ 15	$\eta_{SSS\text{-}G} > \eta_{G\text{-}HM} > \eta_{BS\text{-}HM} > \eta_{G\text{-}G}$	$\eta_{SSS\text{-}G} > \eta_{BS\text{-}HM} > \eta_{G\text{-}HM} > \eta_{G\text{-}G}$
15 < SCR ≤ 25	$\eta_{G\text{-}HM} > \eta_{G\text{-}G} > \eta_{SSS\text{-}G} > \eta_{BS\text{-}HM}$	$\eta_{G\text{-}HM} > \eta_{G\text{-}G} > \eta_{SSS\text{-}G} > \eta_{BS\text{-}HM}$
25 < SCR ≤ 100	$\eta_{G\text{-}G} \approx \eta_{G\text{-}HM} > \eta_{SSS\text{-}G} \approx \eta_{BS\text{-}HM}$	$\eta_{G\text{-}G} > \eta_{G\text{-}HM} > \eta_{SSS\text{-}G} > \eta_{BS\text{-}HM}$

4.3 Natural convection in cavities

4.3.1 Study parameters

Table 4.3 shows the different parameters and the range in which they are varied in studying natural convection in a cavity heated volumetrically through a transparent wall. Two cases have been considered: cavity heated from the side wall and from the bottom wall. The side of cavity facing the transparent wall is considered isothermal while the other two walls are adiabatic.

Table 4.3: Parameters of the study on natural convection in a cavity.

Dimensionless Parameters	**Values (Side heating)**	**Values (Bottom heating)**
E	0.1, 1, 1.33, 2, 4, 10, 100	0.1, 1, 1.33, 2, 4, 10, 100
Ra*	10^3, 10^4, 10^5, 10^6, 10^7, 10^8	10^2, 10^3, 10^4, 10^5
Pr	0.01, 0.1, 1, 10, 100, 1000	0.01, 0.1, 1, 10, 100, 1000
Bi*	0, 1, 2, 3, 4, 5	0, 1, 2, 3, 4, 5
AR	0.1, 0.5, 1, 2, 10	0.1, 0.5, 1

4.3.2 Techniques used for visualization of results in the study of natural convection in cavities

a). Streamlines

Streamlines are lines joining points with equal stream function values (Ψ = constant) and are tangential to the flow. Once the temperature and velocity flow distribution at steady state is yielded, the stream function at various points is calculated as follows:

$$\psi_{X,Y=0} = \psi_{X=0,Y=0} - \int_0^X VdX \tag{4.4}$$

$$\psi_{X,Y} = \psi_{X,Y=0} + \int_0^Y UdY \tag{4.5}$$

The value of $\Psi_{X=0,\ Y=0}$ is arbitrarily taken as zero.

b). *Isotherms*

Isotherms are lines passing through points of equal temperature (T^* = constant). They can be easily obtained once the temperature distribution is known. In a system where conduction is the dominant mode of heat transfer, the direction of heat transfer is perpendicular to the isotherms. However, in a convection dominated scenario, isotherms are not sufficient to provide a clear picture of the situation as heat transfer depends on the mass transfer. This is where heatlines come into picture which are discussed next.

c). *Heatlines*

Heatlines are useful in the study of heat transfer and are analogous to streamlines in the field of fluid flow. Just as streamlines depict the direction of fluid flow, heatlines show the direction of energy transfer. They are especially important for the case of convection related problems as the transport of energy rides upon the flow of fluid which is different from conduction dominated problems where the energy flow is perpendicular to the isotherms as already discussed previously.

Like streamlines, heat function '$\mathscr{H}$' can be defined in terms of energy flow in 'x-' and 'y-' directions. The tangent of the energy vector is the route of energy transfer i.e., heatline (Tao et al., 2019).

$$\frac{\partial \mathscr{H}}{\partial y} = \xi_x \tag{4.6}$$

$$-\frac{\partial \mathscr{H}}{\partial x} = \xi_y \tag{4.7}$$

In the conventional derivation of heat function for drawing heatlines from the energy equation, there is no source term involved. However, in the present study the concept of heatlines is extended to study natural convection caused due to volumetric heating wherein an energy generation term is a part of the energy equation (Mukhopadhyay et al., 2002).

The steady state energy equation is given as follows:

$$u\frac{\partial T}{\partial x}+v\frac{\partial T}{\partial y}=\alpha_l\left(\frac{\partial^2 T}{\partial x^2}+\frac{\partial^2 T}{\partial y^2}\right)+\frac{\partial \phi}{\partial x} \tag{4.8}$$

$$\Rightarrow \frac{\partial}{\partial x}\left(\rho c_p uT-k\frac{\partial T}{\partial x}-\rho c_p \phi\right)+\frac{\partial}{\partial y}\left(\rho c_p vT-k\frac{\partial T}{\partial y}\right)=0 \tag{4.9}$$

The heat function then becomes,

$$\frac{\partial \mathcal{H}}{\partial y}=\rho c_p u(T-T_{ref})-k\frac{\partial T}{\partial x}-\rho c_p \phi \text{ (Energy flow in x-direction)} \tag{4.10}$$

$$-\frac{\partial \mathcal{H}}{\partial x}=\rho c_p v(T-T_{ref})-k\frac{\partial T}{\partial y} \text{ (Energy flow in y-direction)} \tag{4.11}$$

The dimensionless heat function for the present problem is defined as follows:

$$\frac{\partial \mathcal{H}^*}{\partial Y}=\left(UT^*-\frac{\partial T^*}{\partial X}+e^{-EX}\right) \text{ (Energy flow in X-direction)} \tag{4.12}$$

$$-\frac{\partial \mathcal{H}^*}{\partial X}=VT^*-\frac{\partial T^*}{\partial Y} \text{ (Energy flow in Y-direction)} \tag{4.13}$$

such that,

$$\mathcal{H}^*_{X,Y=0}=\mathcal{H}^*_{X=0,Y=0}-\int_0^X\left(VT^*-\frac{\partial T^*}{\partial Y}\right)dX \tag{4.14}$$

$$\mathcal{H}^*_{X,Y}=\mathcal{H}^*_{X,Y=0}+\int_0^Y\left(UT^*-\frac{\partial T^*}{\partial X}+e^{-EX}\right)dY \tag{4.15}$$

The value of $\mathcal{H}_{X=0,\ Y=0}$ is arbitrarily taken to be zero.

4.3.3 Cavity heated volumetrically from side: Results

The results of the study on cavity heated from side have been divided into two sections. Section 4.3.2.1 deals with the results from heating the cavity with uniformly distributed flux whereas section 4.3.2.2 deals with linearly varying heat flux. While the total flux remains the same in both cases, in the case of linearly varying flux two orientations have been considered: first, where heat flux varies linearly with zero flux at the bottom of the cavity till maximum flux at the top of the cavity; second, where heat flux varies linearly with zero flux at the top of the cavity to maximum flux at the bottom of the cavity.

4.3.3.1 Uniformly distributed heat flux

This section looks at the effect of uniformly distributed heat flux (UDHF) on the temperature and flow distribution in the cavity and how it depends upon the Rayleigh and Prandtl numbers, the optical thickness of the fluid, the convective flux at the transmitting wall, the aspect ratio of the cavity etc. The Rayleigh number is varied from 10^2 to 10^8. The Prandtl number is varied from 0.01 to 1000. The values of optical thickness are 0.1, 1, 1.33, 2, 4, 10 and 100. The convective heat loss from glass wall is regulated by varying the value of Bi^* from 0 to 5. The value of aspect ratio is varied from very low to very high. The different values considered are 0.1, 0.5, 1, 2 and 10.

However, not all the results for different permutations of the variables have been presented as doing so would make the manuscript lengthy. For this study, a base case was taken where Ra=10^6, Pr=10, E=2, Bi^* = 3 and AR = 1. The results of variation in the different parameters are considered individually while keeping the values of other parameters constant.

(a). Effect of Optical thickness of fluid layer

This section looks at how optical thickness of the fluid layer (or fluid opacity) affects the isotherms, streamlines and the flux at the isothermal and the transmitting glass wall. Numerical analysis was carried out for different values of E (=0.1, 1, 1.33, 2, 4, 10 and 100). Streamlines (Fig. 4.10), isotherms (Fig. 4.11), heatlines (Fig. 4.12), convective heat flux at isothermal wall (Fig. 4.13(a)) and flux at glass wall (Fig. 4.13(b)) were plotted for the previously mentioned values of E. Fig. 4.13(c) shows the temperature at midline (Y=0.5) along X for different values of E.

Effect on streamlines

As the optical thickness increases, the value of maximum stream function first increases to 13.35 at *E=4* after which it decreases. As the optical thickness increases, more energy is deposited in liquid layers which generates a convective motion of the fluid as a larger proportion of the incident energy is absorbed by the liquid as opposed to being directly absorbed by the isothermal wall. The boundary layer thickness near the transmitting wall decreases with higher values of *E* and the central core expands as is evident from the streamlines (Fig. 4.10). However, as *E* increases further, the value of the maximum stream function decreases as the radiation is absorbed close to the transmitting wall and is not able to penetrate sufficiently deep into the cavity to create a buoyant lift.

Effect on isotherms

As *E* increases, the boundary layer close to the transmitting wall grows progressively thinner as is observed from the isotherms (Fig. 4.11). The maximum temperature in the cavity continues to increase as the optical thickness increases. Also, the maximum temperature moves closer to the transmitting wall as *E* is increased which is obvious as more and more energy is accumulated in a thin region close to the transmitting wall.

Effect on heatlines

The heatlines for different values of optical thickness (*E*) are shown in Fig. 4.12. The Rayleigh and Prandtl number values are fixed (at $Ra = 10^6$ and $Pr = 10$). At very low values of '*E*', the heatlines are horizontal as most of the incident radiation passes unabsorbed through the cavity. This is not explicitly evident from the streamlines and the isotherms and shows how heatlines help in providing a clearer picture which forms the basis for understanding the thermal mechanism. As '*E*' continues to increase, the pattern of heatlines begins to resemble the streamline pattern which is obvious as convection becomes the dominant mode of heat transfer. The value of heat function is maximum at *E = 1,* after which it begins to decrease.

Effect on local convective heat flux at isothermal wall and the heat loss at glass wall

Convective heat flux at the isothermal wall and the transmitting glass wall has been calculated and plotted (Fig. 4.13(a)). The following equation gives the convective heat flux at different values of cavity height.

$$q^*(Y) = -\frac{\partial T^*}{\partial X_{(X=1)}} \tag{4.16}$$

As the fluid opacity increases, the convective heat flux at the isothermal wall also increases up to a point. The maximum convective heat flux is observed at *E=4.* At *E=10*, the convective heat flux is lower (Fig. 4.13(a)).

The heat loss at the transmitting glass wall is the heat lost to atmosphere. As glass wall is at a higher temperature than the surroundings, it loses heat through convection and radiation. The following equation gives the heat flux lost at the glass wall for different values of cavity height.

$$q_g^*(Y) = Bi^*.\Delta T^*_{X=0} \tag{4.17}$$

Where ΔT^*_Y *is* the dimensionless temperature difference between glass wall and atmosphere at height *Y.*

The flux at the transmitting glass wall goes on increasing as *E* increases (Fig. 4.13(b)). This can be explained through Fig. 4.13(c) which shows the variation in mid-line ($Y = 0.5$) dimensionless temperature along *X* for variable *E* (= 0.1, 1, 4, 10, 100). As *E* increases from 0.1 to 4, the mid-line temperature increases as well at all values of *X* in the cavity. However, for $E = 10$, the mid-line dimensionless temperature is higher than that for $E = 4$, close to the transmitting wall and it is lower towards the opaque isothermal wall. The same happens for the case when $E = 10$ as well. As the values of *E* rise higher, energy is absorbed in fluid layers close to the transmitting wall and it does not penetrate the inner fluid layers to raise them buoyantly.

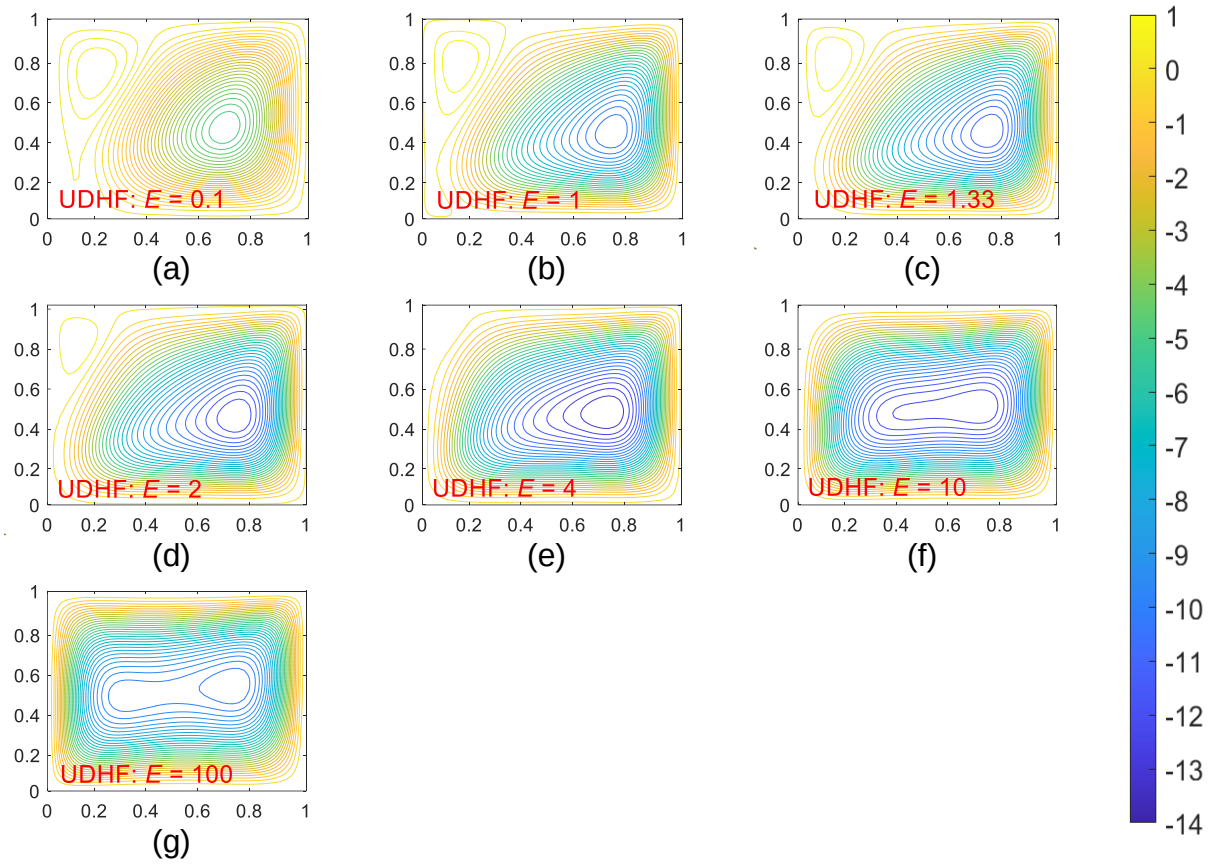

Fig. 4.10: Effect of optical thickness on flow structure (streamlines) ($Ra = 10^6$, $Pr = 10$, $Bi^* = 3$, $AR = 1$): (a). $E = 0.1$, $|\Psi_{max}| = 5.0805$ (b). $E = 1$, $|\Psi_{max}| = 10.61$ (c). $E = 1.33$, $|\Psi_{max}| = 11.34$ (d). $E = 2$, $|\Psi_{max}| = 12.28$ (e). $E = 4$, $|\Psi_{max}| = 13.35$ (f). $E = 10$, $|\Psi_{max}| = 12.63$ (g). $E = 100$, $|\Psi_{max}| = 10.01$.

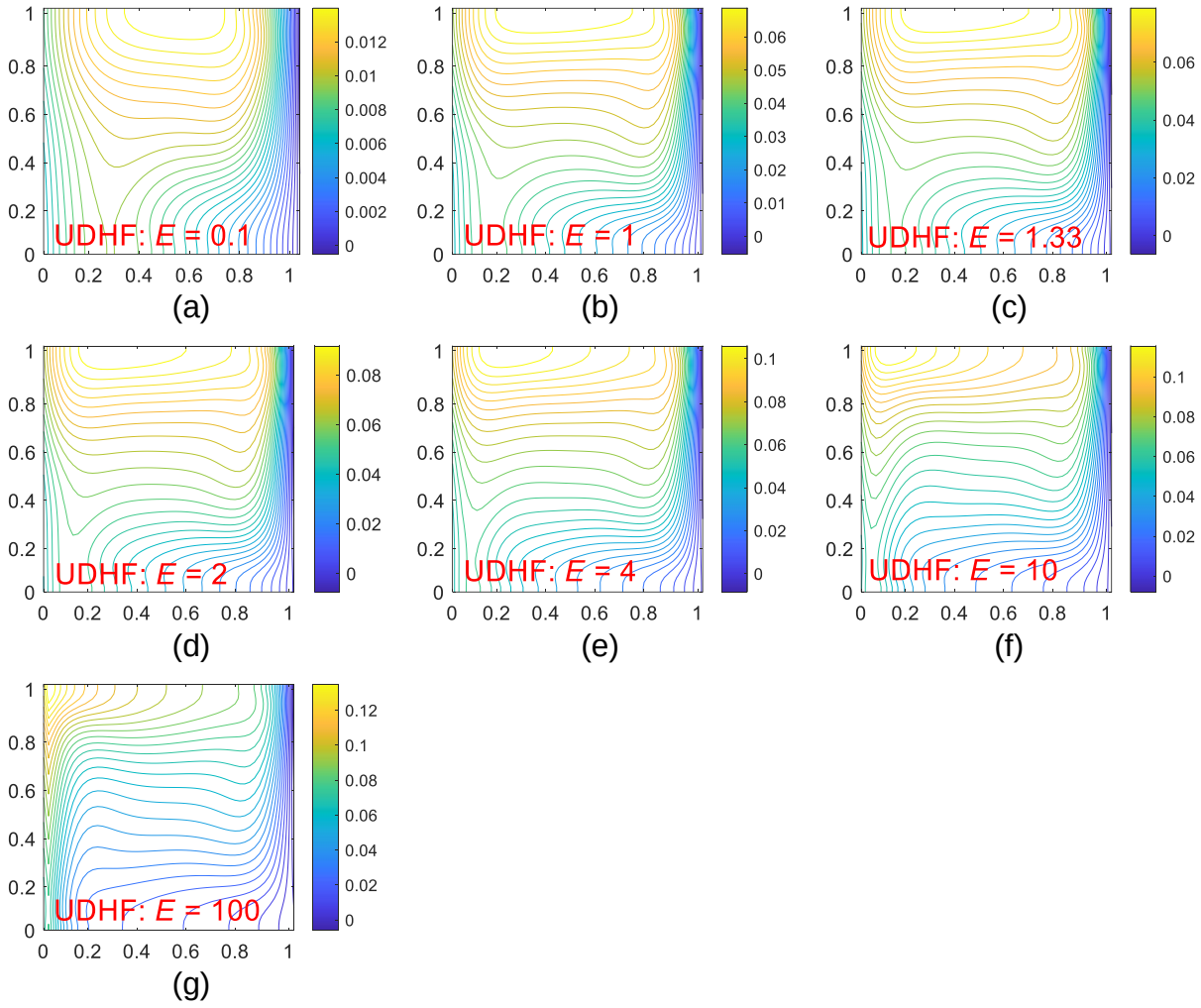

Fig. 4.11: Effect of optical thickness on temp. distribution (isotherms) ($Ra = 10^6$, $Pr = 10$, $Bi^* = 3$, $AR = 1$): (a). $E = 0.1$, $T_{max} = 0.0145$ (b). $E = 1$, $T_{max} = 0.07$ (c). $E = 1.33$, $T_{max} = 0.08$ (d). $E = 2$, $T_{max} = 0.095$ (e). $E = 4$, $T_{max} = 0.11$ (f). $E = 10$, $T_{max} = 0.12$ (g). $E = 100$, $T_{max} = 0.14$.

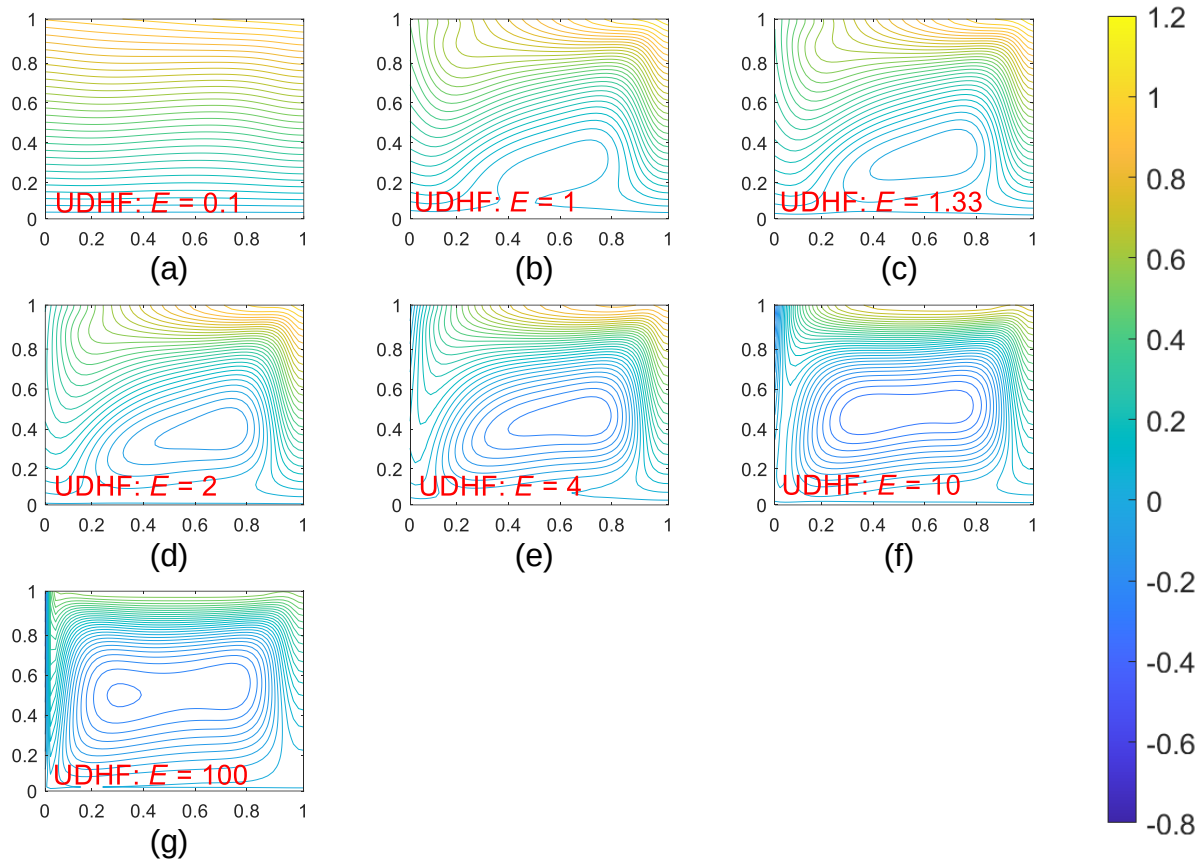

Fig. 4.12: Effect of optical thickness on heatlines ($Ra = 10^6$, $Pr = 10$ $Bi^* = 3$, $AR = 1$): (a). $E = 0.1$, $H_{max} = 1.022$ (b). $E = 1$, $H_{max} = 1.095$ (c). $E = 1.33$, $H_{max} = 1.091$ (d). $E = 2$, $H_{max} = 1.06$ (e). $E = 4$, $H_{max} = 0.94$ (f). $E = 10$, $H_{max} = 0.76$ (g). $E = 100$, $H_{max} = 0.565$.

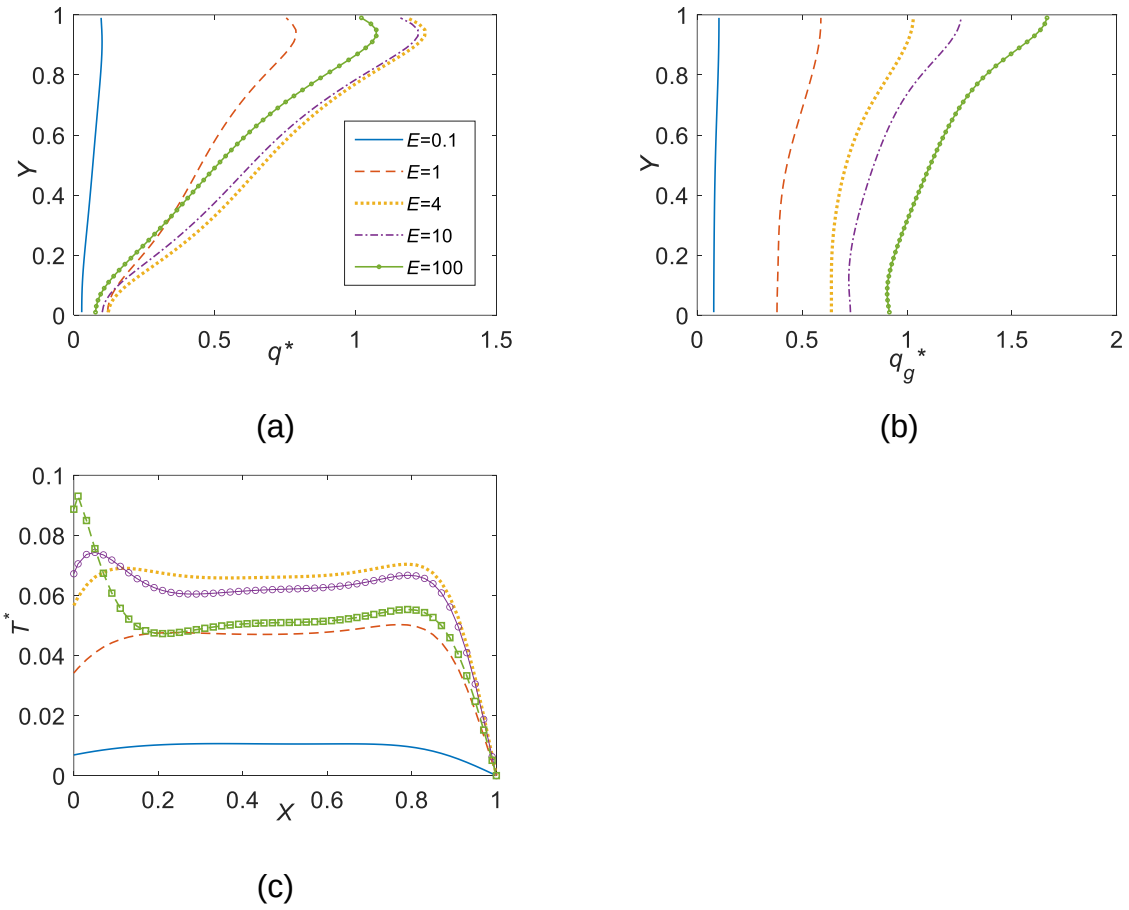

Fig. 4.13: Effect of optical thickness on (a). local convective heat flux at isothermal wall (b). flux lost through glass wall ($Ra = 10^6$, $Pr = 10$, $Bi^* = 3$, $AR = 1$) (c). Mid-line dimensionless temperature ($Y = 0.5$) along X for variable E ($Ra = 10^6$, $Pr = 10$, $Bi^* = 3$, $AR = 1$).

(b). Effect of Rayleigh Number

This section looks at how Rayleigh number affects the temperature and flow distribution and the local convective heat flux at the isothermal wall for the cavity. Calculations were performed for Ra=10^2, 10^3, 10^4, 10^5, 10^6, 10^7 and 10^8. Streamlines (Fig. 4.14), isotherms (Fig. 4.15) and heatlines (Fig. 4.16) were generated to analyze the flow pattern in the cavity and the temperature distribution. Fig. 4.17 shows the effect of Rayleigh number on local convective heat flux and the flux at glass wall. On the left side of the streamline and isotherm plots is the transmitting wall and on the right side is the isothermal wall.

There is a gradual transition observed from a conduction dominated flow pattern to a convection dominated one as *Ra* increases from 10^2 to 10^8.

Effect on streamlines

Fig. 4.14 shows the effect of Rayleigh number on streamlines. For low Rayleigh numbers ($Ra \leq 10^2$), a centro-symmetrical structure of streamlines is observed. A narrow gap between streamlines denotes a steeper change in the stream function between two points at the same distance. As *Ra* increases, the centro-symmetrical structure becomes more and more skewed and there is a higher concentration of streamlines close to the isothermal wall (right). This starts to get more pronounced at $Ra=10^5$ and continues to increase up to $Ra=10^8$. Since the glass wall absorbs very little radiation and gets heated up mainly from conduction due to its proximity with the fluid in the cavity, the temperature at the glass wall is lower than that of the first layer of fluid in the cavity (right next to the transmitting wall). Another reason for lower temperature of the transmitting glass wall is that it loses energy to the surroundings through convection and radiation. A secondary vortex is formed at the upper left corner of the cavity which becomes thinner and more elongated as *Ra* increases. At the transmitting wall, the flow gets separated from the wall as it moves upwards; this separation happens at a lower height at low *Ra.* This happens because as the fluid moves upwards along the cooler wall, it flows against gravity and loses momentum causing it to deviate away from the wall into the cavity where it mixes with fluid which is at higher temperature. As *Ra* increases, the fluid flowing upwards along the transmitting wall carries its momentum to a greater height and separation occurs at a higher level. Thus, the momentum exchange causes the 'humps' in the streamlines.

Effect on isotherms

For low Rayleigh numbers ($Ra \leq 10^2$), the isotherms (Fig. 4.15) are vertical indicating conduction dominated flow; as *Ra* increases, the isotherms start becoming horizontal as is expected in a convection dominated flow. Thus, just as can be inferred from the streamlines for different *Ra* numbers – distinct regimes are observed in the isotherm plots as well; there is a conduction dominated regime ($Ra \leq 10^2$), a transition regime ($10^3 \leq Ra \leq 10^4$), and a convection dominated regime ($Ra > 10^4$). In the convection dominated regime, a thermally stratified core is seen similar to the case of cavity with differentially heated walls. The transition to turbulent convection which

is likely to occur as *Ra* increases has not been included in this study. The critical modified Rayleigh number at which transition to turbulent regime occurs for the physical system modeled in the present study has not been studied in the literature. Since the physics involved in heating the fluid contained within a cavity through direct absorption of incident radiation by the working fluid as opposed to heating the fluid in a cavity with differentially heated walls is quite dissimilar, the Rayleigh number corresponding to transition in the latter case cannot be applied to the former. The results obtained in this study have shown a laminar character in the flow up to $Ra = 10^8$.

Effect on heatlines

At low Rayleigh numbers when conduction dominates – the heatlines appear horizontal (Fig. 4.16). As Rayleigh number increases – the heatlines form a hump in the middle which develops into a loop which means that the energy transport takes place in a circular motion. Furthermore, a boundary layer begins to appear at the isothermal wall where the heatlines are clustered close together. Also, as Rayleigh number increases, the heatline pattern begins to resemble the pattern of streamlines. As energy transport is mainly due to convection at higher Rayleigh numbers. The maximum value of heat function continues to increase as the Rayleigh number increases.

Effect on local convective heat flux at isothermal wall and heat lost at glass wall

There is very little variation in convective heat flux at isothermal wall with Y at $Ra = 10^3$. As Ra increases and convection dominated regime builds up, a large variation in the convective flux at the top and bottom of the cavity is observed. At the top of the cavity the heat flux is maximum as heated fluid impinges against the adiabatic top wall of the cavity (Y=1).

As Rayleigh number increases, the heat lost from glass wall decreases, this happens because due to natural convection setting up at higher Rayleigh numbers, the glass wall gets cooled due to the liquid current thus decreasing the temperature of the glass wall and hence the heat flux.

Thus, an increase in Rayleigh number facilitates the increase in useful heat gain (through the isothermal wall) and minimizes the heat loss through the glass wall.

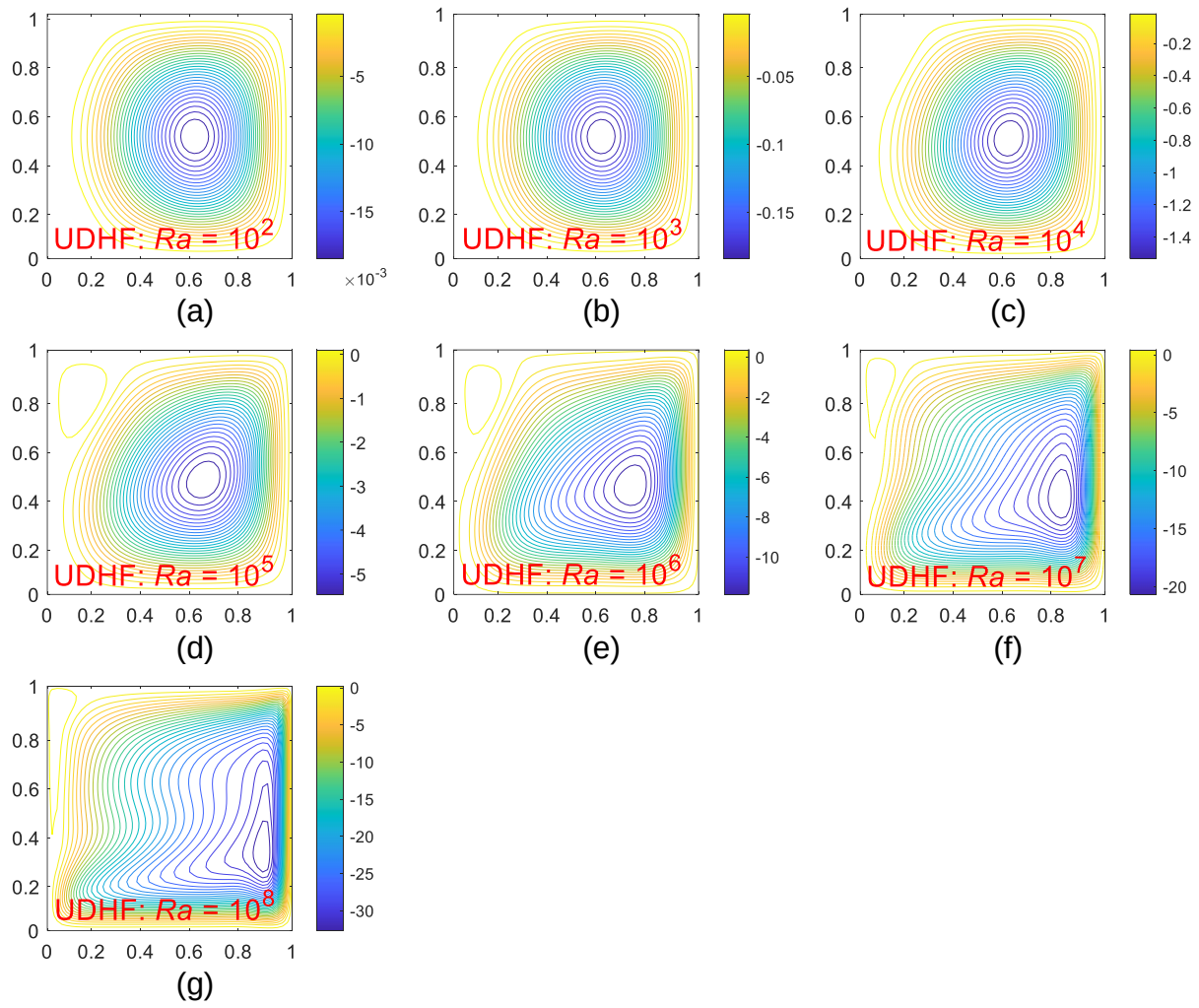

Fig. 4.14: Effect of Rayleigh number on flow structure (streamlines) ($Pr = 10$, $E = 2$, $Bi^* = 3$, $AR = 1$): (a). $Ra = 10^2$, $|\Psi_{max}| = 0.019$ (b). $Ra = 10^3$, $|\Psi_{max}| = 0.19$ (c). $Ra = 10^4$, $|\Psi_{max}| = 1.58$ (d). $Ra = 10^5$, $|\Psi_{max}| = 5.64$ (e). $Ra = 10^6$, $|\Psi_{max}| = 12.28$ (f). $Ra = 10^7$, $|\Psi_{max}| = 21.37$ (g). $Ra = 10^8$, $|\Psi_{max}| = 33.81$.

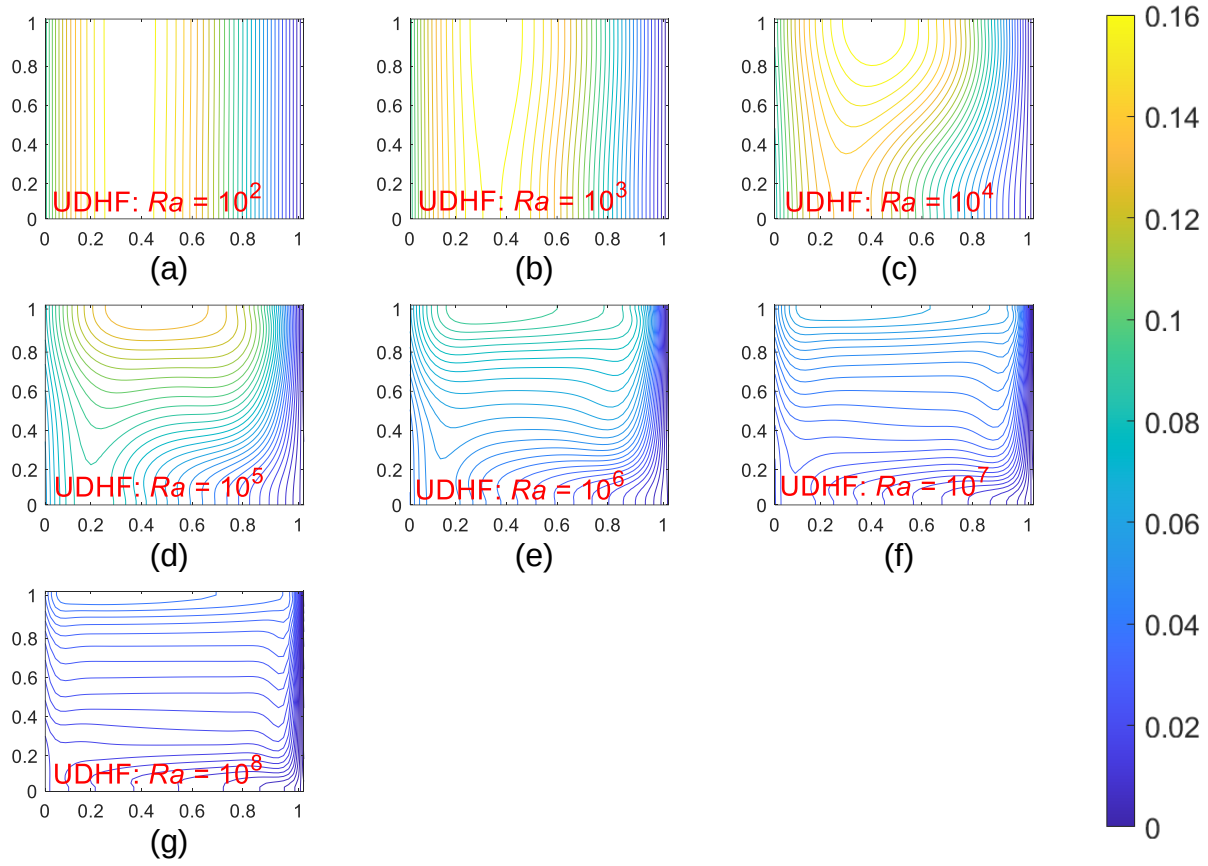

Fig. 4.15: Effect of Rayleigh number on temperature distribution (isotherms) ($Pr = 10$, $E = 2$, $Bi^* = 3$, $AR = 1$): (a). $Ra = 10^2$, $T_{max} = 0.1634$ (b). $Ra = 10^3$, $T_{max} = 0.1753$ (c). $Ra = 10^4$, $T_{max} = 0.17$ (d). $Ra = 10^5$, $T_{max} = 0.13$ (e). $Ra = 10^6$, $T_{max} = 0.095$ (f). $Ra = 10^7$, $T_{max} = 0.06$ (g). $Ra = 10^8$, $T_{max} = 0.04$.

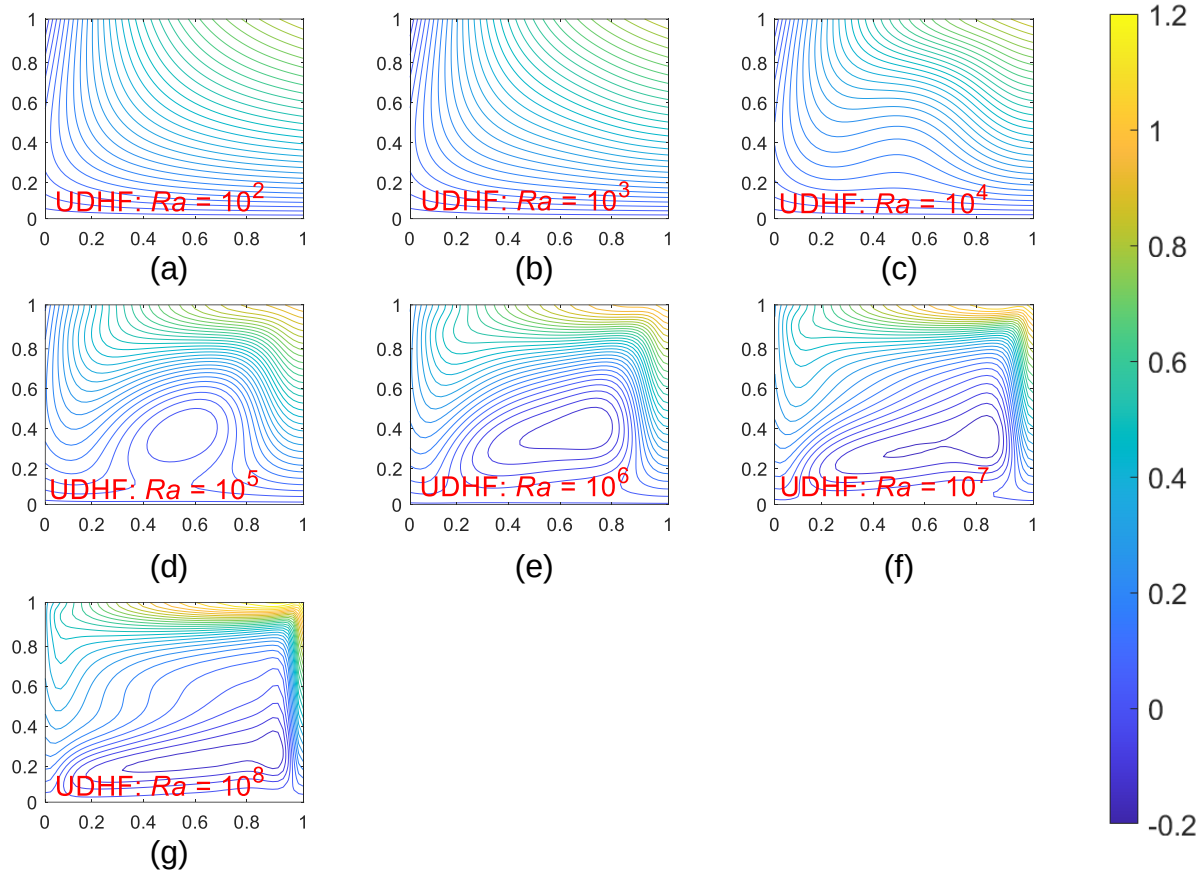

Fig. 4.16: Effect of Rayleigh number on heatlines ($Pr = 10$, $E = 2$, $Bi^* = 3$, $AR = 1$): (a). $Ra = 10^2$, $H_{max} = 0.835$ (b). $Ra = 10^3$, $\theta_{max} = 0.1753$ (c). $Ra = 10^4$, $H_{max} = 0.862$ (d). $Ra = 10^5$, $H_{max} = 0.967$ (e). $Ra = 10^6$, $H_{max} = 1.06$ (f) $Ra = 10^7$, $H_{max} = 1.14$ (g). $Ra = 10^8$, $H_{max} = 1.2$.

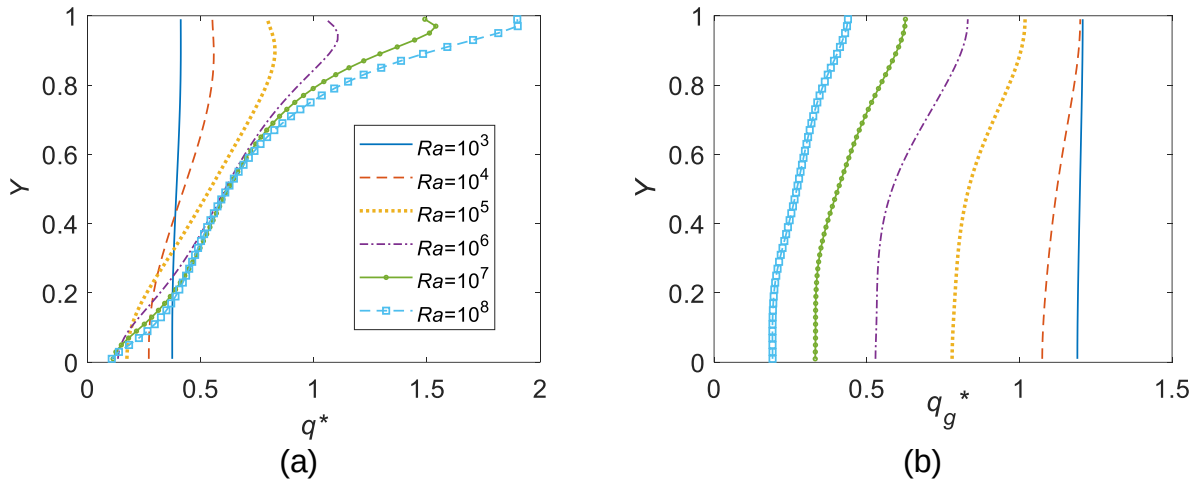

Fig. 4.17: Effect of Rayleigh number on (a). local convective heat flux at isothermal wall and (b) flux lost through glass wall (Pr = 10, E = 2, Bi^* = 3, AR = *1*).

(c) Effect of Prandtl Number

This section looks at how gradually varying Prandtl number affects temperature and flow distribution and the local convective heat flux at the isothermal wall of the cavity. Numerical analysis was carried out for increasing order of magnitude of Pr (=0.01, 0.1, 1, 10, 100 and 1000). This wide range of Prandtl numbers includes liquid metals and semiconductors (at the lower end) to viscous oils (at the high end). While it may be argued that liquid metals are opaque and are not relevant to a study pertaining to volumetric heating, there are semi-conducting fluids that have low Prandtl numbers, and they are semi-transparent to thermal radiation (Rapp, Bastian E., 2017). Streamlines (Fig. 4.18), isotherms (Fig. 4.19) and heatlines (Fig. 4.20) are plotted to show the effect of varying Prandtl number. Fig. 4.21 shows the effect of Prandtl number variation on the convective heat flux and at the isothermal wall and the flux at the glass wall.

There is a gradual transition observed in the flow and temperature contours as Pr increases. While conduction dominates at low Prandtl numbers, convection is the dominant heat transfer mechanism at higher Prandtl numbers. However, there is insignificant change in the contours beyond Pr=10. All the other values are kept constant i.e., $Ra = 10^6$ and E = 2, Bi^* = 3, AR = *1*.

Effect on streamlines

The value of maximum stream function Ψ_{max} increases as *Pr* increases. The values of Ψ_{max} are 9.99, 10.28, 11.7, 12.28, 12.32 and 12.33 for *Pr*=0.01, 0.1, 1, 10, 100 and 1000, respectively. As it can be seen there is negligible variation of Ψ_{max} as *Pr* becomes greater than 10. This becomes clear from the plot of streamlines (Fig. 10) which remain unchanged as *Pr* increases above 10. At low *Pr* values (=0.01), conduction dominates whereas convection takes precedence at high *Pr* values. This is because at low Prandtl number, the thermal conductivity of the medium is very high and the heat transfer rate dominated by conduction. Also, a weak eddy is formed at *Pr* = 0.01, however, its effect on the heat transfer rate is very small compared to heat transfer by conduction.

Effect on isotherms

As can be inferred from Fig. 4.19, the isotherms become horizontal progressively as *Pr* increases. The maximum dimensionless temperature (θ_{max}) in the cavity decreases as the *Pr* values increase. This is because of convection induced mixing of the fluid in the cavity. The thermal boundary layer becomes thinner as Prandtl number increases. There is little to no difference in the isotherms beyond *Pr* values equal to 10. Above this value of Prandtl number, the viscous forces reach a point where there is no further change in the temperature and flow distribution in the cavity.

Effect on heatlines

Fig. 4.20 shows the effect of progressively increasing Prandtl number on the heatlines. The pattern of heatlines is like that of streamlines. Also, there is negligible change in the pattern of heatlines beyond *Pr* = 10.

Effect on local convective heat flux at isothermal wall and the heat lost at glass wall

The local convective heat flux variation with *Y* at the isothermal wall increases with the height of the cavity due to the higher temperature of the fluid (Fig. 4.21). There is negligible variation in the curves for $Pr \geq 10$. The net local convective flux at isothermal wall increases with Prandtl number. The same trend of higher temperature at the upper region is seen with the flux at the glass wall. Also, the net heat loss at glass wall decreases as Prandtl number increases. Also, there is negligible variation in flux when $Pr \geq 10$. Thus, an increase in Prandtl number facilitates the increase of useful heat gain at isothermal wall and decreases the heat loss at glass wall as was observed for the case of Rayleigh number.

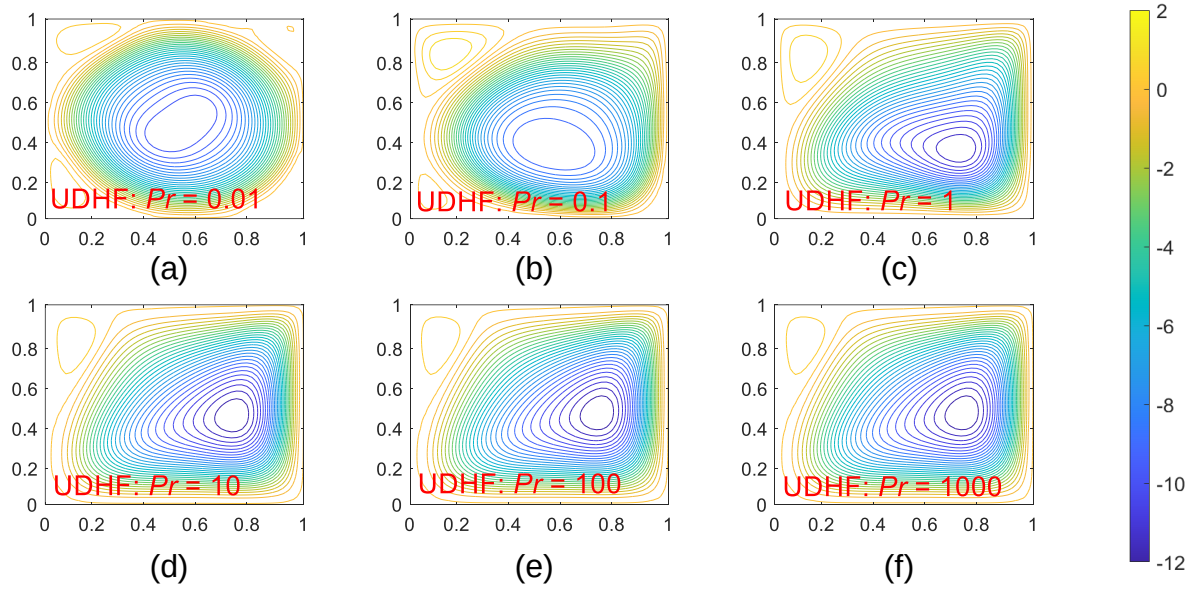

Fig. 4.18: Effect of Prandtl number on flow structure (streamlines) ($Ra = 10^6$, $E = 2$, $Bi^* = 3$, $AR = 1$): (a). $Pr = 0.01$, $|\Psi_{max}| = 9.99$ (b). $Pr = 0.1$, $|\Psi_{max}| = 10.28$ (c). $Pr = 1$, $|\Psi_{max}| = 11.7$ (d). $Pr = 10$, $|\Psi_{max}| = 12.28$ (e). $Pr = 100$, $|\Psi_{max}| = 12.32$ (f). $Pr = 1000$, $|\Psi_{max}| = 12.33$.

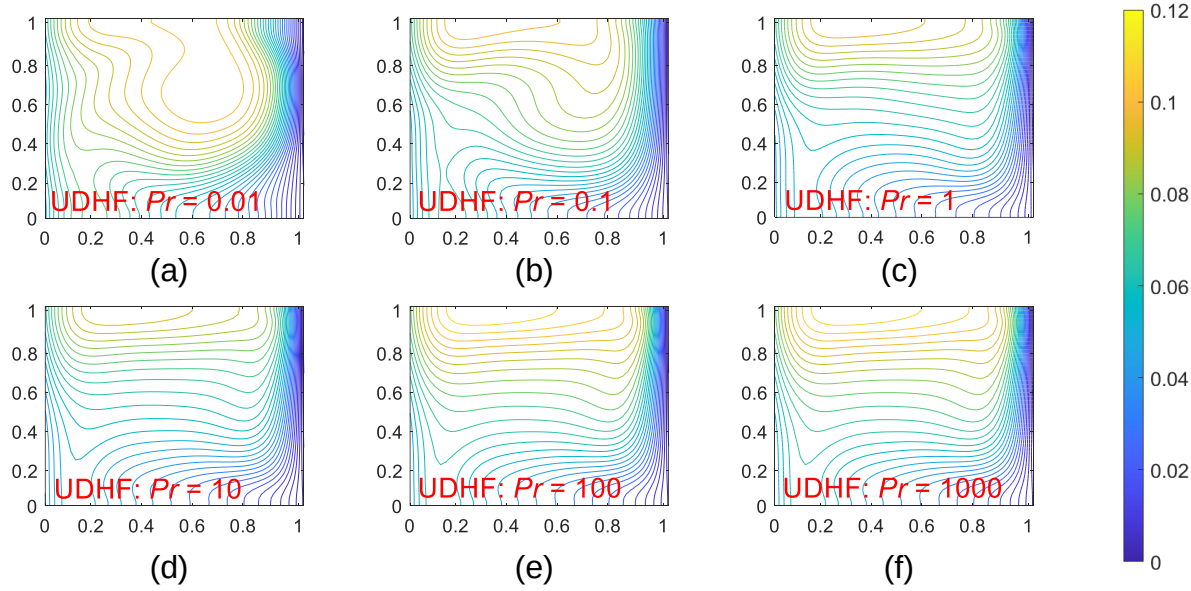

Fig. 4.19: Effect of Prandtl number on temp. distribution (isotherms) ($Ra = 10^6$, $E = 2$, $Bi^* = 3$, $AR = 1$): (a). $Pr = 0.01$, $T_{max} = 0.1024$ (b). $Pr = 0.1$, $T_{max} = 0.1011$ (c). $Pr = 1$, $T_{max} = 0.099$ (d). $Pr = 10$, $T_{max} = 0.095$ (e). $Pr = 100$, $T_{max} = 0.0946$ (f). $Pr = 1000$, $T_{max} = 0.0946$.

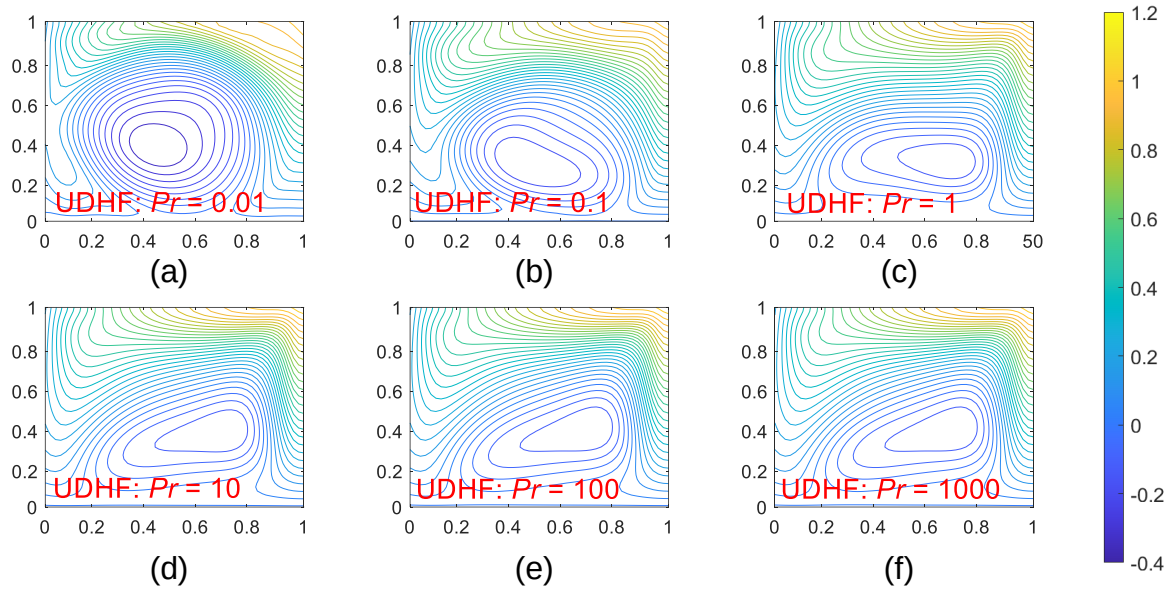

Fig. 4.20: Effect of Prandtl number on heatlines ($Ra = 10^6$, $E = 2$, $Bi^* = 3$, $AR = 1$): (a). $Pr = 0.01$, $H_{max} = 1.022$ (b). $Pr = 0.1$, $H_{max} = 1.033$ (c). $Pr = 1$, $H_{max} = 1.055$ (d). $Pr = 10$, $H_{max} = 1.060$ (e). $Pr = 100$, $H_{max} = 1.0\,61$ (f). $Pr = 1000$, $H_{max} = 1.06$.

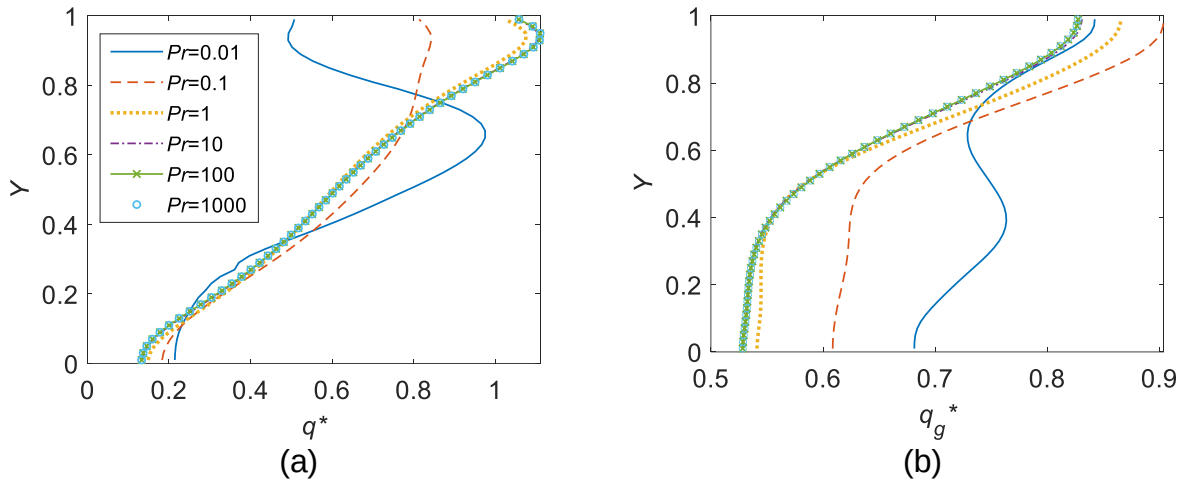

Fig. 4.21: Effect of Prandtl number on (a). local convective heat flux at isothermal wall and (b). flux lost through glass wall ($Ra = 10^6$, $E = 2$, $Bi^* = 3$, $AR = 1$).

(d) Effect of Aspect Ratio

This section observes the effect of aspect ratio in a cavity affects the temperature and heat and fluid flow distribution inside the cavity. Numerical analysis was carried out for aspect ratios varying from 0.1 (very low) to 10 (very high). Streamlines (Fig. 4.22), isotherms (Fig. 4.23) and heatlines (Fig. 4.24) are plotted to show the effect.

Effect on streamlines

Fig. 4.22 shows the effect of aspect ratio on the streamlines. At low aspect ratio (AR=0.1), the flow structure is divided into two whorls. This happens as the fluid rises along the transparent wall (left) which allows the incident radiation to pass through, and then moves towards the right along the top adiabatic wall. However, it loses momentum as the horizontal distance is much larger and falls midway – creating two distinct whorls. As the aspect ratio increases however, a single loop is observed which becomes more and more elongated ("stretched") as aspect ratio increases. The values of stream functions in ascending order of aspect ratios are 0.11, 5.97, 12.28, 19.42 and 59.02.

Effect on isotherms

Fig. 4.23 shows the effect of varying aspect ratio on the isotherms. At low aspect ratios, the isotherms are almost vertical as would be the case if heating was taking place through conduction alone. While the central core is more stagnant in cavities with lower aspect ratios, for higher aspect ratios the core is not stagnant as is evident from the non-horizontal temperature profiles. The values of dimensionless temperatures in ascending order of aspect ratio are 0.161, 0.088, 0.095, 0.105 and 0.140. It is interesting to note the trend here. While it is expected that the value of maximum temperature should increase as the aspect ratio increases because as the vertical height of cavity increases while the width of the cavity remains same – the heated area also increases. However, the value of maximum temperature is highest when the AR = 0.1. This is because there is very little mixing due to convection as the fluid movement is restricted by the horizontal cavity walls and as such the temperature increases. As aspect ratio increases however, the heat flux increases but so does the convective motion of the fluid and mixing between fluid layers. Thus, the value of maximum temperature first decreases at AR = 0.5 beyond which it continues to increase at higher aspect ratios.

Effect on heatlines

Fig. 4.24 shows the effect of varying aspect ratios on heatlines. For low aspect ratios, the heatlines are horizontal, perpendicular to the almost vertical isotherms. At higher aspect ratios, the heatlines are once again like the streamlines, showing that convection is the predominant mechanism of heat transport. The values of heat function for the different aspect ratios in ascending order are 0.124, 0.586, 1.024, 1.607 and 6.39.

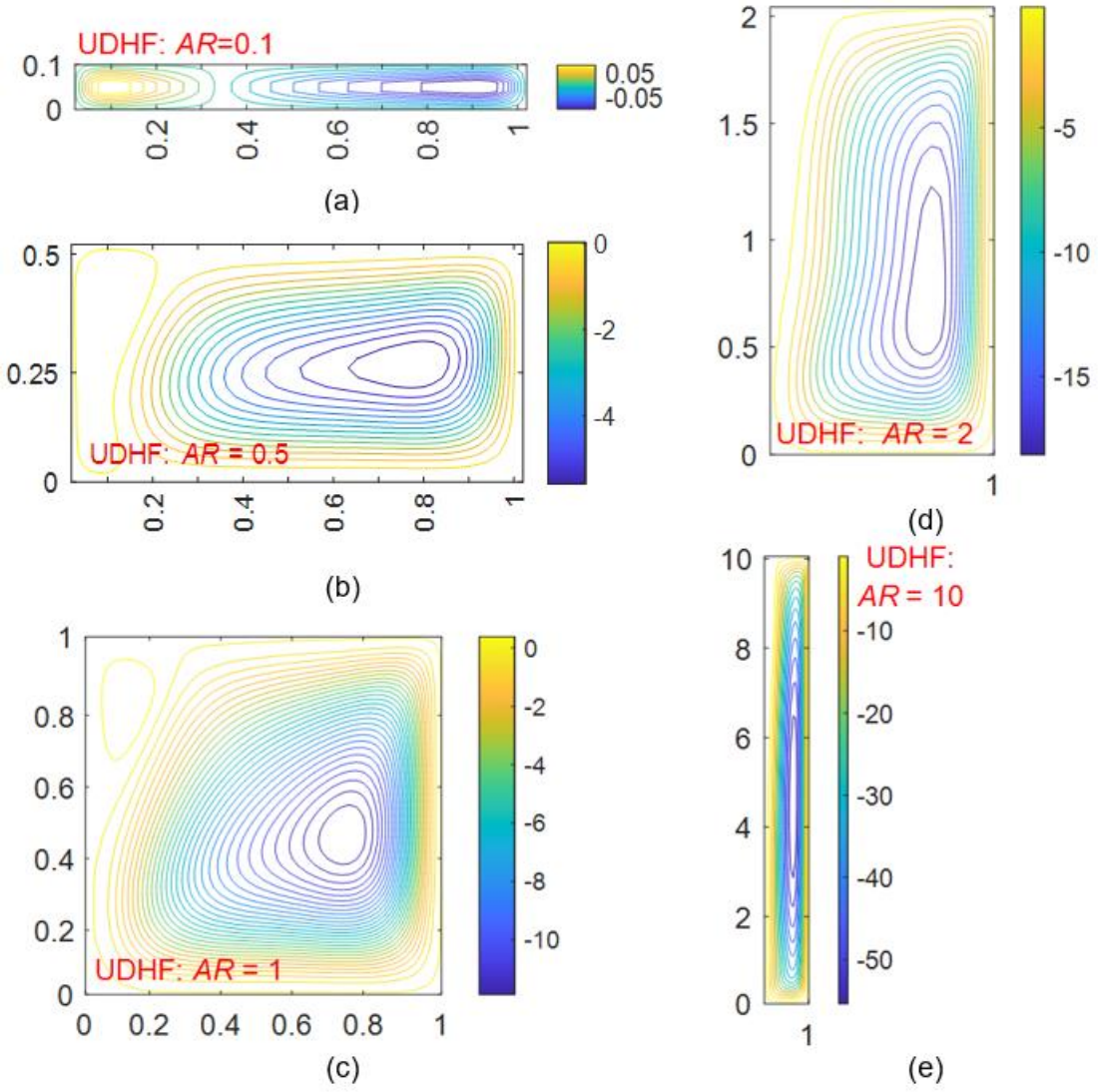

Fig. 4.22: Effect of aspect ratio on flow structure (streamlines) ($Ra = 10^6$, $Pr = 10$, $E = 2$, $Bi^* = 3$): (a). $AR = 0.1$, $|\Psi_{max}| = 0.111$ (b). $AR = 0.5$, $|\Psi_{max}| = 5.974$ (c). $AR = 1$, $|\Psi_{max}| = 11.7$ (d). $AR = 2$, $|\Psi_{max}| = 19.42$ (e). $AR = 10$, $|\Psi_{max}| = 59.02$.

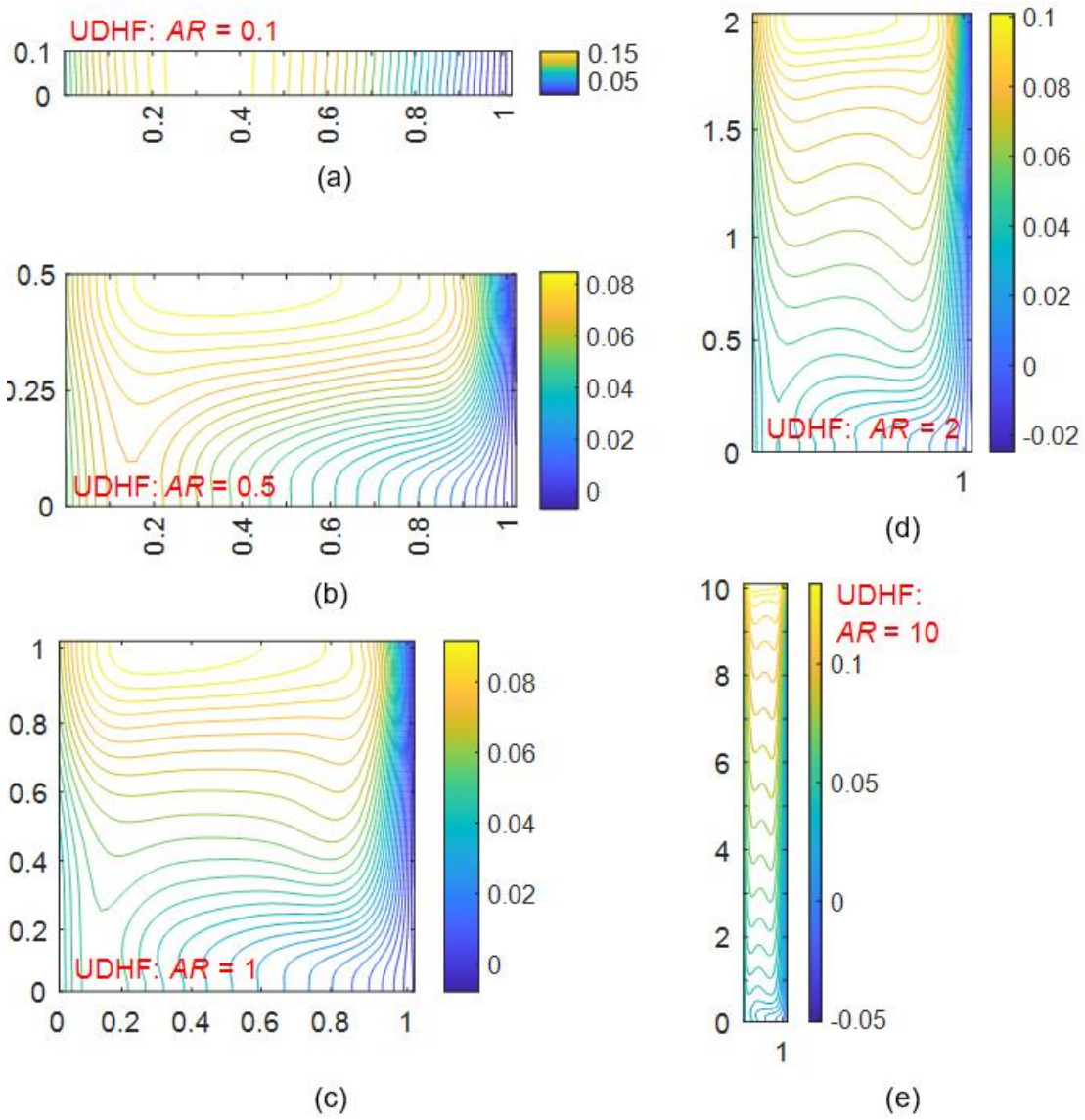

Fig. 4.23: Effect of aspect ratio on temperature distribution (isotherms) ($Ra = 10^6$, $Pr = 10$, $E = 2$, $Bi^* = 3$): (a). $AR = 0.1$, $T_{max} = 0.16$ (b). $AR = 0.5$, $T_{max} = 0.088$ (c). $AR = 1$, $T_{max} = 0.095$ (d). $AR = 2$, $T_{max} = 0.1053$ (e). $AR = 10$, $T_{max} = 0.14$.

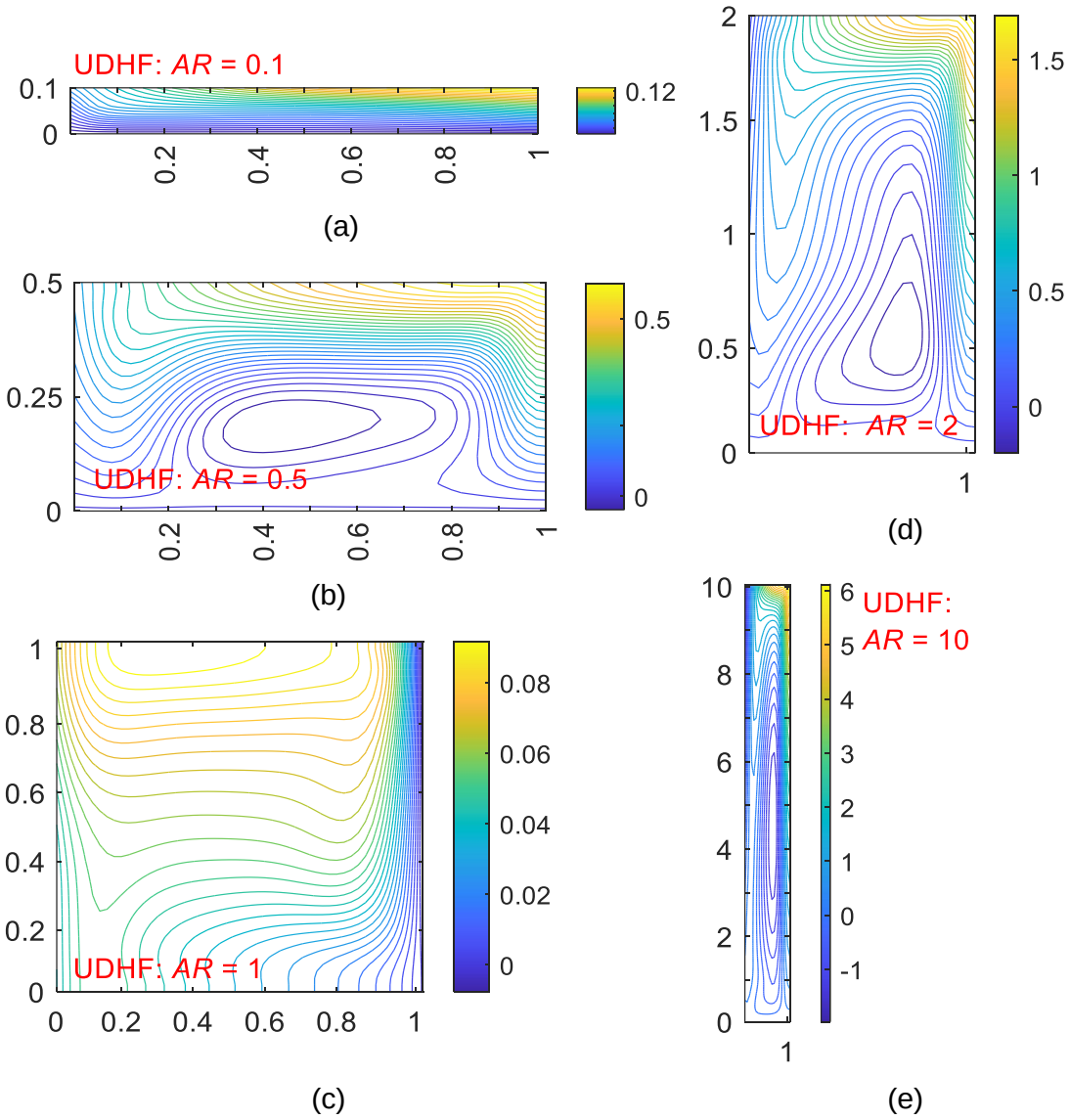

Fig. 4.24: Effect of aspect ratio on heatlines ($Ra = 10^6$, $Pr = 10$, $E = 2$, $Bi^* = 3$): (a). $AR = 0.1$, $H_{max} = 0.124$ (b). $AR = 0.5$, $H_{max} = 0.586$ (c). $AR = 1$, $H_{max} = 1.055$ (d). $AR = 2$, $H_{max} = 1.60$ (e). $AR = 10$, $H_{max} = 6.39$.

(e). Effect of modified Biot number

It is interesting to note the isotherms (Fig. 4.25) obtained from plotting the results gathered from varying the modified Biot number in the numerical simulation. When $Bi^* = 0$, which implies that no heat loss takes place from the transmitting glass wall by radiation or convection, the temperature of the transmitting glass wall is higher than the liquid layer immediately on the right of it. However as Bi^* is increased, the temperature of the glass wall begins to decrease as it loses more and more heat through convection and radiation. This phenomenon of temperature inversion is useful in preventing heat losses from volumetric absorption based solar receivers and provides an advantage over surface absorption-based receivers which have the highest temperature at the heated surface.

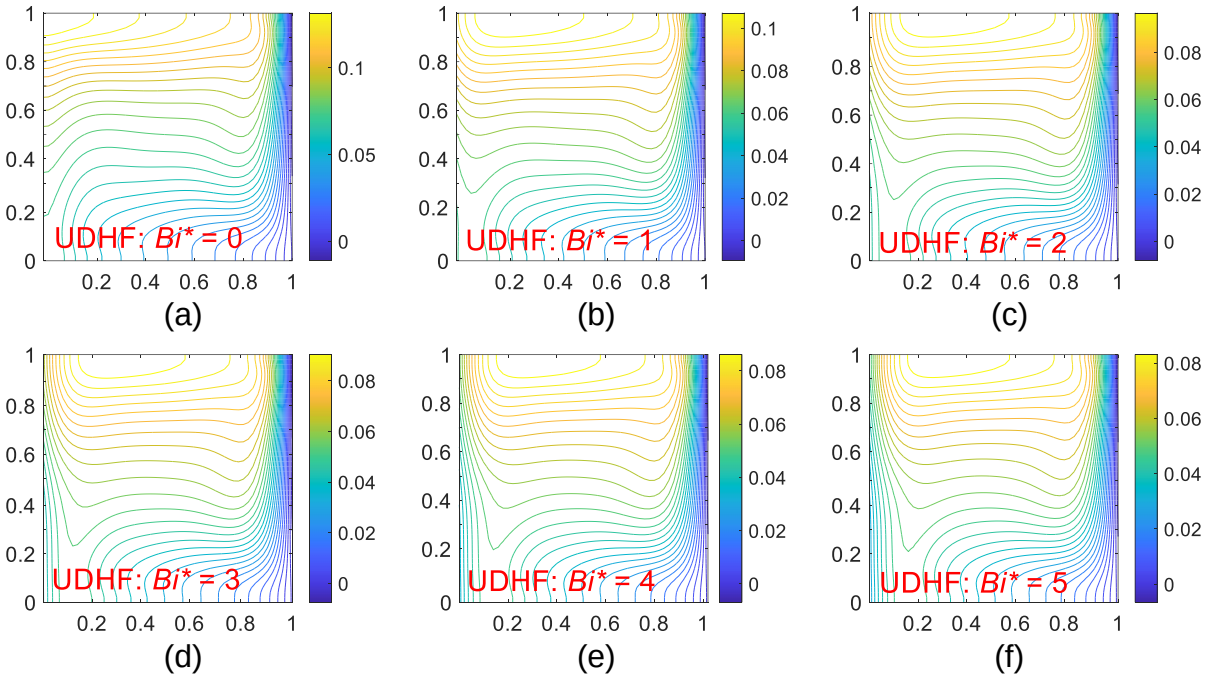

Fig. 4.25: Effect of modified Biot number on temperature distribution (isotherms) ($Ra = 10^6$, $Pr = 10$, $E = 2$, $AR = 1$): (a). $Bi^* = 0$, $T_{max} = 0.14$ (b). $Bi^* = 1$, $T_{max} = 0.12$ (c). $Bi^* = 2$, $T_{max} = 0.1$ (d). $Bi^* = 3$, $T_{max} = 0.09$ (e). $Bi^* = 4$, $T_{max} = 0.085$ (f). $Bi^* = 5$, $T_{max} = 0.081$

(f). Impact of Rayleigh number, Prandtl number and optical thickness on the useful heat gain at the isothermal wall (X = 1).

Fig. 4.26 shows the cumulative heat flux for the different Rayleigh and Prandtl numbers and the optical thickness of the fluid. The useful cumulative flux increases with Rayleigh and the Prandtl number. The cumulative flux at isothermal wall (Q^*) is calculated as follows:

$$Q^* = \int_{Y=0}^{Y=1} \frac{\partial T^*}{\partial X} dY \tag{4.18}$$

It also increases with fluid opacity up to $E = 2$. However, on comparing the values for $E = 2$ and $E = 4$ at low Rayleigh numbers, the value of flux is higher for $E = 2$. This is because at low Rayleigh numbers and higher optical thickness values, the convective motion of the liquid is not strong, and the effect of radiation is stronger at the transmitting wall than at the isothermal wall. However, this is not the case at higher Rayleigh numbers where cumulative flux values for $E = 4$ are higher than those at $E = 2$.

Fig. 4.27 shows the variation of cumulative flux with Rayleigh number for different optical thickness values (E ranges from 0.1 to 100). Cumulative flux is calculated as the sum of the flux values at different points along the height of the cavity. The Prandtl number is kept constant ($Pr = 10$). As optical thickness increases from $E = 1$ to $E = 2$, the cumulative flux at isothermal wall is consistently high across all Rayleigh numbers from 10^3 to 10^8. Beyond $E = 2$, i.e., for $E = 4$, 10 and 100, the cumulative flux drops at low Rayleigh numbers.

Another important observation is the existence of regimes – a conduction dominated regime ($Ra \leq 10^3$) where the heat flux at the isothermal wall is minimum; a transition regime ($10^3 \leq Ra \leq 10^4$) where the heat flux increases gently; a convection regime ($10^4 < Ra \leq 10^8$) where there is a sharp increase in the value of the cumulative heat flux (Q^*).

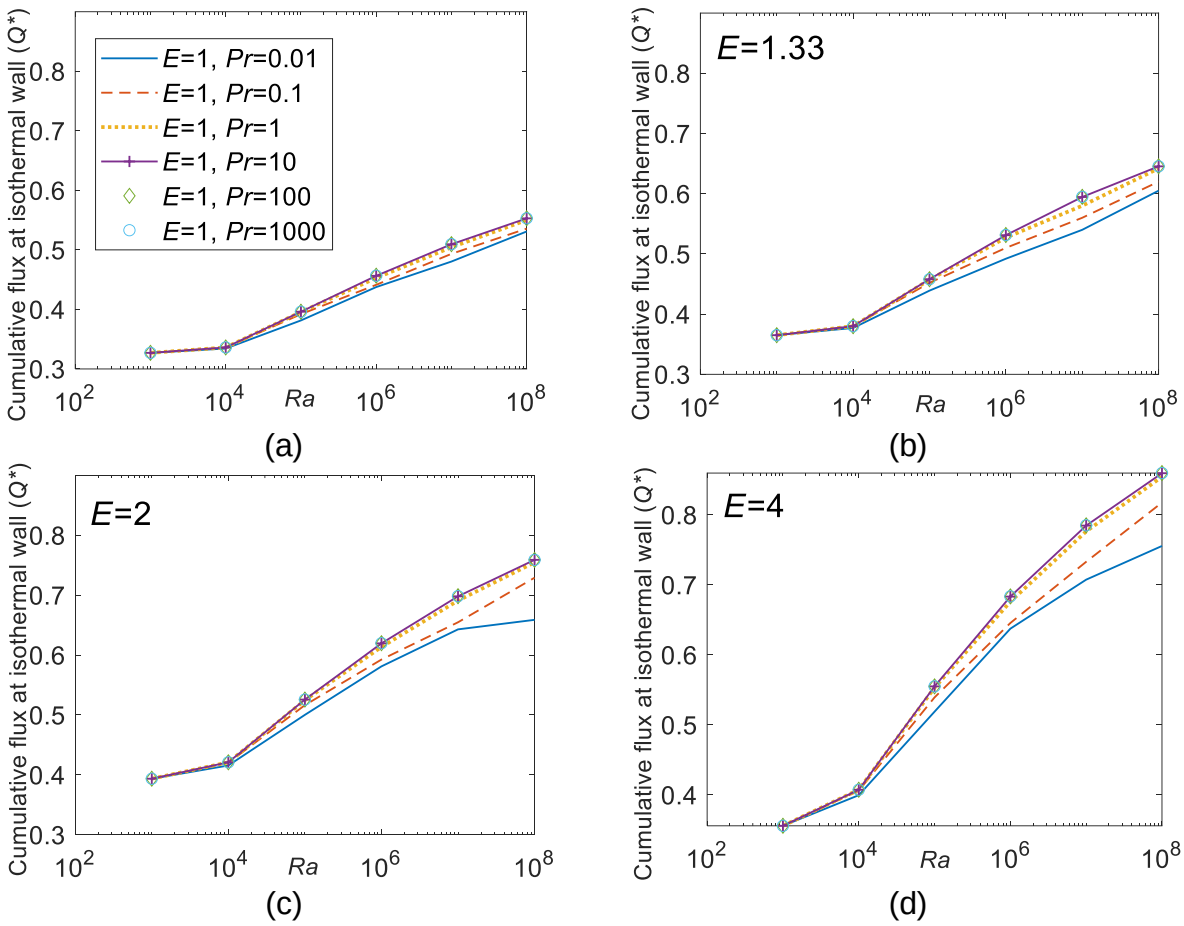

Fig. 4.26: Impact of Rayleigh number, Prandtl number and optical thickness of fluid on the cumulative heat flux at the isothermal wall (a). $E = 1$ (b). $E = 1.33$ (c). $E = 2$ and (d). $E = 4$.

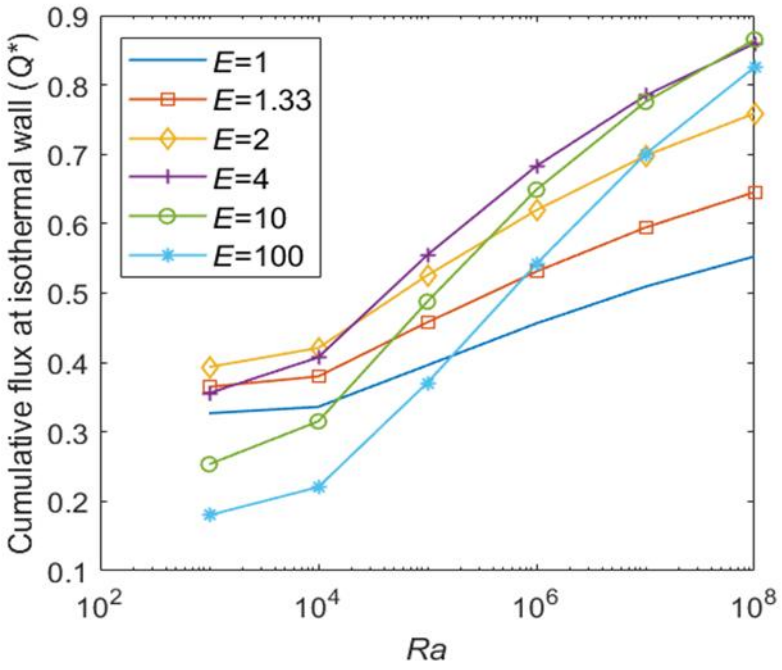

Fig. 4.27: *Ra* vs cumulative flux (Q^*) for different fluid opacity values (*Pr* = 10).

4.3.3.2 Linearly varying heat flux

In this section, the effect of linearly varying heat flux is presented and discussed. Two orientations of linearly varying heat flux are considered in this study which are as follows:

Case 1: Flux varies from zero to maximum from the bottom to the top of the cavity (LVHF1).

Case 2: Flux varies from maximum to zero from the bottom to the top of the cavity (LVHF2).

The net heat flux entering the cavity in both the cases is same as that entering in the cavity with uniformly distributed heat flux.

In the present section, the effect of linearly varying heat flux on the temperature and heat and flow distribution in the cavity are studied through streamlines, isotherms and heatlines.

Fig. 4.28 shows the streamlines, isotherms and heatlines for case 1 where the flux varies from zero to maximum from the bottom to the top of the cavity. The Rayleigh number is kept constant at 10^6, and the optical thickness is varied (*E* = 1, 2 and 10). The values of $|\Psi_{max}|$ for the different optical thicknesses are 7.97, 9.94, 12.6245. Similarly, the values of θ_{max} are 0.0782, 0.0997 and 0.126 and the values of H_{max} are 1.0504, 0.9815 and 0.7331 for *E* = 1, 2 and 10, respectively.

Fig. 4.29 shows the streamlines, isotherms and heatlines for case 2 where the flux varies from maximum to zero from the bottom to the top of the cavity. The Rayleigh number is kept constant at 10^6, and the optical thickness is varied (E = 1, 2 and 10). The values of $|\Psi_{max}|$ for the different optical thicknesses are 12.511, 13.45, 12.3. Similarly, the values of θ_{max} are 0.055, 0.07 and 0.095 and the values of H_{max} are 1.04, 0.975 and 0.74 for E = 1,2 and 10, respectively.

On comparing the results obtained for linearly varying heat flux to those of uniformly distributed heat flux, it was found that for case 1 where the flux is zero at the bottom and increases linearly to the top there is very little difference in the pattern of isotherms, however a slightly higher value of maximum cavity temperature is obtained. The value of maximum stream function is lower than that for uniform heat flux and the value of maximum heat function is higher. This can be explained easily – as the bulk of the radiation is incident on the upper half of the cavity, more energy gets concentrated thus increasing the temperature and heat flow in the upper region. However, the flow of fluid is decreased as the heated layer of fluid is already on the top, thus natural convection decreases.

Similarly, on comparing the results obtained for linearly varying heat flux to those of uniformly distributed heat flux (UDHF), it is found that for case 2 where the flux is maximum at the bottom and decreases to zero at the top, the difference is more conspicuous. The isotherms are closer to each other at the bottom and further apart at the top indicating a steeper temperature gradient at the bottom due to greater radiation incident at the bottom and the maximum cavity temperature is lower than for that of uniformly distributed flux. The value of maximum stream function is higher than that for uniform heat flux and the value of maximum heat function is lower. The higher stream function values can be attributed to greater flux being incident in the lower half of the cavity causing the fluid at the bottom to become heated sooner due to which its density decreases, and it moves upwards more rapidly. Similarly, the heat function value, which is highest at the top of the cavity, is comparatively lower in this case as there is lower heat flux incident at the top.

One interesting observation is the difference in the maximum and minimum cavity temperatures for the three cases. The difference in the maximum and minimum cavity temperatures is highest for LVHF1 followed by the case of UDHF and the difference is lowest for LVHF2. Thus, the LVHF2 configuration provides the most uniform temperature distribution which can be used in the development of receivers which are less prone to stresses caused due to temperature variation.

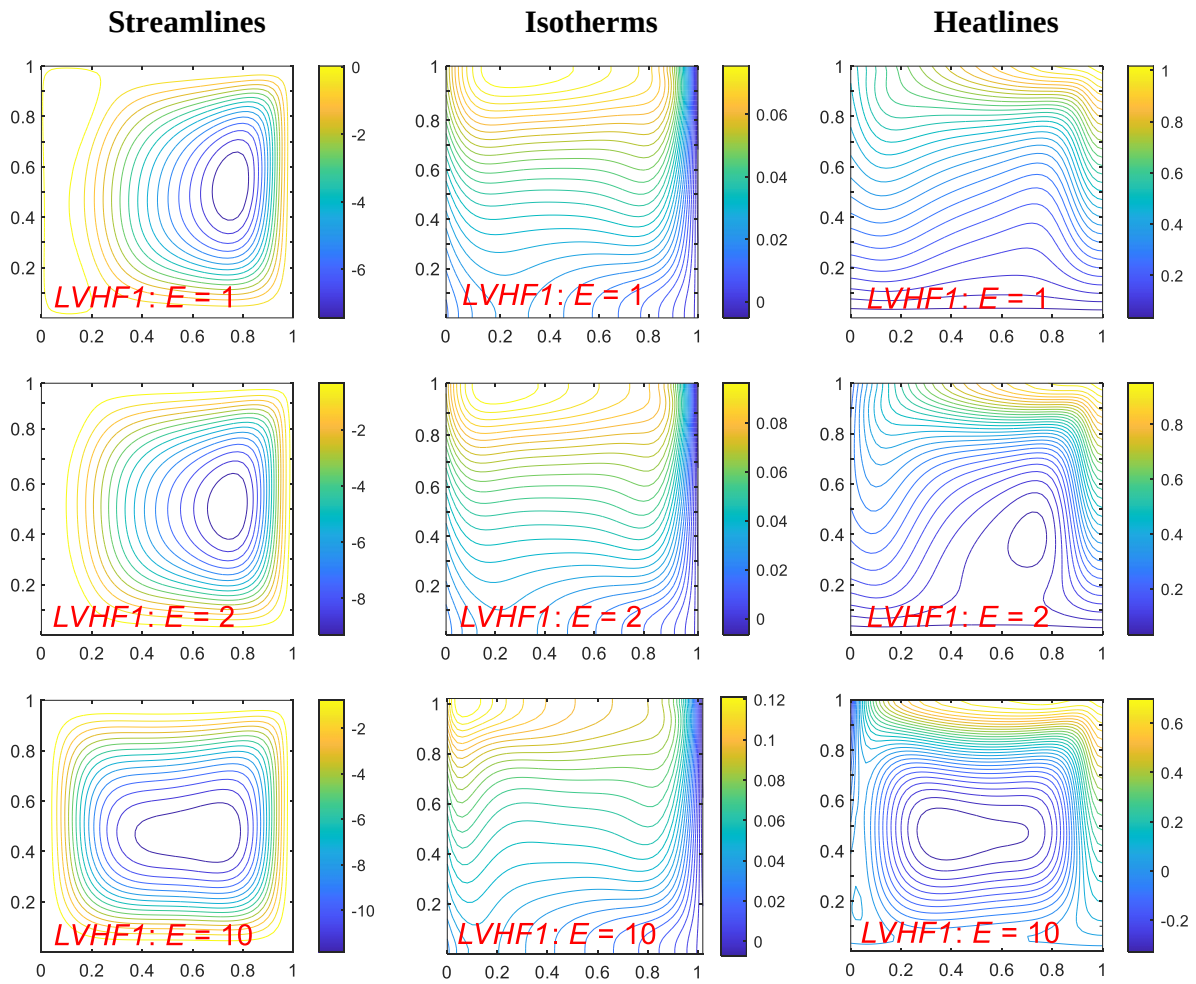

Fig. 4.28: Streamlines, Isotherms and Heatlines for linearly varying heat flux: case 1 (maximum flux at the bottom and zero at top) for different optical thicknesses ($Ra = 10^6$, $Pr = 10$, $Bi^* = 3$, $AR = 1$).

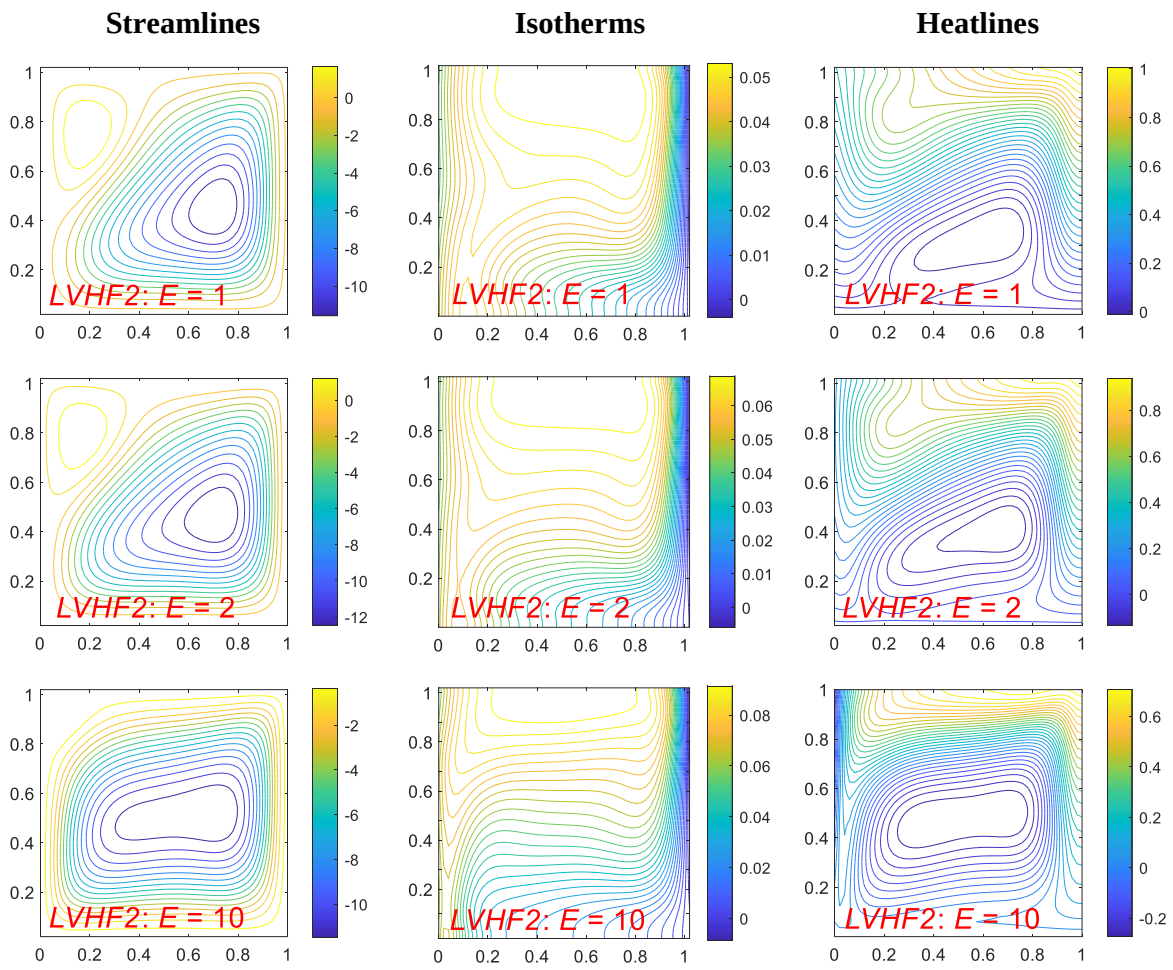

Fig. 4.29: Streamlines, Isotherms and Heatlines for linearly varying heat flux: case 2 (zero flux at the bottom and maximum at top) for different optical thicknesses ($Ra = 10^6$, $Pr = 10$, $Bi^* = 3$, $AR = 1$).

4.3.4 Cavity heated volumetrically from bottom: Results

The results of the study on cavity heated from bottom have been divided into two sections. Section 4.3.3.1 deals with the results from heating the cavity with uniformly distributed flux whereas section 4.3.3.2 deals with linearly varying heat flux. While the total flux remains the same in both cases, in the case of linearly varying flux, it varies from zero to maximum from the left to the right of the cavity.

4.3.4.1 Uniformly distributed heat flux

This section looks at the effect of uniformly distributed heat flux (UDHF) on the temperature and flow distribution in a bottom-heated cavity and how it depends upon the Rayleigh and Prandtl numbers, the optical thickness of the fluid, the convective flux at the transmitting wall, the aspect ratio of the cavity etc. The Rayleigh number is varied from 10^2 to 10^5, i.e., the laminar regime. The Prandtl number is varied from 0.01 to 1000. The values of optical thickness are taken as 0.1, 1, 1.33, 2, 4, 10 and 100. The convective heat loss from glass wall is regulated by varying the value of Bi^* from 0 to 5. The value of aspect ratio is varied from 0.1 to 1.

(a). Effect of optical thickness of fluid layer

This section looks at how optical thickness of the fluid layer affects the isotherms, streamlines, heatlines and the heat flux at the isothermal wall. Numerical analysis was carried out for different values of E (=0.1, 1, 1.33, 2, 4, 10 and 100). The values of other parameters were fixed (AR=1, Bi^*=3, Ra=10^5, Pr=10). Figures 4.30, 4.31, 4.32 and 4.33 show the results.

Effect on streamlines

As the optical thickness increases from 0.1 to 100, the value of maximum stream function increases to 10.0918 at E=10 after which it decreases to 8.8949 at E=100. As the optical thickness increases, more energy is deposited in liquid layers which generates a convective motion of the fluid as a larger proportion of the incident energy is absorbed by the liquid as opposed to being directly absorbed by the isothermal wall at the top of the cavity. At very low values of optical thickness (E=0.1), there is a symmetric structure of streamlines with two whorls appearing on the left and right of the cavity. The value of the stream function appears to be very small (order of 10^{-14})

indicating very little movement of the fluid. At higher values of optical thickness, a single whorl is observed in the pattern of the streamlines with much higher values of stream function (Fig. 4.30).

Effect on isotherms

At the lowest value of optical thickness (E=0.1) investigated in the study, the isotherms are horizontal, and the maximum temperature appears in the middle of the cavity. The pattern changes with isotherms becoming more curved as the optical thickness increases showing convective motion and the shape of the pattern does not change drastically, however, the maximum temperature in the cavity moves closer to the transmitting wall at the bottom of the cavity, as E is increased which is obvious as more and more energy is accumulated in the region closer to the transmitting wall. The maximum temperature in the cavity also continues to increase as the optical thickness increases from 0.0167 (at E=0.1) to 0.1567 (at E=100) (Fig. 4.31).

Effect on heatlines

At very low value of optical thickness (E=0.1), the heatlines appear as vertical, perpendicular to the isotherms, as most of the incident radiation passes unabsorbed through the cavity from the bottom wall towards the top. This is not explicitly evident from the streamlines and the isotherms and shows how heatlines help in providing a clearer picture which forms the basis for understanding the thermal mechanism. As optical thickness continues to increase (from E=1 to E=100), the pattern of heatlines begins to curve and a whorl is formed more towards the right side of the cavity while on the left the heatlines still are almost vertical with a slight dent in the middle. The pattern does not change in appearance even as optical thickness is varied from (E=1 to E=100) (Fig. 4.32).

Effect on local heat flux at top isothermal wall

Convective heat flux at the top isothermal wall and the transmitting glass wall has been calculated and plotted. The following equation gives the convective heat flux at different values of cavity height.

$$q^*(X) = -\frac{\partial T^*}{\partial Y_{(Y=1)}} \tag{4.19}$$

As the fluid opacity increases, the convective heat flux at the isothermal wall also increases up to a point. The maximum convective heat flux is observed at *E=4.* At *E=10*, the convective heat flux is lower at all values of *X* (Fig. 4.33).

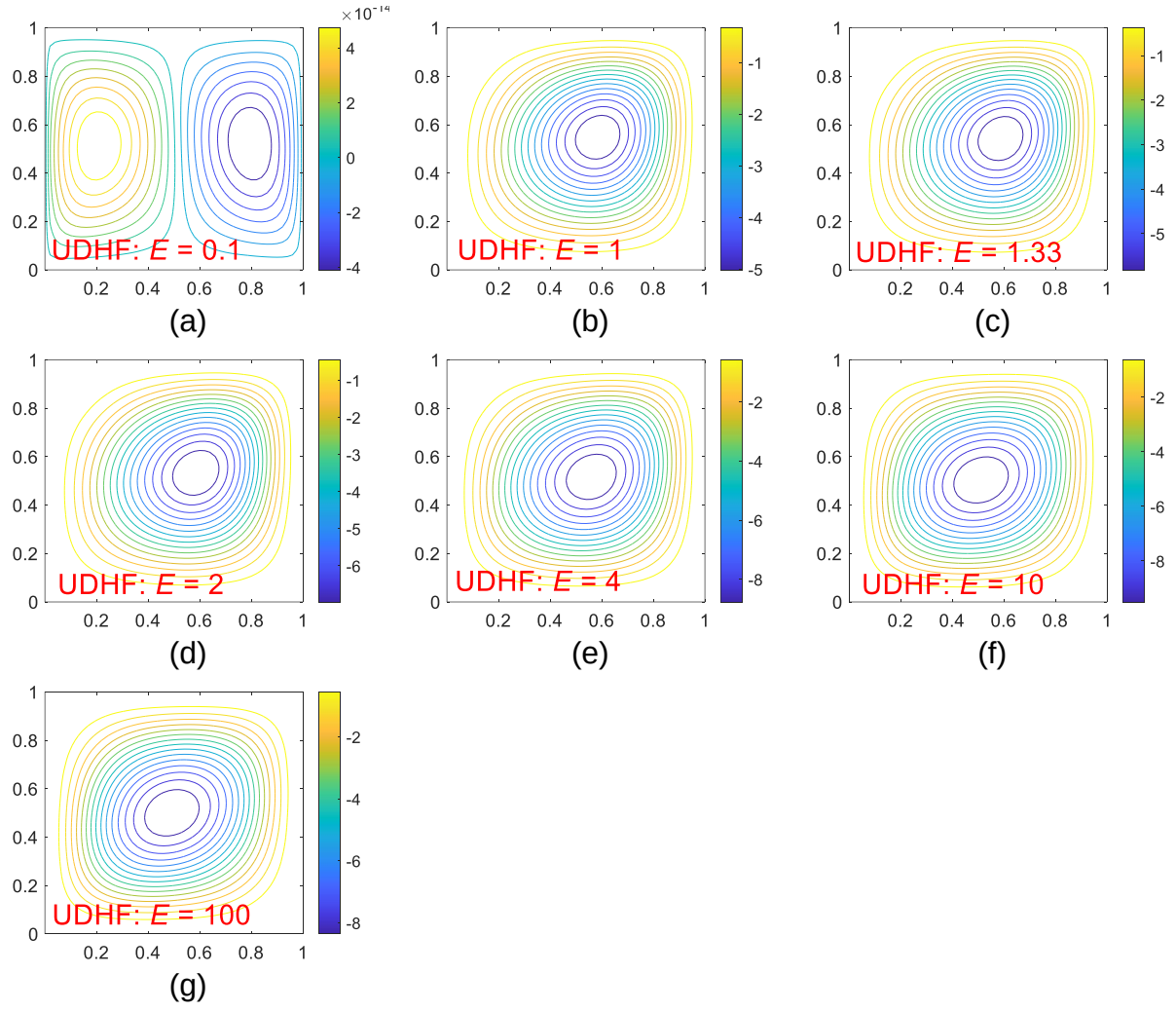

Fig. 4.30: Effect of optical thickness on flow structure (streamlines) ($Ra = 10^5$, $Pr = 10$, $Bi^* = 3$, $AR = 1$): (a). $E = 0.1$, $|\Psi_{max}| = 5.35\times10^{-14}$ (b). $E = 1$, $|\Psi_{max}| = 5.35$ (c). $E = 1.33$, $|\Psi_{max}| = 6.2020$ (d). $E = 2$, $|\Psi_{max}| = 7.4311$ (e). $E = 4$, $|\Psi_{max}| = 9.3364$ (f). $E = 10$, $|\Psi_{max}| = 10.0918$ (g). $E = 100$, $|\Psi_{max}| = 8.8949$.

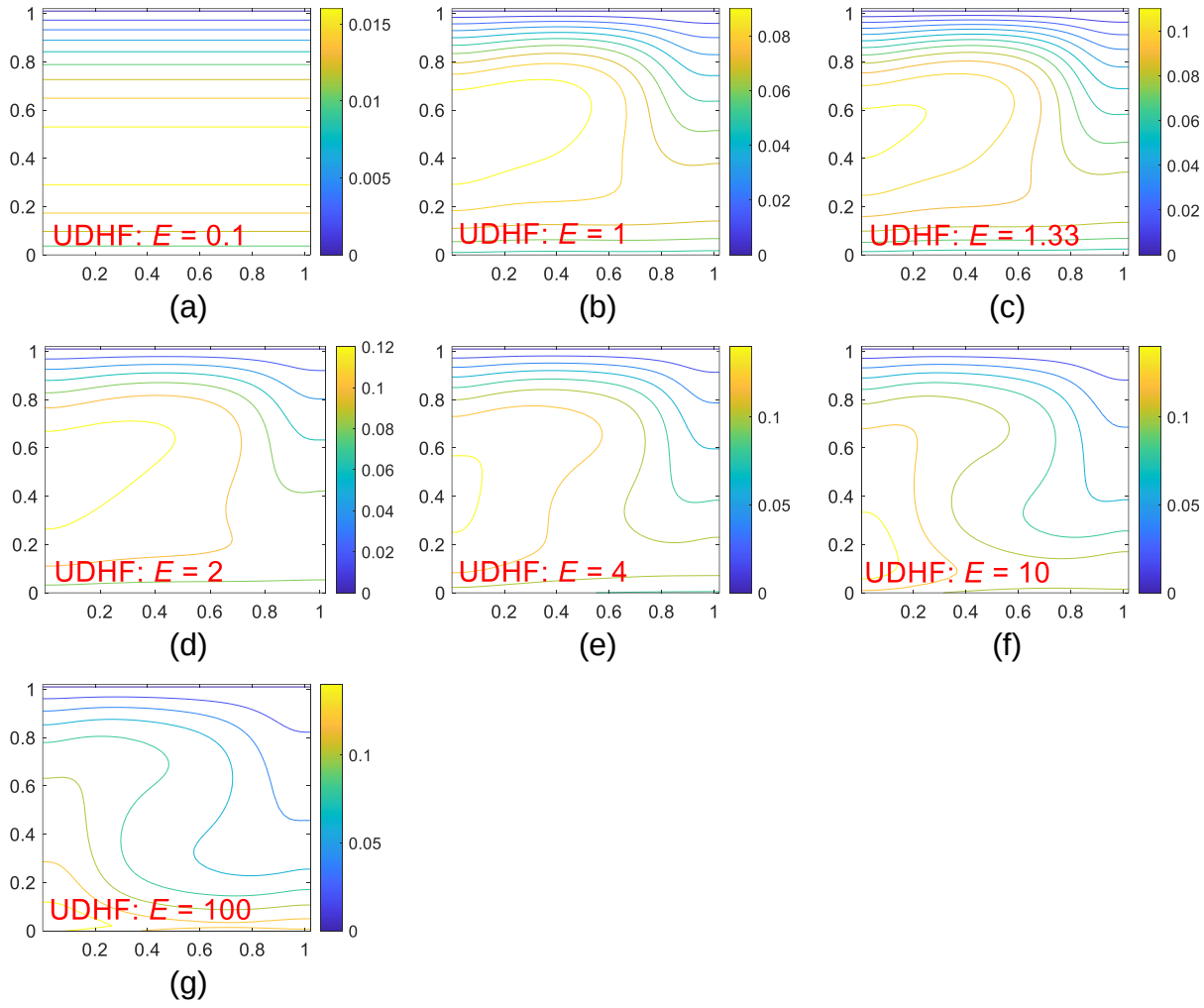

Fig. 4.31: Effect of optical thickness on temp. distribution (isotherms) ($Ra = 10^5$, $Pr = 10$, $Bi^* = 3$, $AR = 1$): (a). $E = 0.1$, $T_{max} = 0.02$ (b). $E = 1$, $T_{max} = 0.09$ (c). $E = 1.33$, $T_{max} = 0.08$ (d). $E = 2$, $T_{max} = 0.13$ (e). $E = 4$, $T_{max} = 0.14$ (f). $E = 10$, $T_{max} = 0.15$ (g). $E = 100$, $T_{max} = 0.16$.

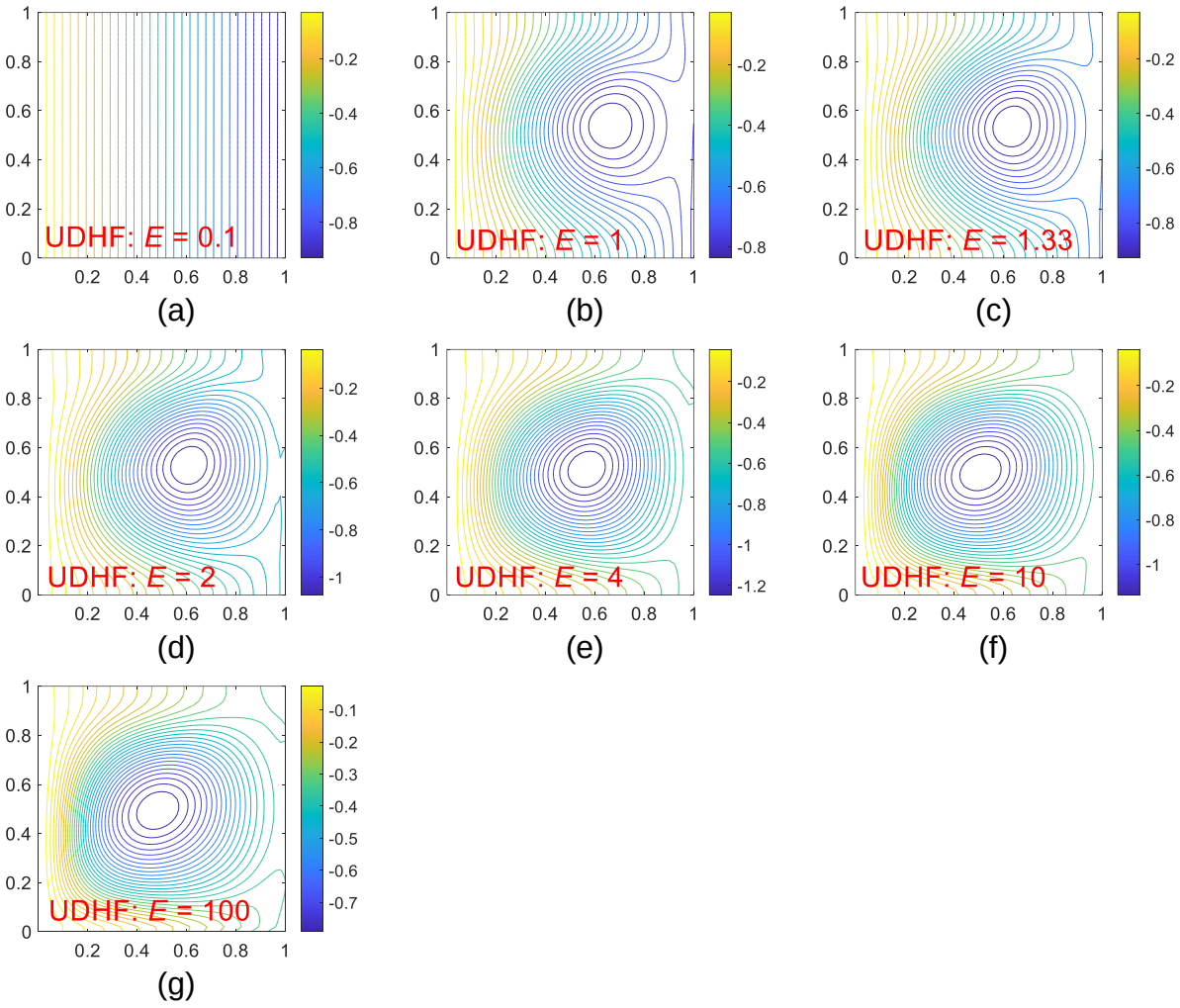

Fig. 4.32: Effect of optical thickness on heatlines ($Ra = 10^5$, $Pr = 10$): (a). $E = 0.1$, $H_{max} = 0.96$ (b). $E = 1$, $H_{max} = 0.86$ (c). $E = 1.33$, $H_{max} = 0.96$ (d). $E = 2$, $H_{max} = 1.11$ (e). $E = 4$, $H_{max} = 0.96$ (f). $E = 10$, $H_{max} = 0.96$ (g). $E = 100$, $H_{max} = 0.96$.

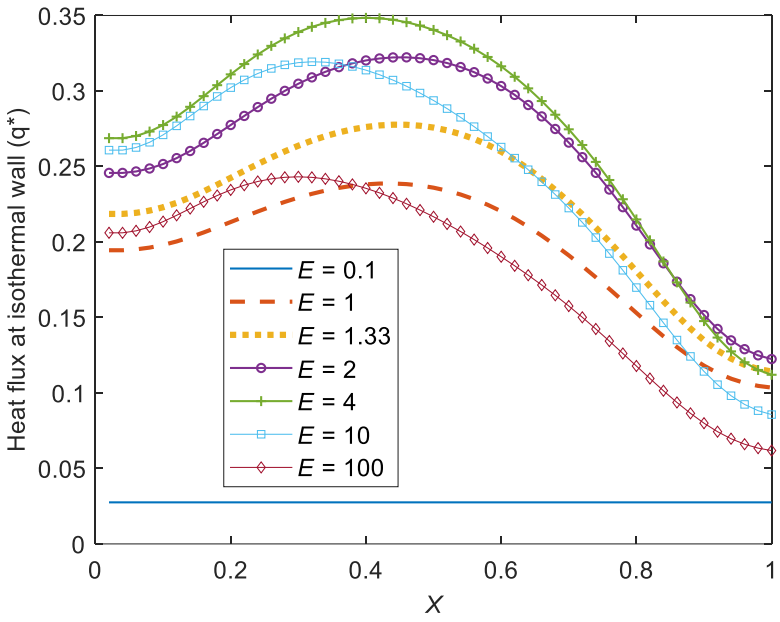

Fig. 4.33: Effect of optical thickness on heat flux at isothermal wall

(b). Effect of Rayleigh number

This section looks at how Rayleigh number affects the temperature and flow distribution and the local convective heat flux at the isothermal wall for the cavity (Fig. 4.34 and 4.35). Calculations were performed for Ra=10^2, 10^3, 10^4 and 10^5. Streamlines, isotherms and heatlines were generated to analyze the flow pattern in the cavity and the temperature distribution. The values of other parameters were fixed (AR=1, Bi^*=3, E=2, Pr=10).

Effect on streamlines

Up to Ra=10^4, the streamline structure remains similar with two whorls appearing symmetrically on the left and right side of the cavity. At Ra=10^5, there is a single whorl seen in the streamline structure at almost the center of the cavity. Beyond Ra=10^5, the flow becomes turbulent and is not included in the present investigation. The value of maximum stream function ranges from the order of 10^{-17} (at Ra=10^2) to 7.43 (at Ra=10^5) (Fig. 4.34).

Effect on isotherms

Up to Ra=10^4, the isotherms are seen to be horizontal and the maximum dimensionless temperature in the cavity is 0.16. At Ra=10^5, the isotherms become curved breaking the layered pattern of isotherms showing RB convection has set in. The maximum dimensionless temperature of the cavity drops to 0.12 as this happens as the liquid in the cavity begins to move around dissipating more heat (Fig. 4.34).

Effect on heatlines

Up to Ra=10^4, the heatlines appear to be vertical, perpendicular to the isotherms showing that most of the heat transfer takes place due to conduction between the layers at different temperatures and the maximum heat function in the cavity is 0.53. At Ra=10^5, the heatlines become curved breaking the pattern of vertical heatlines showing that convection has set in. The maximum value of heat function the cavity increases to 1.1107 (Fig. 4.34).

Effect on local heat flux at top isothermal wall

Convective heat flux at the top isothermal wall and the transmitting glass wall has been calculated and plotted at Ra = 10^2 and Ra = 10^5. The plots for Ra = 10^3 and 10^4 have been omitted as they coincide with that of Ra = 10^2.

As the Rayleigh number increases, the heat flux at the isothermal wall also increases. At low values of Ra, the heat flux remains constant at all values of 'X', as the temperature in the cavity is stratified and at a particular value of 'Y', the temperature remains almost the same. At Ra = 10^5, the heat flux at the isothermal wall shows a maximum value in the middle at around X = 0.5 (Fig. 4.35).

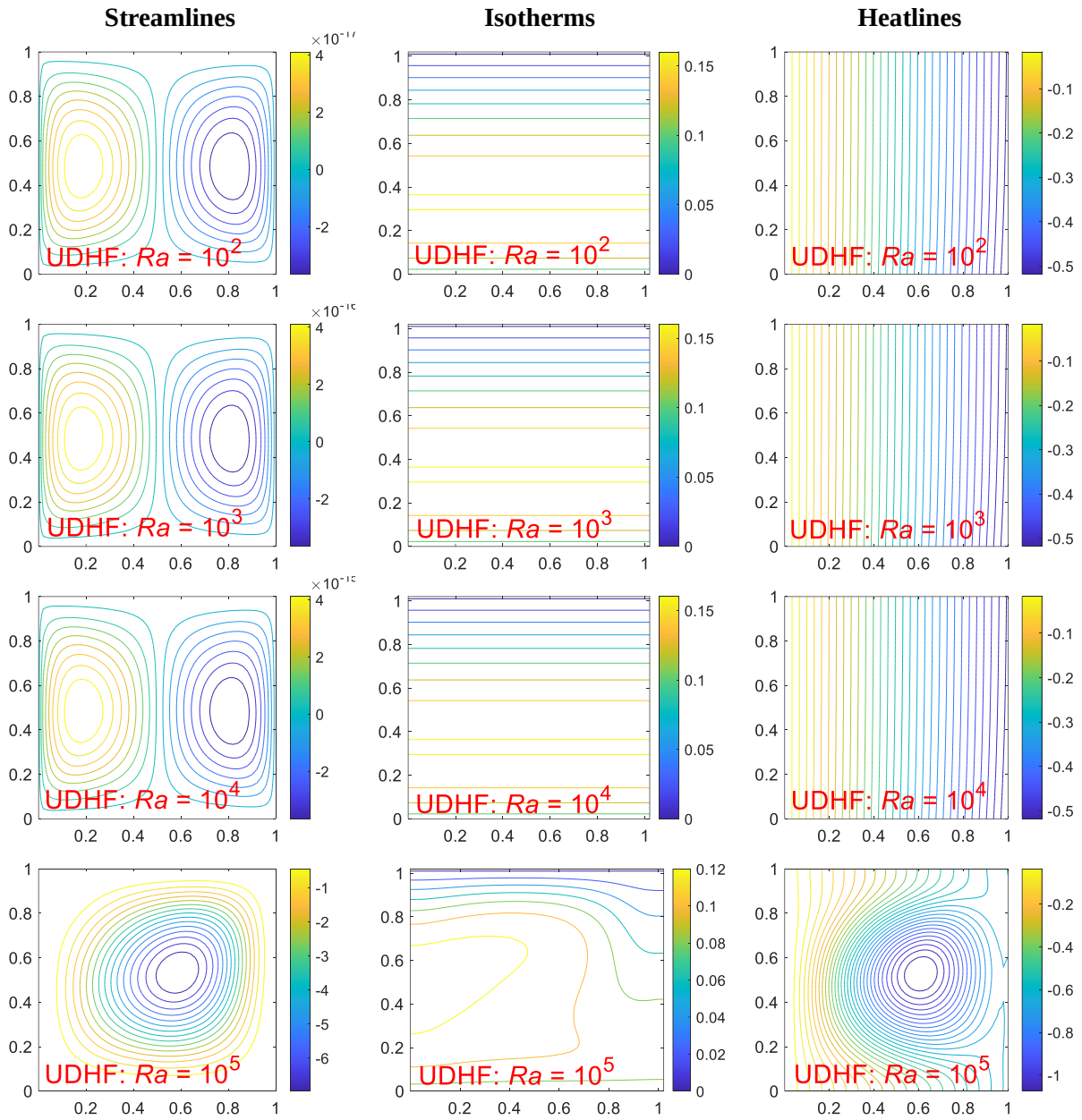

Fig. 4.34: Effect of Rayleigh number (Ra = 10^2, 10^3, 10^4, 10^5) on flow structure (streamlines), temperature distribution (isotherms) and heat flow (heatlines) (E = 2, Pr = 10, Bi^* = 3, AR = *1*): (Row1). Ra = 10^2, $|\Psi_{max}|$ = 4.21×10^{-17}, $|H_{max}|$ = 0.53, $|T_{max}|$ = 0.16; (Row 2). Ra = 10^3, $|\Psi_{max}|$ = 4.21×10^{-16}, $|H_{max}|$ = 0.53, $|T_{max}|$ = 0.16; (Row 3). Ra = 10^4, $|\Psi_{max}|$ = 4.22×10^{-15}, $|H_{max}|$ = 0.53, $|T_{max}|$ = 0.16; (Row 4). Ra = 10^5, $|\Psi_{max}|$ = 7.4311, $|H_{max}|$ = 1.11, $|T_{max}|$ = 0.13.

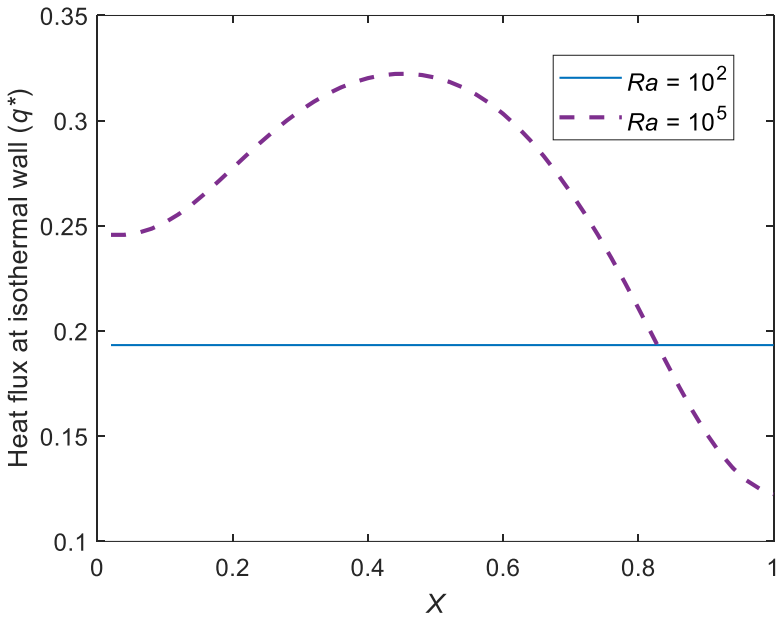

Fig. 4.35: Effect of Rayleigh number on heat flux at isothermal wall.

(c). Effect of Prandtl Number

This section looks at how gradually varying Prandtl number affects temperature, fluid and heat flow distribution (Fig, 4.36, 4.37, 4.38 and 4.39). Numerical analysis was carried out for increasing order of magnitude of *Pr* (=0.01, 0.1, 1, 10, 100 and 1000). Streamlines, isotherms and heatlines are plotted to show the effect of varying Prandtl number.

There is a gradual transition observed in the flow and temperature contours as *Pr* increases. While conduction dominates at low Prandtl numbers, convection is the dominant heat transfer mechanism at higher Prandtl numbers. However, there is insignificant change in the contours beyond *Pr*=10. All the other values are kept constant i.e., $Ra = 10^5$, $E = 2$, $Bi^* = 3$, $AR = 1$.

Effect on streamlines

The value of maximum stream function Ψ_{max} increases as *Pr* increases. It increases from a low value of 1.39×10^{-9} to 7.46 for $Pr = 0.01$ to 1000. As it can be seen there is negligible variation of Ψ_{max} as *Pr* becomes greater than 10. This becomes clear from the plot of streamlines which remain unchanged as *Pr* increases above 10. At lower Prandtl number, there are two whorls visible in the

cavity whereas at higher Prandtl numbers a single circular whorl is seen in the streamline pattern. (Fig. 4.36).

Effect on isotherms

At low Prandtl number (Pr=0.01), the isotherms are horizontal. As Prandtl number increases, the isotherms become more curved. The maximum temperature in the cavity decreases as Prandtl number increases due to convection and dissipation of heat. (Fig. 4.37).

Effect on heatlines

At low Prandtl number (Pr=0.01), the heatlines are vertical. As Prandtl number increases, the heatlines become more curved. The maximum heat function in the cavity increases as Prandtl number increases. (Fig. 4.38).

Effect on local heat flux at top isothermal wall

Convective heat flux at the top isothermal wall and the transmitting glass wall has been calculated and plotted at Pr = 0.01, 0.1, 1, 10, 100. At very low Prandtl number Pr = 0.01, the heat flux is almost constant showing that the flux does not change with 'X' and the cavity temperature is constant for a particular value of *'Y'* as is also evident from the isotherms.

At higher Prandtl numbers, the fluid inside the cavity begins to undergo convective motion. The maximum flux occurs at approximately the middle of the cavity (X = 0.5). The results don't vary much at Prandtl numbers beyond 10. (Fig. 4.39).

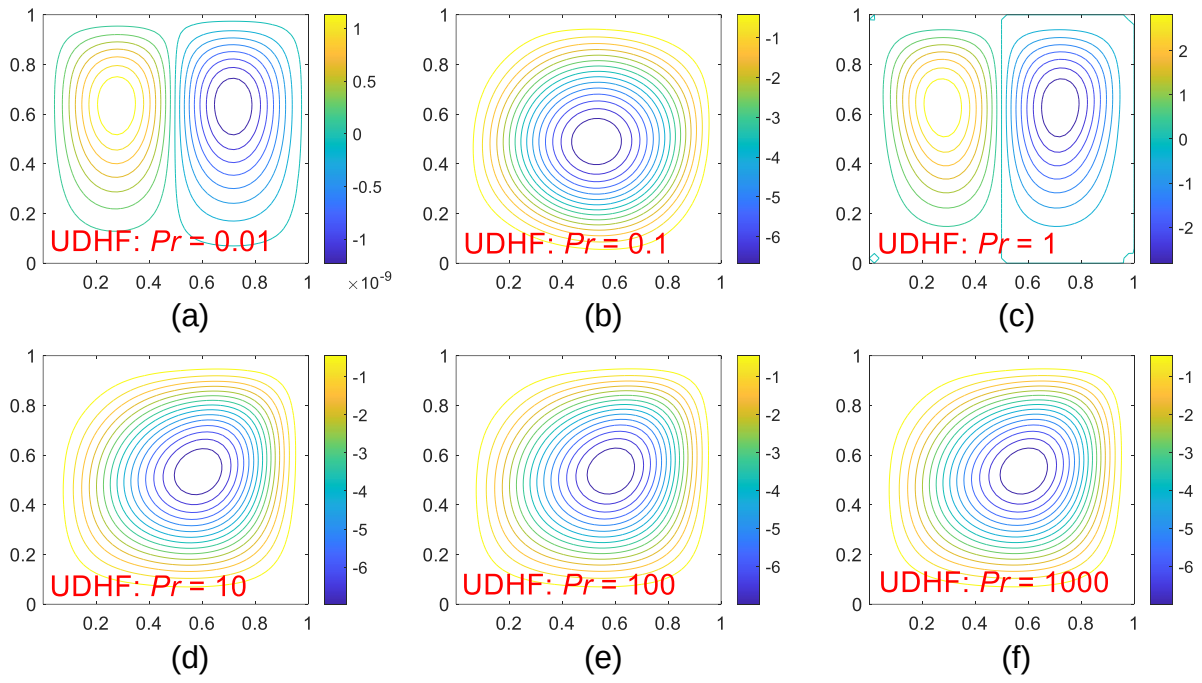

Fig. 4.36: Effect of Prandtl number on flow structure (streamlines) ($Ra = 10^5$, $E = 2$, $Bi^* = 3$, $AR = 1$): (a). $Pr = 0.01$, $|\Psi_{max}| = 5.35\times10^{-14}$ (b). $Pr = 0.1$, $|\Psi_{max}| = 5.35$ (c). $Pr = 1$, $|\Psi_{max}| = 6.2020$ (d). $Pr = 10$, $|\Psi_{max}| = 7.4311$ (e). $Pr = 100$, $|\Psi_{max}| = 9.3364$ (f). $Pr = 1000$, $|\Psi_{max}| = 10.0918$.

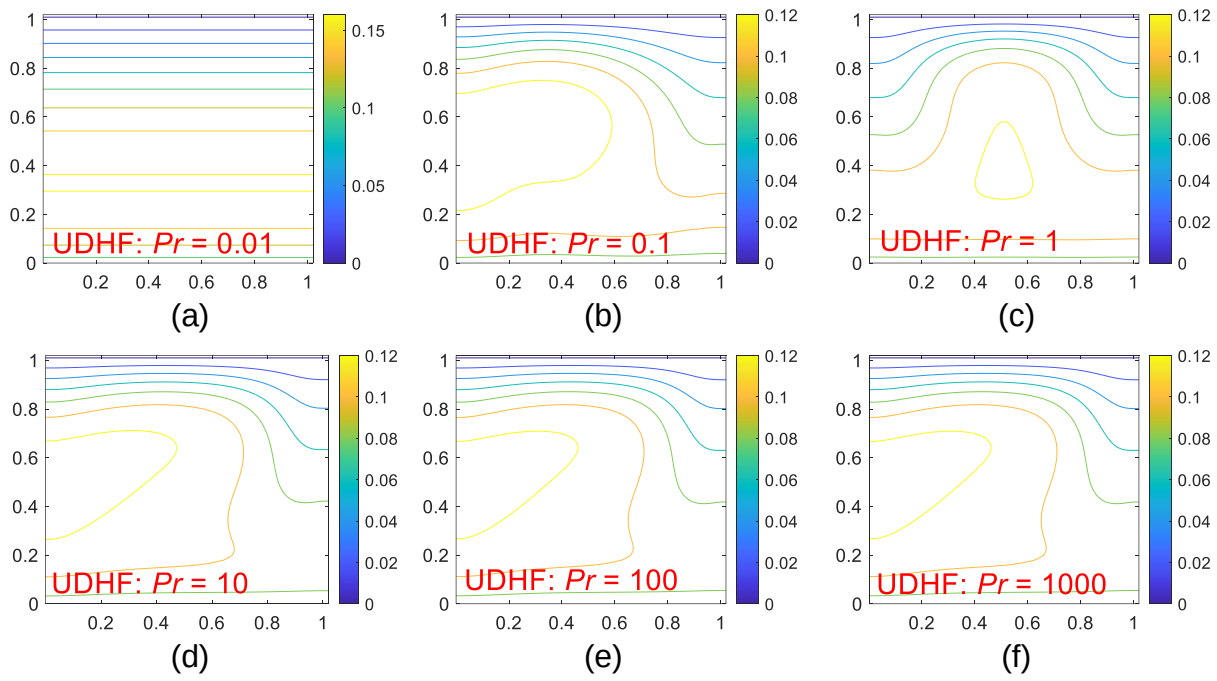

Fig. 4.37: Effect of Prandtl number on temp. distribution (isotherms) ($Ra = 10^5$, $E = 2$, $Bi^* = 3$, $AR = 1$): (a). $Pr = 0.01$, $T_{max} = 0.16$ (b). $Pr = 0.1$, $T_{max} = 0.13$ (c). $Pr = 1$, $T_{max} = 0.12$ (d). $Pr = 10$, $T_{max} = 0.13$ (e). $Pr = 100$, $T_{max} = 0.13$ (f). $Pr = 1000$, $T_{max} = 0.13$.

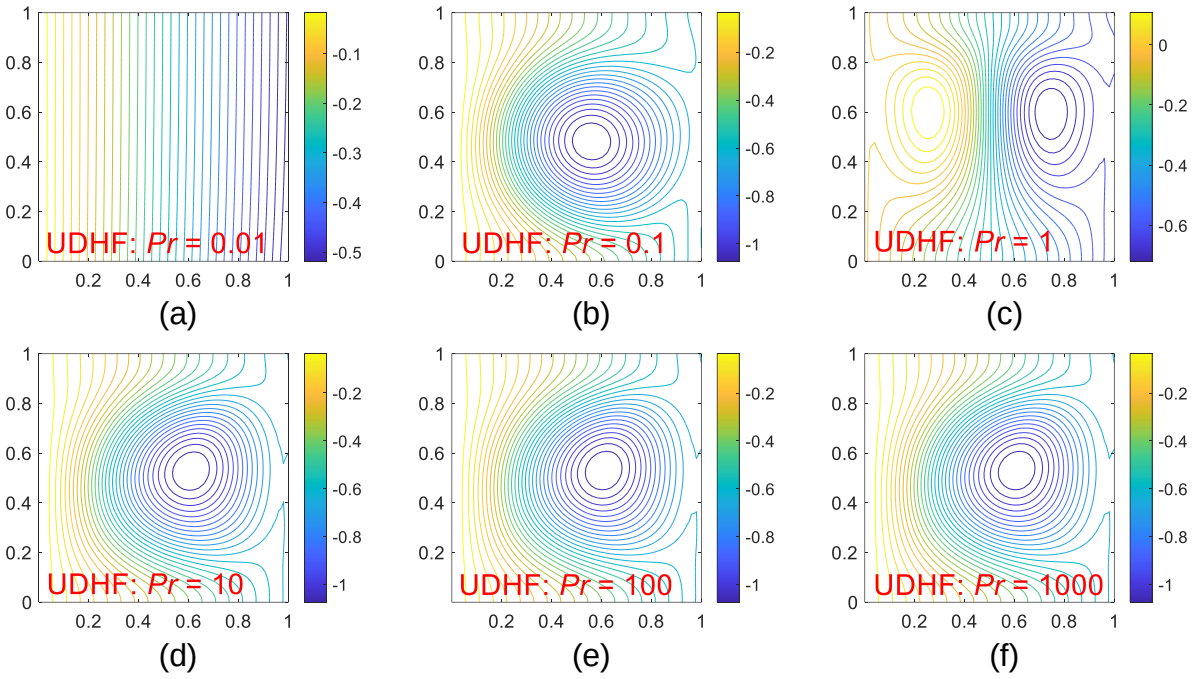

Fig. 4.38: Effect of Prandtl number on heatlines ($Ra = 10^5$, $E = 2$, $Bi^* = 3$, $AR = 1$): (a). $Pr = 0.01$, $H_{max} = 0.53$ (b). $Pr = 0.1$, $H_{max} = 0.64$ (c). $Pr = 1$, $H_{max} = 0.63$ (d). $Pr = 10$, $H_{max} = 1.11$ (e). $Pr = 100$, $H_{max} = 1.09$ (f). $Pr = 1000$, $H_{max} = 1.09$.

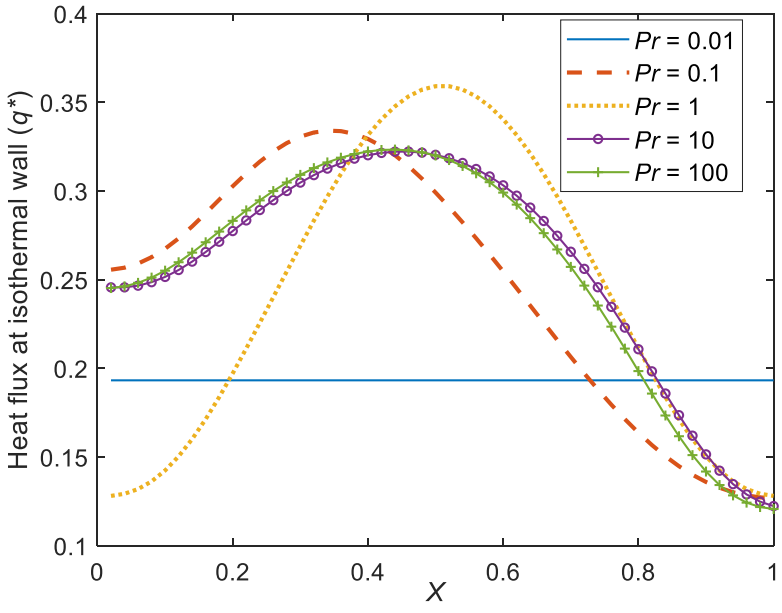

Fig. 4.39: Effect of Prandtl number on heat flux at isothermal wall.

(d). Effect of modified Biot Number

This section looks at how gradually varying Biot number affects temperature, fluid and heat flow distribution (Fig. 4.40 and 4.41). Numerical analysis was carried out for increasing order of magnitude of Bi^* (= 0,1,2,3,4 and 5). Increasing Biot number denotes increasing convection and radiation losses at the transmitting glass plate. All the other values are kept constant i.e., $Ra = 10^5$, $E = 2$, $Pr = 10$, $AR = 1$.

Effect on streamlines

At low Biot numbers ($Bi^* = 0$ and 1), the streamlines appear as two distinct whorls placed symmetrically in the cavity. The value of maximum stream function in the cavity increases up to $Bi^* = 2$, after which it decreases. This occurs as increasing the heat losses first causes a disruption in temperature distribution at the transmitting wall which causes greater disturbance in the fluid cavity and when losses become higher after a certain point the stream function decreases once again as lesser heat is absorbed by the fluid.

Effect on isotherms

At low Biot numbers ($Bi^* = 0$ and 1), the isotherms appear as bell shaped curve in the cavity at its middle. At higher Biot numbers, the isotherms don't change drastically in their appearance and there is a single roll pattern which appears. The value of maximum dimensionless temperature in the cavity decreases as Biot number is increased which is due to increasing convection losses.

Effect on heatlines

At low Biot numbers ($Bi^* = 0$ and 1), the heatlines appear as two whorls in the cavity on the left and right sides. At higher Biot numbers, the heatlines don't change drastically in their appearance and there is a single whorl pattern which appears slightly towards the right of cavity. The value of maximum heat function in the cavity decreases as Biot number is increased.

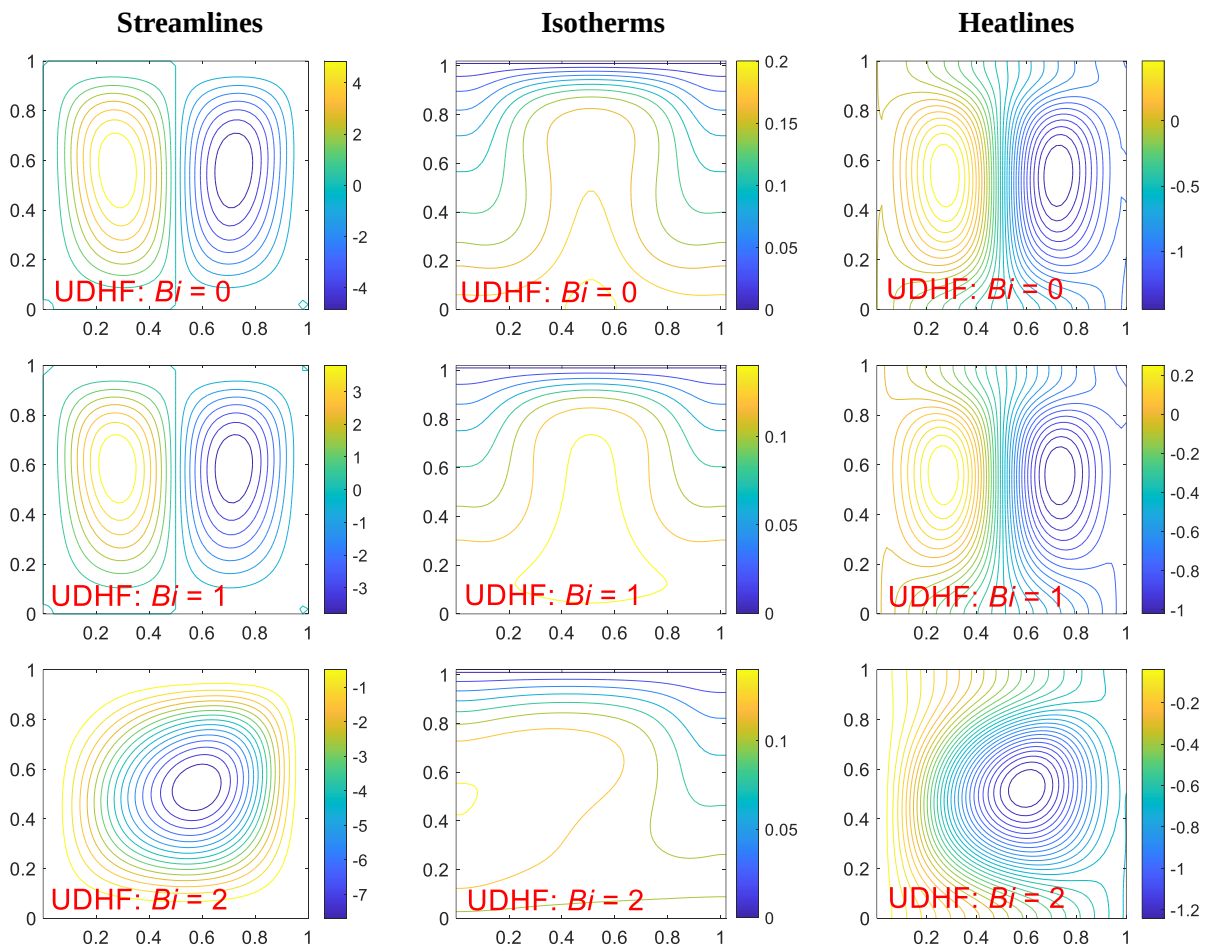

Fig. 4.40: Effect of lower Biot numbers (Bi^* = 0, 1, 2) on flow structure (streamlines), temperature distribution (isotherms) and heat flow (heatlines) (E = 2, Pr = 10, Ra = 10^5, AR = *1*): (Row1). Bi = 0, $|\Psi_{max}|$ = 5.54, $|H_{max}|$ = 1.51, $|T_{max}|$ = 0.20; (Row 2). Bi = 1, $|\Psi_{max}|$ = 4.34, $|H_{max}|$ = 0.29, $|T_{max}|$ = 0.15; (Row 3). Bi = 2, $|\Psi_{max}|$ = 8.21, $|H_{max}|$ = 1.28, $|T_{max}|$ = 0.14.

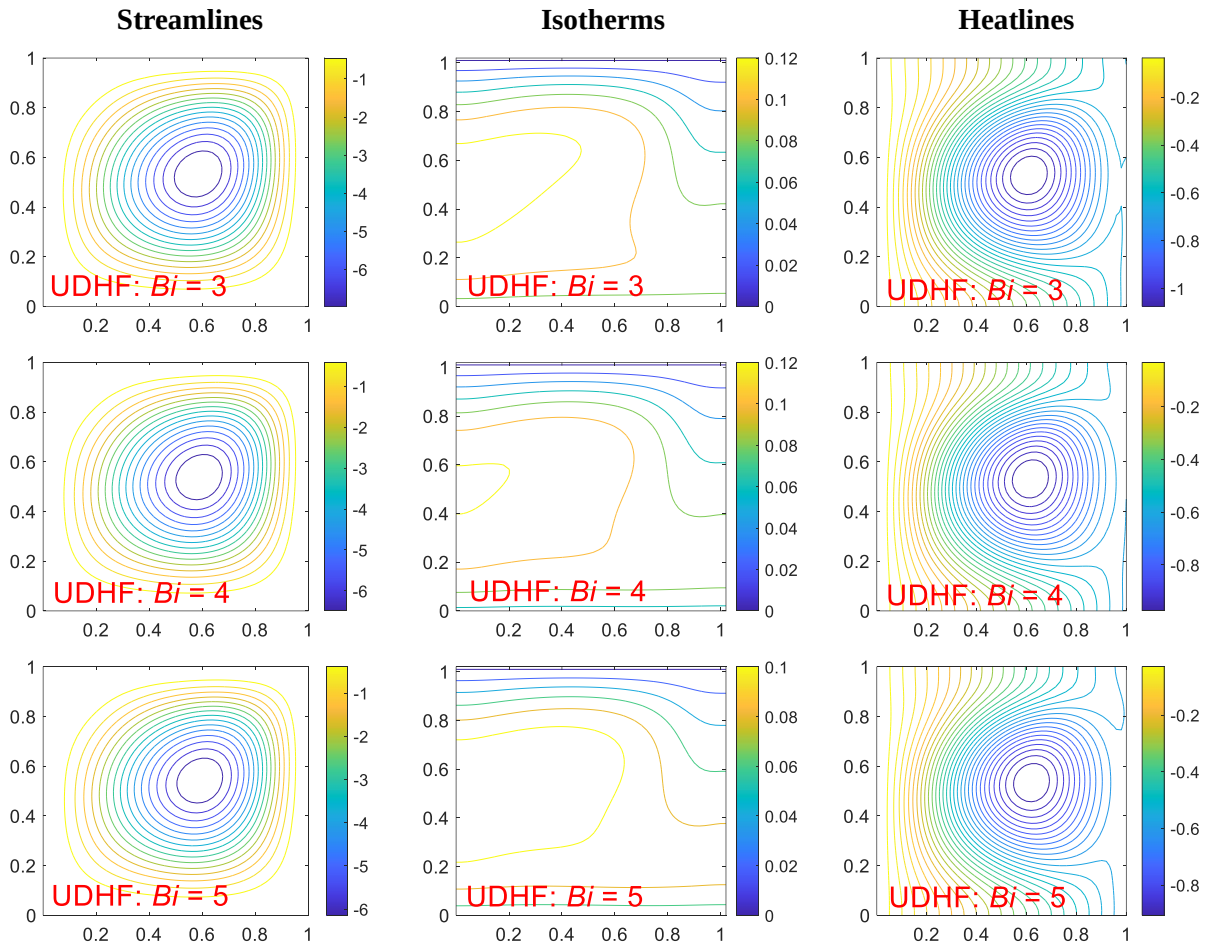

Fig. 4.41: Effect of higher Biot numbers (Bi^* = 3, 4, 5) on flow structure (streamlines), temperature distribution (isotherms) and heat flow (heatlines) (E = 2, Pr = 10, Ra = 10^5, AR = *1*): (Row1). Bi = 3, $|\Psi_{max}|$ = 7.43, $|H_{max}|$ = 1.11, $|T_{max}|$ = 0.13; (Row 2). Bi = 4, $|\Psi_{max}|$ = 6.92, $|H_{max}|$ = 1.00, $|T_{max}|$ = 0.12; (Row 3). Bi = 5, $|\Psi_{max}|$ = 6.55, $|H_{max}|$ = 0.94, $|T_{max}|$ = 0.12.

(e). Effect of aspect ratio

In this section, the effect of varying aspect ratio on the temperature, fluid and heat flow distribution (Fig. 4.42) is presented. Numerical analysis was carried out for increasing order of magnitude of AR (= 0.1, 0.5, 1, 2 and 10). It was observed that at aspect ratios 2 and 10, the flow becomes turbulent and hence streamlines, isotherms and heatlines were not plotted for those scenarios. This happens because the heated area in those cases is much higher than the heating area of the cavity.

Effect on streamlines

At low aspect ratios (*AR* = 0.1 and 0.5), the streamlines appear as two distinct whorls placed symmetrically in the cavity on the left and the right side. The value of maximum stream function in the cavity increases as aspect ratio is increased up to 1. This occurs as due to the low aspect ratio, the fluid does not move around freely between the transmitting wall at the bottom and the cooling wall at the top of the cavity due to friction. The left side of the isotherms show higher temperature and lower temperature on the right-side wall indicating hotter liquid rising along the left adiabatic wall and descending along the right wall. At *AR* = 0.5, the whorls on the left and right are more symmetric with the whorl on the left wall occupying slightly more area in the cavity. At *AR* = 1, there is a single whorl at the center of the cavity.

Effect on isotherms

At aspect ratios lower than 1, the isotherms are horizontal. The maximum temperature increases as the aspect ratio increases (from 0.0043 to 0.1295) which is due to increase in the distance between the top and bottom wall. In a square cavity (*AR* = 1), the isotherms shown a single roll pattern indicating greater mixing of fluid.

Effect on heatlines

At aspect ratios lower than 1, the heatlines are somewhat vertical however not entirely. The maximum heat function increases (from 0.98 to 1.11) as the aspect ratio increases. It is interesting to note that the heatlines are not perpendicular to the isotherms at low aspect ratios even when the isotherms are horizontal lines. This shows that at low aspect ratios, even when the temperature of the fluid in the cavity is stratified, majority of the heat is carried by the movement of fluid.

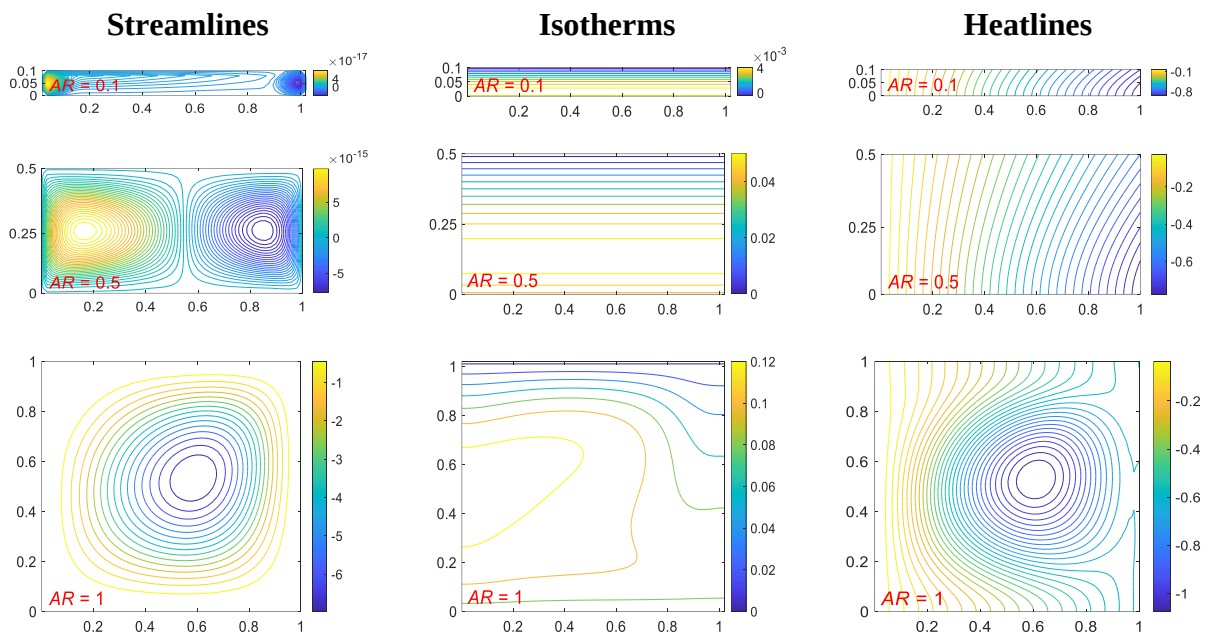

Fig. 4.42: Effect of aspect ratio (AR = 0.1, 0.5, 1) on flow structure (streamlines), temperature distribution (isotherms) and heat flow (heatlines) (E = 2, Pr = 10, Ra = 10^5, Bi^* = 3): (Row1). AR = 0.1, $|\Psi_{max}|$ = 7.79×10^{-17}, $|H_{max}|$ = 0.98, $|T_{max}|$ = 0.0043; (Row 2). AR = 0.5, $|\Psi_{max}|$ = 1.006×10^{-14}, $|H_{max}|$ = 0.80, $|T_{max}|$ = 0.05; (Row 3). AR = 1, $|\Psi_{max}|$ = 7.43, $|H_{max}|$ = 1.11, $|T_{max}|$ = 0.13.

(f). Impact of Rayleigh number, Prandtl number and optical thickness on the useful heat gain at the isothermal wall (Y = 1).

Fig. 4.43 shows the cumulative heat flux for the different Rayleigh and Prandtl numbers and the optical thickness of the fluid. The useful cumulative flux remains almost constant for Rayleigh numbers up to 10^4 but it increases suddenly at Ra = 10^5. It increases with Prandtl number up to Pr =10 beyond which there is negligible change. The cumulative flux at isothermal wall (Q^*) is calculated as follows:

$$Q^* = \int_{X=0}^{X=1} \frac{\partial T^*}{\partial Y} dX \qquad (4.20)$$

It also increases with fluid opacity up to E = 2. However, on comparing the values for E = 2 and E = 4 at low Rayleigh numbers, it was found that the value of flux is higher for E = 2. This is

because at low Rayleigh numbers (10^2-10^4) and higher optical thickness values, the convective motion of the liquid is not strong, and the effect of radiation is stronger at the transmitting wall than at the isothermal wall. However, this is not the case at higher Rayleigh numbers (10^5) where cumulative flux values for $E = 4$ are higher than those at $E = 2$. This same trend was also seen for a cavity irradiated from the side.

Fig. 4.24 shows the variation of cumulative flux with Rayleigh number for different optical thickness values (E ranges from 0.1 to 100). The Prandtl number is kept constant ($Pr = 10$). As optical thickness increases from $E = 1$ to $E = 2$, the cumulative flux at isothermal wall is consistently high across all Rayleigh numbers from 10^2 to 10^5. Beyond $E = 2$, i.e., for $E = 4$, the cumulative flux drops at low Rayleigh numbers whereas at $E = 10$ and 100, the cumulative flux drops at all Rayleigh numbers. This is because as the fluid opacity is increased, the system emulates surface heating with the incident radiation rapidly being absorbed at the transmitting wall and the energy is not carried to the isothermal wall at the top.

Another important observation is the existence of regimes – a conduction dominated regime ($10^2 \leq Ra \leq 10^4$) where the heat flux at the isothermal wall is minimum and a convection regime ($Ra = 10^5$) where there is a sharp increase in the value of the cumulative heat flux (Q^*). Unlike the case of cavities heated from side there is no transition regime between Ra values of 10^4 and 10^5 indicating either an abrupt jump or a very small transition regime between 10^4 and 10^5. Beyond $Ra = 10^5$, the flow becomes turbulent.

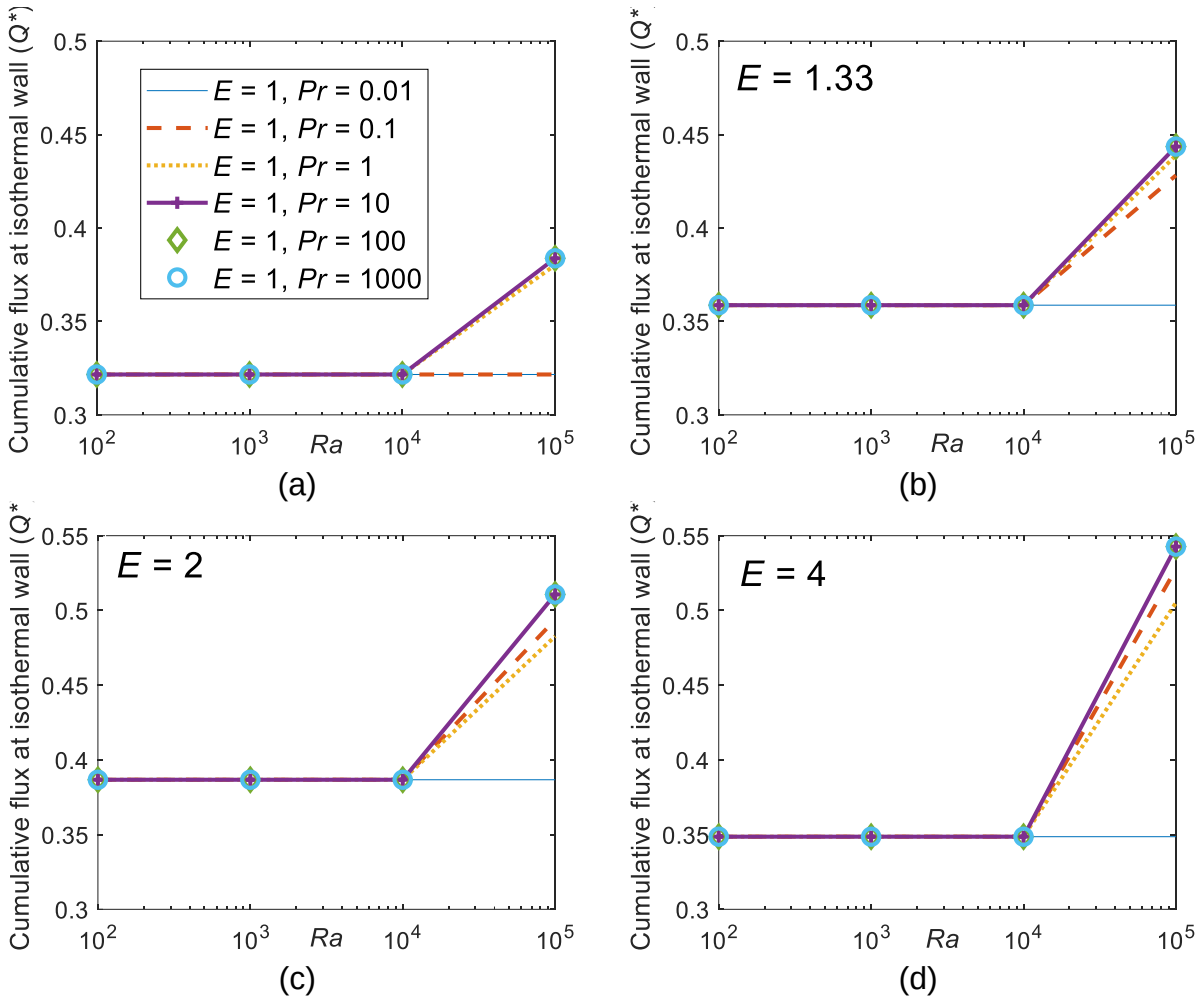

Fig. 4.43: Impact of Rayleigh number, Prandtl number and optical thickness of fluid on the cumulative heat flux at the isothermal top wall (a). $E = 1$ (b). $E = 1.33$ (c). $E = 2$ and (d). $E = 4$.

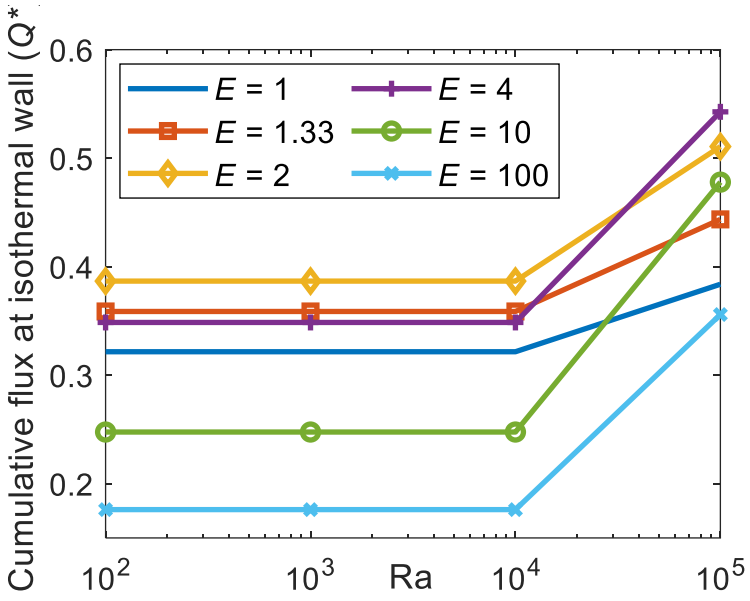

Fig. 4.44: *Ra* vs cumulative flux (Q^*) for different fluid opacity values (*Pr* = 10).

4.3.4.2 Effect of linearly varying heat flux

This section considers the effect of linearly varying heat flux. The net heat flux entering the cavity in the case of linearly varying flux is the same as that entering the cavity for the case of uniformly distributed heat flux.

The effect of linearly varying heat flux on the temperature and heat and flow distribution in the cavity is studied through streamlines, isotherms and heatlines (Fig. 4.45). The flux varies from zero to maximum from the left to the right of the cavity. The Rayleigh number is kept constant at 10^5 and the optical thickness is varied (*E* = 1, 2 and 10).

It is observed that the values of $|\Psi_{max}|$ for the different optical thicknesses are 6.25, 7.57, 9.77. Similarly, the values of θ_{max} are 0.0946, 0.1220 and 0.1217 and the values of H_{max} are 0.7991, 0.9475 and 0.7752 for *E* = 1, 2 and 10, respectively.

The value of stream function increases consistently as the value of optical thickness increases showing increased convection in the cavity. The maximum temperature in the cavity increases first with optical thickness and decreases thereafter. As optical thickness increases, more energy is absorbed by the fluid thus increases the convection, however as convection increases, the energy is dissipated more readily by the fluid thus decreasing the maximum temperature in the cavity.

Compared to the case of uniform heating, higher temperatures appear on the right side of the cavity instead of the left side of the cavity when the higher temperatures are on the left side of the cavity.

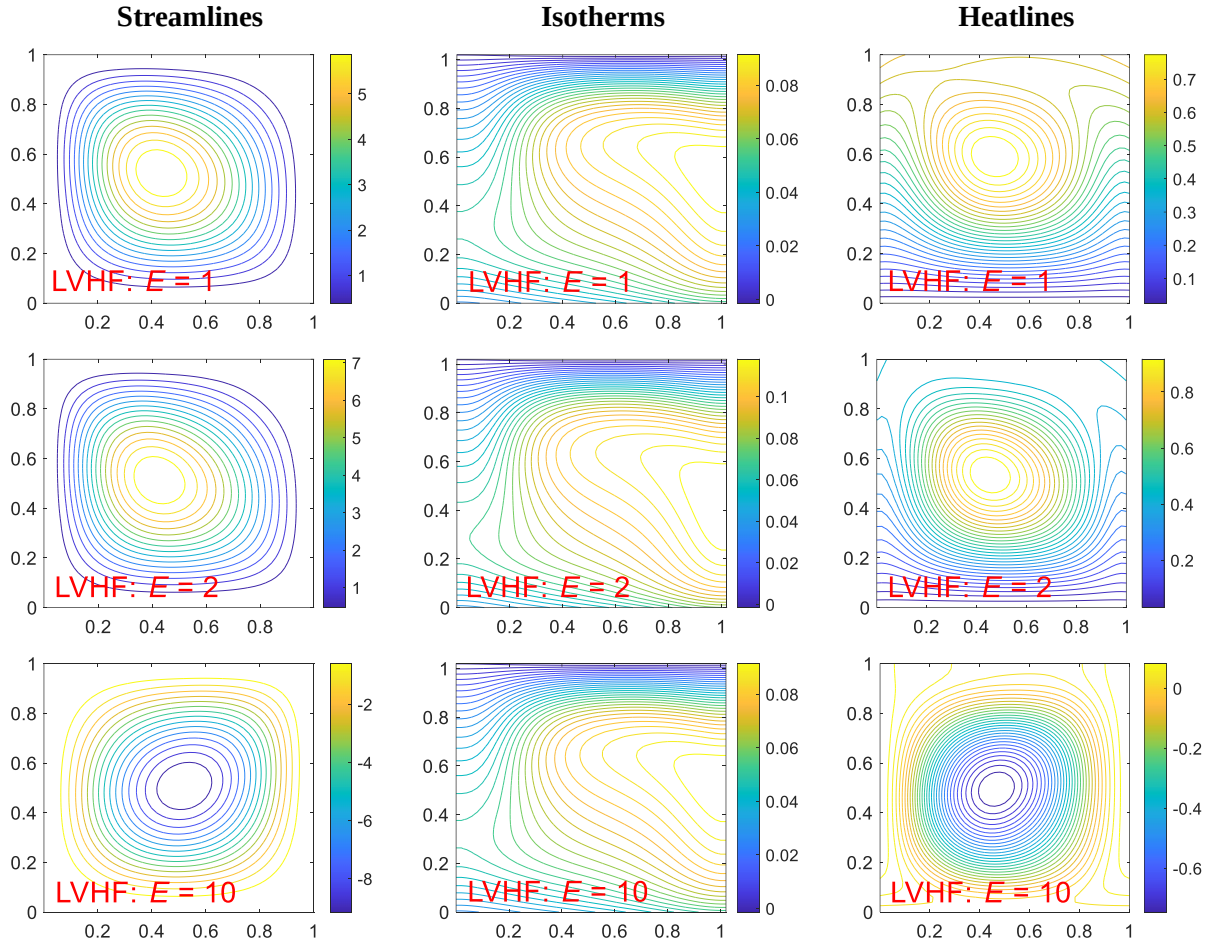

Fig. 4.45: Streamlines, isotherms and heatlines for linearly varying heat flux for different optical thicknesses ($Ra = 10^5$, $Pr = 10$, $Bi^* = 3$, $AR = 1$).

4.3.5 Scope of the study on natural convection in cavities

The previous sections pertaining to natural convection in cavities dealt with the results obtained from varying different parameters and their effects on the fluid and heat flow and temperature distribution in a cavity heated volumetrically by radiation incident from the side. This section discusses the scope of the present study to find applications where these findings can be suitably applied.

To translate the dimensionless results to a language more conducive to understanding the application of this work in direct absorption solar collectors, the following procedure is adopted.

The values of some variables such as the values of physical properties of the working fluid, and the ambient temperature are fixed.

g = 10 m/sec^2; $Pr = \frac{\upsilon}{\alpha} = 10$; α=4.03×10^{-7}; υ = 4.03×10^{-6};

β = 0.000979/°C; k_l = 0.1363 W/mK

By fixing these values, the values of Rayleigh number became directly proportional to the value of incident flux. The graph showing Rayleigh number vs the incident flux is given in Fig. 5.1. From the graph, it can be inferred that the Rayleigh number defined in the present study which is based on the distance between two vertical walls, is in the laminar range when the cavity size is small. However, it quickly transitions to the turbulent region as cavity size is increased. This is due to the viscous effects of the walls of the cavity which becomes less pronounced as the cavity size decreases. Since the present study pertains to laminar natural convection taking place in the cavity (Ra $\leq 10^8$ for side-heated cavity and Ra $\leq 10^5$ for bottom heated cavity), it is suitable for applications which involve either very small values of '*L*' or low values of incident flux. Potential applications are:

- Direct absorption solar collectors and other solar applications operating at low flux conditions.
- Double glazed windows
- The part of the study which deals with non-uniform flux can find use in design of receivers with focusing mechanisms which can be engineered to distribute flux in a preferred

orientation to achieve desired temperature and flow distribution which can minimize thermal stresses and enhance safety (Ya Ling et al., 2019).

The study also takes into consideration the effect of varying the Prandtl number over a very wide range (0.01-1000). Such a wide range of values encompasses numerous fluids from highly conductive liquid metals to viscous oils. Liquid metals are especially important in cooling systems for nuclear reactors. Similarly, other parameters varied in this study are optical thickness which is varied from very low to high to emulate volumetric heating to surface heating, respectively. Similarly, aspect ratio has been varied from 0.1 to 10. Different configurations of incident heat flux are also studied, the results can be used in different applications. Understanding the heat transfer and fluid flow processes in such systems can help in improving the efficiency and safety of engineering applications. By predicting temperature distribution in the cavity can help in mitigating risks by identifying potential hotspots and preventing any damage to appliances.

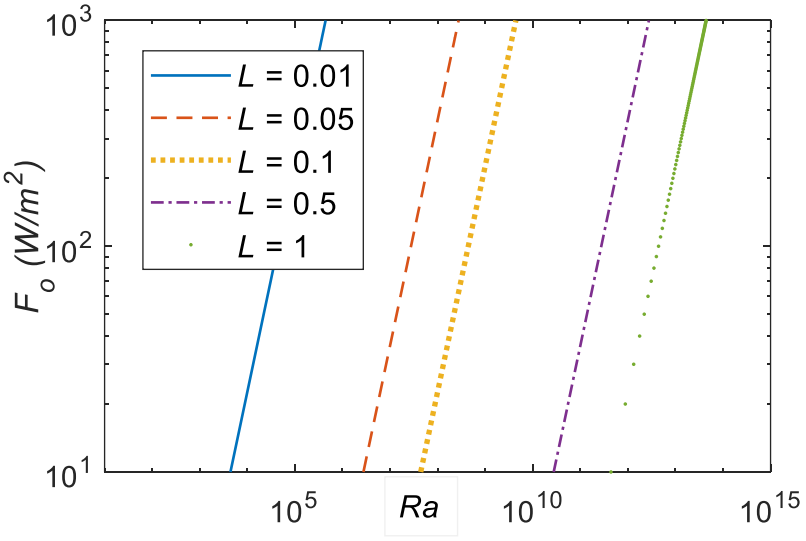

Fig. 4.46: Rayleigh number vs Incident flux.

5. Conclusions and Future Scope

5.1 Aims

This chapter brings together the work presented in previous chapters, discusses its significance and its limitations, and relates the scope for future studies in this sphere and it is divided into two sections accordingly: (1). Significance and main contributions of the work (2). Limitations and future scope of work.

5.2 Significance and main contributions of the work

The present study provides a detailed investigation into the phenomenon of volumetrically heated, fluid-filled systems and the role they can play in improving solar thermal systems. The reason why employing volumetric heating mechanism instead of surface heating in solar receivers can provide better efficiency are as follows:

- In surface absorption-based heating of receivers, there develops an energy barrier between the fluid and the surface. The surface temperature leaps as it absorbs incident radiation: however, energy is not transferred efficiently to the working fluid. Volumetric absorption-based heating is better as a major bulk of incident radiation is directly absorbed by the fluid.
- Volumetric absorption-based receivers also reduce convection and emission losses which are directly proportional to the fourth power of the absolute temperature of the surface. Since the receiver surface temperatures are way higher for surface absorption-based receivers than they are for volumetric absorption-based receivers – they suffer greater losses.

Thus, volumetric absorption-based receivers enable greater proportion of the incident radiation to be transmitted to the working fluid and reduce emission and convective losses which translates to higher receiver efficiencies.

The present study considers both forced and natural convection in volumetrically heated systems with special emphasis on their usefulness in solar thermal systems. The temperature and flow distribution in such systems, the various parameters governing those and finding optimum designs

under different operating conditions with respect to their use in solar thermal systems is investigated.

Solar thermal power plants operating all over the world employ surface absorption-based receivers and differ from each other in their concentrating technology, receiver design, size etc. The use of volumetric absorption-based receivers instead can help in improving the efficiency of the receiver component of the solar thermal system through capture of a higher fraction of the incident energy and by reducing radiative and convective losses. The present work studies volumetric systems with forced and natural convection in channels and enclosures, respectively.

Intricate mathematical modelling frameworks have been developed and employed to study the phenomena of volumetric heating in a host of configurations and receiver geometries; several parameters pertaining to fluid flow, receiver geometry and optical and thermophysical properties of the working fluid have also been taken into consideration. The mathematical modelling techniques used in the present work can be extrapolated to other such systems as well. Thus, the study makes a significant contribution in advancing the knowledge in the field of solar thermal systems.

The main contributions of the study are summarized under two heads, those from the study of (1). forced convection in channels and (2). natural convection in cavities.

5.2.1 Contributions of the study of forced convection in channels

(1). Development of an intricate mathematical modelling framework to study solar thermal systems (viz. channels with surface and volumetric heating) with different configurations of optical elements. The effect of optical thickness of the working fluid, solar concentration ratio, Reynolds number, inlet fluid temperature and height of the channel on the performance parameters of the system has been assessed.

(2). Through the comparison of surface and volumetric absorption-based heating systems. It was found that volumetric systems provide 45-51% enhancement in efficiency over surface absorption based systems particularly at high inlet temperatures and solar concentration ratios, and low Reynold numbers. The efficiency of surface absorption-bases systems dips down drastically as the surface temperatures are exceedingly high relative to the average fluid temperatures.

(3). The efficiency of systems with heat mirror casings is lower than those with glass casings at low solar concentration ratios and inlet temperatures of the fluid because of low transmissivity of heat mirrors but they perform better at high concentration of incident solar energy and inlet fluid temperature as they block emission losses from the system at high temperatures thereby offsetting losses due to lower transmissivity.

(4). The exit fluid temperature curves for surface and volumetrically heated systems show the phenomena of temperature inversion. While the temperature in surface absorption based systems is highest for the surface of the receiver, the temperature of the transmitting glass surface in volumetrically heated systems is lower than the topmost layer of liquid in contact with it.

5.2.2 Contributions of the study of natural convection in cavities

Table 5.1 provides a list of the contributions of the study of natural convection in cavities whilst comparing heating from the side and bottom.

Table 5.1: Contributions of the study of natural convection in cavities

Cavity heated from side	Cavity heated from bottom
Development of a mathematical modelling framework for a parametric investigation of fluids enclosed in a confined cavity heated volumetrically from side.	Development of a mathematical modelling framework for a parametric investigation of fluids enclosed in a confined cavity heated volumetrically from bottom.
Effect of Rayleigh, Prandtl and Biot numbers, optical thickness, and aspect ratio of the cavity on the temperature and fluid and heat flow distribution of the cavity. The effect of linearly varying heat flux is also studied.	Effect of Rayleigh, Prandtl and Biot numbers, optical thickness, and aspect ratio of the cavity on the temperature and fluid and heat flow distribution of the cavity. The effect of linearly varying heat flux has also been studied.
Use of heatlines to visualize the heat flow distribution.	Use of heatlines to visualize the heat flow distribution.
For cavities heated from the side, laminar flow exists for $Ra \leq 10^8$. Three distinct regimes are observed: a conduction dominated regime at $Ra \leq 10^3$; a transition regime occurs at $10^3 <$	For bottom heated cavities laminar flow exists up to $Ra \leq 10^5$. Two regimes are observed: a conduction dominated regime ($10^2 \leq Ra \leq 10^4$) and a convection regime ($Ra = 10^5$). There is

$Ra \leq 10^4$ and; at $Ra > 10^4$ a convection dominated regime is observed.	no transition regime between Ra values of 10^4 and 10^5 indicating either an abrupt jump or a very small transition regime between 10^4 and 10^5. Beyond $Ra = 10^5$, the flow becomes turbulent.
For cavities heated from the side, the aspect ratio is varied from 0.1 to 10 and the flow remains laminar throughout.	In cavities heated from bottom the aspect ratio is varied from 0.1 to 1. At aspect ratio greater than 1, the flow becomes turbulent.

5.3 Limitations and future scope of work

The work studies the phenomena of volumetric heating in channels and cavities in detail. However, there are certain limitations which are listed below:

(1). The work deals with laminar regimes of flow in both channels and cavities, however, conditions for laminar flow exists only under some operating conditions. The work can be extended to include the transitional and the turbulent regimes, whose understanding constitutes a rich research problem worthy of investigation.

(2). The study of fluid in cavities is parametric in nature and does not include spectral properties of the constituent elements of the system; future work can be carried out in this direction.

(3) Other geometries can be considered to study the phenomena of volumetric absorption of radiation in solar as well as other areas of application.

(4). There is a rising demand in industrial and domestic sectors to harness heat > 200^0C with unconcentrated sunlight using aerogels which are capable of drastically reducing heat losses while maintaining high transparency to solar radiation (Zhao et al., 2019). The mathematical framework used in the present study can be applied to aerogel-based systems to quantify their performance.

Appendix

A: Mathematical modeling of spectral optical properties

Glass

The transmissivity values for low-iron glass have been calculated utilizing data (optical constants 'n' and 'κ') from (Rubin, 1985). Once the values of 'n' and 'κ' are known, the reflectivity, transmissivity and absorptivity values for glass can be evaluated through the following steps:

The spectral internal transmissivity 'τ_a' can be calculated using,

$$\tau_{a,\lambda} = e^{-K_{e,\lambda} ds}, \tag{A1}$$

where,

$$K_{e,\lambda} = \frac{4\pi\kappa}{\lambda}, \tag{A2}$$

The effective spectral reflectance is evaluated from the Fresnel relations:

$$\begin{aligned}
\rho_{\perp,\lambda} &= \frac{(n_{vac}\cos\psi - w)^2 + v^2}{(n_{vac}\cos\psi + w)^2 + v^2} \\
\rho_{\parallel,\lambda} &= \frac{\left[(n_{h,\lambda}^2 - \kappa_{h,\lambda}^2)\cos\psi - n_{vac} w\right]^2 + \left[2 n_{h,\lambda}\kappa_{h,\lambda}\cos\psi - n_{vac} v\right]^2}{\left[(n_{h,\lambda}^2 - \kappa_{h,\lambda}^2)\cos\psi + n_{vac} w\right]^2 + \left[2 n_{h,\lambda}\kappa_{h,\lambda}\cos\psi + n_{vac} v\right]^2}, \\
\rho_{avg,\lambda} &= \frac{\rho_{\perp,\lambda} + \rho_{\parallel,\lambda}}{2}
\end{aligned} \tag{A3}$$

where,

$$2w^2 = \left(n_{h,\lambda}^2 - \kappa_{h,\lambda}^2 - n_{vac}^2 \sin^2\psi\right) + \sqrt{\left(n_{h,\lambda}^2 - \kappa_{h,\lambda}^2 - n_{vac}^2 \sin^2\psi\right)^2 + 4n_{h,\lambda}^2\kappa_{h,\lambda}^2}$$
$$2v^2 = -\left(n_{h,\lambda}^2 - \kappa_{h,\lambda}^2 - n_{vac}^2 \sin^2\psi\right) + \sqrt{\left(n_{h,\lambda}^2 - \kappa_{h,\lambda}^2 - n_{vac}^2 \sin^2\psi\right)^2 + 4n_{h,\lambda}^2\kappa_{h,\lambda}^2}, \quad \text{(A4)}$$

The spectral absorptivity for glass is then calculated from

$$a_\lambda = \varepsilon_\lambda = 1 - \tau_{a,\lambda} - \rho_{avg,\lambda}, \quad \text{(A5)}$$

In the backdrop of the fact that presently anti-reflective coatings are deposited over the glass to enhance solar weighted transmissivity; the spectral transmissivity values were scaled up such that the solar weighted transmissivity of glass is 97.8%. This value is consistent with that reported in the literature (Price et al., 2002) for glass envelopes employed in concentrating solar collectors.

Nanofluid

As radiation propagates through the nanofluid; its magnitude changes owing to absorption and scattering mechanisms. Attenuation of radiation due to scattering is negligibly small as the particles are much smaller than the wavelength of incident light which means that scattering occurs in the Rayleigh regime and absorption dominates (Freedman et al., 2018). Absorption and scattering mechanisms could be quantified using the following expressions:

$$K_{a,\lambda,bf} = \frac{4\pi\kappa}{\lambda}, \quad \text{(A6)}$$

where '$K_{a,\lambda}$' is the spectral absorption coefficient, 'κ' is the spectral index of absorption, and 'λ' is the wavelength.

The combined attenuation from absorption and scattering by nanoparticles is taken care of by extinction coefficient, given as,

$$K_{e,\lambda,np} = \frac{1.5 f_v Q_{e,\lambda}(\beta, m)}{d}, \quad \text{(A7)}$$

where, '$K_{e,\lambda}$' is the spectral extinction coefficient, 'f_v' is the volume fraction, 'd' is the characteristic dimension (hydrodynamic diameter, d = 30nm), 'β' is the size parameter, 'm' is the normalized refractive index and '$Q_{e,\lambda}$' is the extinction efficiency of the particles defined as follows (Tyagi et al., 2009):

$$\beta = \frac{\pi d}{\lambda}, \tag{A8}$$

$$m = \frac{m_{np}}{n_{bf}}, \tag{A9}$$

$$Q_{e,\lambda} = 4\beta \,\mathrm{Im}\left\{\frac{m^2-1}{m^2+2}\left[1+\frac{\beta^2}{15}\left(\frac{m^2-1}{m^2+2}\right)\frac{m^4+27m^2+38}{2m^2+3}\right]\right\} + \frac{8}{3}\beta^4 \,\mathrm{Re}\left\{\left(\frac{m^2-1}{m^2+2}\right)^2\right\} \tag{A10}$$

The values of 'κ' for base-fluid were obtained from (Hewakuruppu, 2016). The 'n' and 'κ' values for nanoparticles have been taken from (Maron, 1990; Stagg & Charalampopoulos, 1993).
Once the value of extinction coefficients is calculated for base-fluid and nanoparticles individually, the value of extinction coefficient for the nanofluid can be obtained simply by adding the two.

$$K_{e,\lambda,nf} = K_{a,\lambda,bf} + K_{e,\lambda,np} \tag{A11}$$

B: Mathematical modeling of effective optical parameters

Effective emissivity: Effective emissivity [mathematically defined by Eq. (B1)] is the measure of emission from a surface relative to a corresponding black body at same temperature. It is a material property and a function of temperature. Figure B1 shows the effective emissivity values as a function of temperature for glass, heat mirror and solar selective surface.

$$\varepsilon_{eff} = \frac{\int_{0.3\mu m}^{30\mu m} (1-\rho_\lambda-\tau_\lambda) e_{b,T,\lambda} d\lambda}{\int_{0.3\mu m}^{30\mu m} e_{b,T,\lambda} d\lambda} = \frac{\sum_{0.3\mu m}^{30\mu m} (1-\rho_\lambda-\tau_\lambda) e_{b,T,\lambda} d\lambda}{\sum_{0.3\mu m}^{30\mu m} e_{b,T,\lambda} d\lambda} = \frac{\sum_{\lambda=0.3\mu m}^{\lambda=30\mu m} \varepsilon_{\lambda,T} e_{b,\lambda,T} d\lambda}{\sum_{\lambda=0.3\mu m}^{\lambda=30\mu m} e_{b,\lambda,T} d\lambda} \quad \text{(B1)}$$

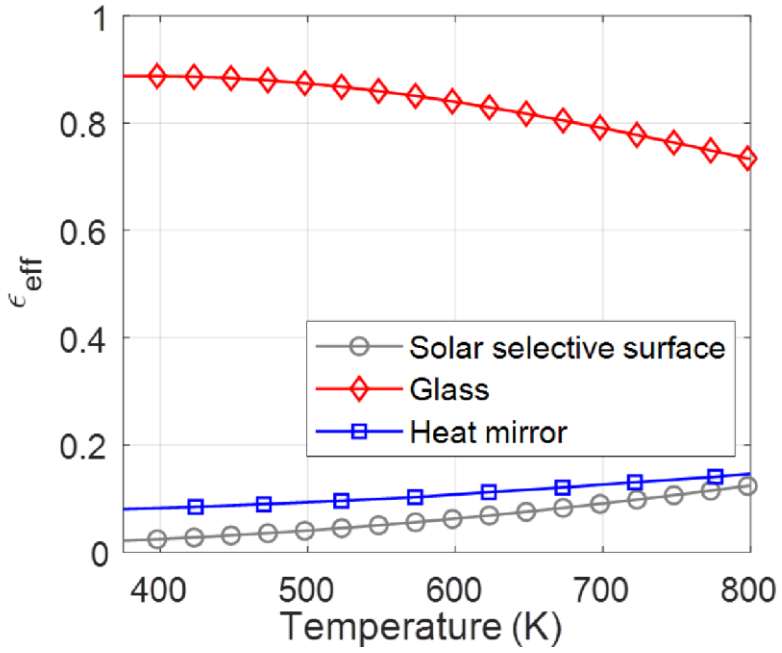

Fig. B1: Effective emissivity as a function of temperature for various optical elements, viz., solar selective surface, glass, and heat mirror.

Effective absorptivity, reflectivity, and transmissivity: Parameters viz., effective absorptivity [defined by Eqs. (B2) and (B3)]), reflectivity [defined by Eqs.(B4) and (B5)], and transmissivity [defined by Eqs.(B6) and (B7)] depend on the material as well as the irradiation spectra. Since the

magnitude and spectra of the radiation falling on any of the plates varies with each reflection, the values of effective absorptivity, reflectivity and transmissivity keep on changing as well.

$$\alpha_{1j,eff} = \frac{\sum_{\lambda=0.3\mu m}^{\lambda=30\mu m} \varepsilon_{\lambda,1} e_{b,\lambda,T1} \rho_{\lambda,2}^{j} \rho_{\lambda,1}^{j-1} \alpha_{\lambda,1} d\lambda}{\sum_{\lambda=0.3\mu m}^{\lambda=30\mu m} \varepsilon_{\lambda,1} e_{b,\lambda,T1} \rho_{\lambda,2}^{j} \rho_{\lambda,1}^{j-1} d\lambda}, \quad \alpha_{2j,eff} = \frac{\sum_{\lambda=0.3\mu m}^{\lambda=30\mu m} \varepsilon_{\lambda,1} e_{b,\lambda,T1} \rho_{\lambda,1}^{j-1} \rho_{\lambda,2}^{j-1} \alpha_{\lambda,2} d\lambda}{\sum_{\lambda=0.3\mu m}^{\lambda=30\mu m} \varepsilon_{\lambda,1} e_{b,\lambda,T1} \rho_{\lambda,1}^{j-1} \rho_{\lambda,2}^{j-1} d\lambda} \qquad \text{(B2)}$$

where $\alpha_{1j,eff}$ is the effective absorptivity of plate 1 for the irradiation spectrum initially emitted by the plate itself (plate 1). Number of reflections dictates the value of effective absorptivity. For instance, at a given temperature, the initially emitted spectrum of plate 1 reaches plate 2, and a portion of this is reflected depending on the spectral reflectivity of plate 2. Subsequently, this modified spectrum reaches plate 1 again; here again a part of this modified spectrum is absorbed by the plate 1 and rest is reflected to plate 2 (depending on the spectral absorptivity and reflectivity values of plate 1). This process goes on till the strength of radiation eventually becomes negligible. Thus, the effective values of effective absorptivity change with each reflection. With reference to Fig. 5, the values of effective absorptivity at points i_1, j_1 and k_1 (and so on) will each be different as the radiation emitted by plate 1 has undergone different number of reflections in each case [subscript and superscript j (= 1, 2, 3....∞) in Eq. (B2) denotes the number of reflections]. Essentially, these points (i_1, j_1 and k_1) represent the absorptivity values after subsequent reflections. Likewise, $\alpha_{2j,eff}$ is the effective absorptivity of plate 2 for the irradiation spectrum initially emitted by plate 1.

On similar lines, $\alpha'_{1j,eff}$ and $\alpha'_{2j,eff}$ are the effective absorptivities of plates 1 and 2 for the irradiation spectrum initially emitted by plate 2.

$$\alpha'_{1j,eff} = \frac{\sum_{\lambda=0.3\mu m}^{\lambda=30\mu m} \varepsilon_{\lambda,2} e_{b,\lambda,T2} \rho_{\lambda,2}^{j-1} \rho_{\lambda,1}^{j-1} \alpha_{\lambda,1} d\lambda}{\sum_{\lambda=0.3\mu m}^{\lambda=30\mu m} \varepsilon_{\lambda,2} e_{b,\lambda,T2} \rho_{\lambda,2}^{j-1} \rho_{\lambda,1}^{j-1} d\lambda}, \quad \alpha'_{2j,eff} = \frac{\sum_{\lambda=0.3\mu m}^{\lambda=30\mu m} \varepsilon_{\lambda,2} e_{b,\lambda,T2} \rho_{\lambda,1}^{j} \rho_{\lambda,2}^{j-1} \alpha_{\lambda,2} d\lambda}{\sum_{\lambda=0.3\mu m}^{\lambda=30\mu m} \varepsilon_{\lambda,2} e_{b,\lambda,T2} \rho_{\lambda,1}^{j} \rho_{\lambda,2}^{j-1} d\lambda} \qquad \text{(B3)}$$

In a similar manner, the effective reflectivity and transmissivity values can be obtained from the equations below.

$$\rho_{1j,eff} = \frac{\sum_{\lambda=0.3\mu m}^{\lambda=30\mu m} \varepsilon_{\lambda,1} e_{b,\lambda,T1} \rho_{\lambda,2}^{j} \rho_{\lambda,1}^{j} d\lambda}{\sum_{\lambda=0.3\mu m}^{\lambda=30\mu m} \varepsilon_{\lambda,1} e_{b,\lambda,T1} \rho_{\lambda,2}^{j} \rho_{\lambda,1}^{j-1} d\lambda}, \quad \rho_{2j,eff} = \frac{\sum_{\lambda=0.3\mu m}^{\lambda=30\mu m} \varepsilon_{\lambda,1} e_{b,\lambda,T1} \rho_{\lambda,2}^{j} \rho_{\lambda,1}^{j-1} d\lambda}{\sum_{\lambda=0.3\mu m}^{\lambda=30\mu m} \varepsilon_{\lambda,1} e_{b,\lambda,T1} \rho_{\lambda,2}^{j-1} \rho_{\lambda,1}^{j-1} d\lambda} \tag{B4}$$

where $\rho_{1j,eff}$ and $\rho_{2j,eff}$ are the effective reflectivities of plates 1 and 2 for the irradiation spectrum initially emitted by plate 1.

$$\rho'_{1j,eff} = \frac{\sum_{\lambda=0.3\mu m}^{\lambda=30\mu m} \varepsilon_{\lambda,2} e_{b,\lambda,T2} \rho_{\lambda,2}^{j-1} \rho_{\lambda,1}^{j} d\lambda}{\sum_{\lambda=0.3\mu m}^{\lambda=30\mu m} \varepsilon_{\lambda,2} e_{b,\lambda,T2} \rho_{\lambda,2}^{j-1} \rho_{\lambda,1}^{j-1} d\lambda}, \quad \rho'_{2j,eff} = \frac{\sum_{\lambda=0.3\mu m}^{\lambda=30\mu m} \varepsilon_{\lambda,2} e_{b,\lambda,T2} \rho_{\lambda,2}^{j} \rho_{\lambda,1}^{j} d\lambda}{\sum_{\lambda=0.3\mu m}^{\lambda=30\mu m} \varepsilon_{\lambda,2} e_{b,\lambda,T2} \rho_{\lambda,2}^{j-1} \rho_{\lambda,1}^{j} d\lambda} \tag{B5}$$

where $\rho'_{1j,eff}$ and $\rho'_{2j,eff}$ are the effective reflectivities of plates 1 and 2 for the irradiation spectrum initially emitted by plate 2.

$$\tau_{1j,eff} = \frac{\sum_{\lambda=0.3\mu m}^{\lambda=30\mu m} \varepsilon_{\lambda,1} e_{b,\lambda,T1} \rho_{\lambda,2}^{j} \rho_{\lambda,1}^{j-1} \tau_{\lambda,1} d\lambda}{\sum_{\lambda=0.3\mu m}^{\lambda=30\mu m} \varepsilon_{\lambda,1} e_{b,\lambda,T1} \rho_{\lambda,2}^{j} \rho_{\lambda,1}^{j-1} d\lambda}, \quad \tau_{2j,eff} = \frac{\sum_{\lambda=0.3\mu m}^{\lambda=30\mu m} \varepsilon_{\lambda,1} e_{b,\lambda,T1} \rho_{\lambda,1}^{j-1} \rho_{\lambda,2}^{j-1} \tau_{\lambda,2} d\lambda}{\sum_{\lambda=0.3\mu m}^{\lambda=30\mu m} \varepsilon_{\lambda,1} e_{b,\lambda,T1} \rho_{\lambda,1}^{j-1} \rho_{\lambda,2}^{j-1} d\lambda} \tag{B6}$$

where $\tau_{1j,eff}$ and $\tau_{2j,eff}$ are the effective transmissivities of plates 1 and 2 for the irradiation spectrum initially emitted by plate 1.

$$\tau'_{1j,eff} = \frac{\sum_{\lambda=0.3\mu m}^{\lambda=30\mu m} \varepsilon_{\lambda,2} e_{b,\lambda,T2} \rho_{\lambda,2}^{j-1} \rho_{\lambda,1}^{j-1} \tau_{\lambda,1} d\lambda}{\sum_{\lambda=0.3\mu m}^{\lambda=30\mu m} \varepsilon_{\lambda,2} e_{b,\lambda,T2} \rho_{\lambda,2}^{j-1} \rho_{\lambda,1}^{j-1} d\lambda}, \quad \tau'_{2j,eff} = \frac{\sum_{\lambda=0.3\mu m}^{\lambda=30\mu m} \varepsilon_{\lambda,2} e_{b,\lambda,T2} \rho_{\lambda,1}^{j} \rho_{\lambda,2}^{j-1} \tau_{\lambda,2} d\lambda}{\sum_{\lambda=0.3\mu m}^{\lambda=30\mu m} \varepsilon_{\lambda,2} e_{b,\lambda,T2} \rho_{\lambda,1}^{j} \rho_{\lambda,2}^{j-1} d\lambda} \tag{B7}$$

where $\tau'_{1j,eff}$ and $\tau'_{2j,eff}$ are the effective transmissivities of plates 1 and 2 for the irradiation spectrum initially emitted by plate 2.

Also, Eq. (B8) gives the effective absorptivity of atmosphere:

$$\alpha_{atm,eff} = \frac{\sum_{\lambda=0.3\mu m}^{\lambda=30\mu m} \alpha_{2,\lambda,T_{amb}} e_{b,\lambda,T_{amb}} d\lambda}{\sum_{\lambda=0.3\mu m}^{\lambda=30\mu m} e_{b,\lambda,T_{amb}} d\lambda} \tag{B8}$$

C: Numerical modeling

Plate 1 (solar selective/black/glass) and the fluid (basefluid/nanofluid) have been discretized into finite control volumes. Explicit form of finite difference technique has been employed to convert the integro-differential equations into set of algebraic equations – characteristic algebraic equations for interior and boundary nodes. Figure C1 show the discretization strategy followed for numerical modeling VARs in particular. RTE is essentially solved in *y*-*z* plane; whereas, the overall energy balance equation is solved in *x*-*y* plane until steady state is reached.

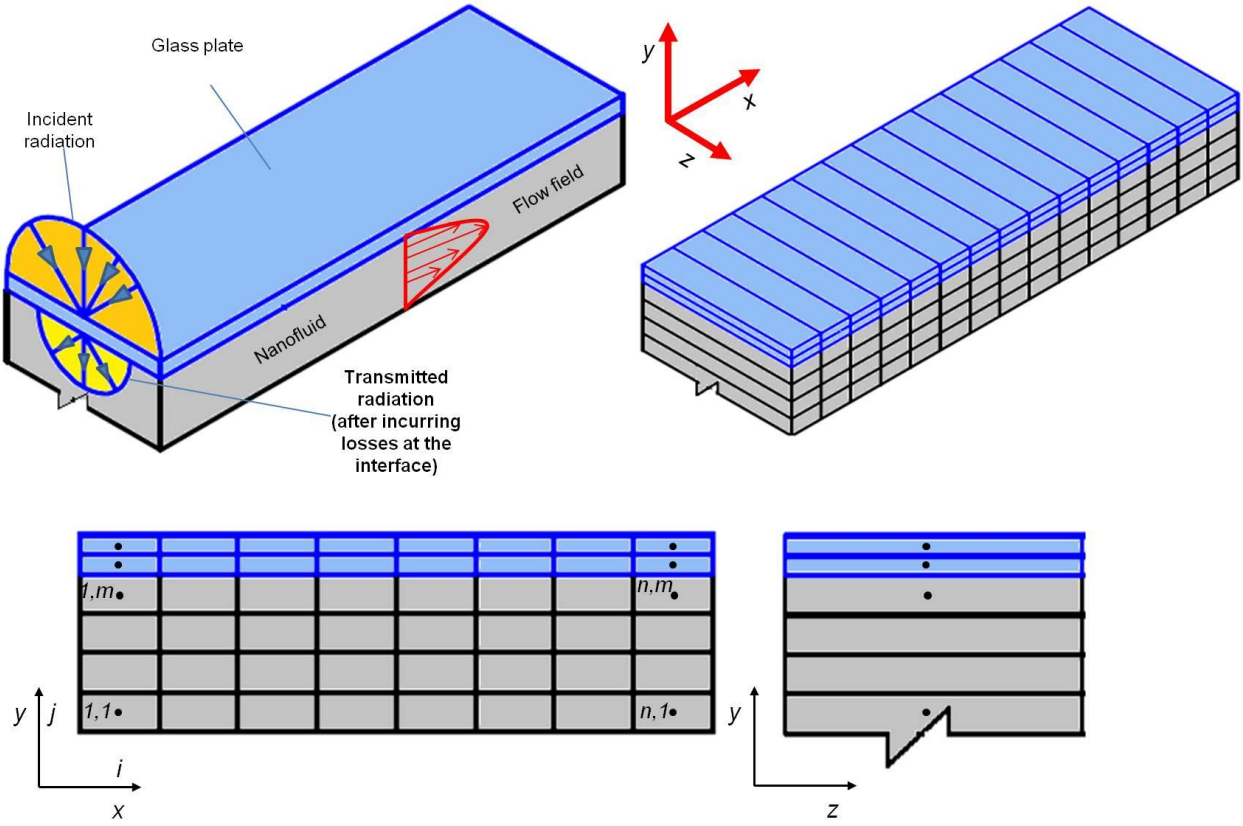

Fig. C1: Discretization strategy for numerical modeling of volumetric receivers.

Further, It may be noted that grid independence test was carried out and it was found that the results were nearly independent of grid size beyond 49×700 (see Fig. C2).

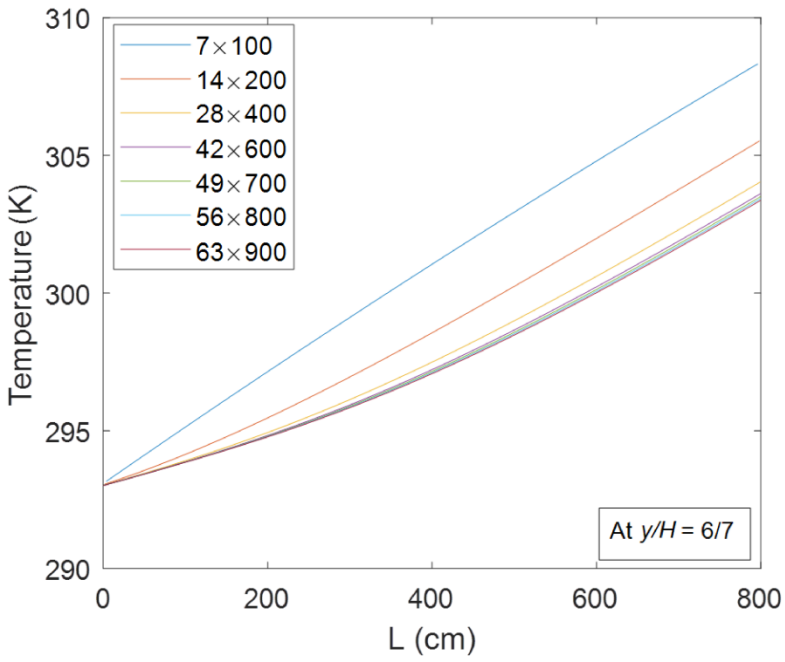

Fig. C2: Spatial temperature distribution along the conduit length at $y/H = 6/7$ for various grid sizes.

D: Solution of the radiative transfer equation (RTE) used in forced convection in channels

Figure C1 shows the *y-z* plane of the conduit. The nanofluid is bounded by glass and reflective plates at the top and bottom, respectively. To find the values of radiation intensity in positive and negative directions at various points along the depth of the channel the RTE has been solved numerically. Once intensity at different depths in different directions (+ve and -ve) is known, the 'divergence' which is the net radiative energy per unit time and volume leaving a differential control volume into which the channel depth has been subdivided can be found.

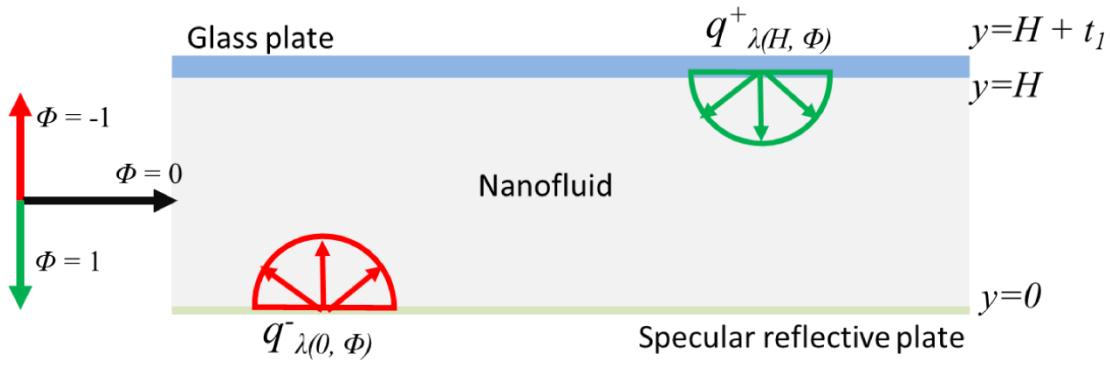

Fig. D1: Schematic showing the y-z plane defining the +ve and -ve directions of Φ and the heat flux.

From the boundary conditions Eqs. (D1) and (D2) are obtained:

$$I^{+}_{\lambda(H,\phi)} = S_{\lambda 1}.\tau_{\lambda 1} + \rho_{\lambda 1}.I^{-}_{\lambda(H,-\phi)} + \alpha_{\lambda 1}.I_{b\lambda[y=H]} \tag{D1}$$

$$I^{-}_{\lambda(0,\phi)} = \rho_{\lambda 3}.I^{+}_{\lambda(0,+\phi)} \tag{D2}$$

Two more equations are obtained from the equation of radiative transfer for an absorbing, emitting scattering medium (only includes out-scattering contribution) [Eqs. (D3) and (D4)].

$$I^{-}_{\lambda(H,\phi)} = I^{-}_{\lambda(0,\phi)} \exp\left[\frac{\theta_H}{\phi}\right] - \int_0^{\theta_H} \frac{I_{b(\theta')}}{\phi} e^{\left(\frac{\theta_H}{\phi}\right)} d\theta' \tag{D3}$$

$$I^{+}_{\lambda(0,\phi)} = I^{+}_{\lambda(H,\phi)} \exp\left[-\frac{\theta_H}{\phi}\right] + \int_{\theta_H}^{0} \frac{I_{b(\theta')}}{\phi} e^{\left(\frac{\theta'-\theta_H}{\phi}\right)} d\theta' \tag{D4}$$

In each of the above equations (Eqs. (D4) and (D5]); the first term on the RHS gives intensity of radiation after attenuation and the second term is the contribution of emission from medium to radiation at any point.

Radiation travelling from the top cover to the bottom is regarded as +ve and vice versa.

Solving Eqs. (D1) - (D4), Eqs. D5 and D6 are obtained:

$$I^{+}_{\lambda(H,\phi)} = \frac{S_{\lambda 1}.\tau_{\lambda 1} + \alpha_{\lambda 1}.I_{b\lambda T_{[y=H]}} + \rho_{\lambda 1}.\rho_{\lambda 3}.\exp\left[\frac{-\theta_H}{\phi}\right].\int_{\theta_H}^{0} \frac{I_{b\lambda(\theta')}}{\phi}.\mathrm{e}^{\left(\frac{-\theta'}{\phi}\right)} d\theta' + \rho_{\lambda 1}.\int_{0}^{\theta_H} \frac{I_{b\lambda(\theta')}}{\phi}.\mathrm{e}^{\left(\frac{\theta_H-\theta'}{\phi}\right)} d\theta'}{\left(1-\rho_{\lambda 1}.\rho_{\lambda 3}.\exp\left[\frac{-2\theta_H}{\phi}\right]\right)} \tag{D5}$$

$for\ \phi > 0$

$$I^{-}_{\lambda(0,\phi)} = \frac{\rho_{\lambda 3}.S_{\lambda 1}.\tau_{\lambda 1}.\exp\left[\frac{\theta_H}{\phi}\right] + \alpha_{\lambda 1}.\rho_{\lambda 3}.I_{b\lambda[y=H]}.\exp\left[\frac{\theta_H}{\phi}\right] - \rho_{\lambda 1}.\rho_{\lambda 3}.\exp\left[\frac{\theta_H}{\phi}\right].\int_{\theta_H}^{0} \frac{I_{b\lambda(\theta')}}{\phi}.\mathrm{e}^{\left(\frac{\theta'}{\phi}\right)} d\theta' - \rho_{\lambda 3}.\int_{0}^{\theta_H} \frac{I_{b\lambda(\theta')}}{\phi}.\mathrm{e}^{\left(\frac{\theta_H-\theta'}{\phi}\right)} d\theta'}{\left(1-\rho_{\lambda 1}.\rho_{\lambda 3}.\exp\left[\frac{2\theta_H}{\phi}\right]\right)}$$

$for\ \phi < 0$

(D6)

The hemispherical flux at any location is obtained by integrating the intensity field.

$$q^{+}_{\lambda} = 2\pi \int_{0}^{1} I^{+}_{\lambda} \phi d\phi$$
$$q^{-}_{\lambda} = 2\pi \int_{-1}^{0} I^{-}_{\lambda} \phi d\phi \tag{D7}$$

Once the values of intensity at the boundaries are calculated, one can use Eq. (D8) to find the intensity and thus hemispherical flux at any point in between the two plates.

$$I_{\lambda}^{+}(\theta) = I_{1\lambda}^{+} \exp\left(\frac{-\theta}{\phi}\right) + \int_{0}^{t} I_{b\lambda}(\theta').\exp\left(\frac{\theta'-\theta}{\phi}\right)\frac{d\theta'}{\phi} \quad \text{(D8)}$$

The hemispherical flux at any point (in both positive and negative directions) between the two plates (plate 1 and plate 2) is obtained by integrating the intensity field from Eq. (D8). The conduit is divided into finite volume elements. Flux coming in and out of the volume element at the top and bottom of the volume element is found using the method described above.

The sum of positive flux at the top of the volume element and negative flux at the bottom of the volume element gives $q_{net,in}$ which is the net flux going into the element. Similarly, sum of negative flux at the top of the volume element and positive flux at the bottom of the element gives the net flux going out of the element ($q_{net,out.}$).

The spectral intensity of radiation emitted locally inside a medium is given by Eq. (D9):

$$I_{b,\lambda} = \frac{C_1 n^3}{\lambda^5\left(e^{C_2/\lambda T} - 1\right)} \quad \text{(D9)}$$

where, C_1=3.74177×10^8 and C_2=3.74177×10^8, *'n'* is the refractive index, *'λ'* is wavelength and *'T'* is for temperature (Howell).

The divergence for any generic volume element is given by Eq. (D10) as

$$q_{rad,nf} = q_{net,out} - q_{net,in} \quad \text{(D10)}$$

The divergence thus calculated can be included in the energy equation to find the temperature distribution within the nanofluid.

E: Validation of numerical models used in the study of forced convection

RTE model validation

Two infinite black walls at a distance 'H' are considered. The known conditions are the temperatures (T_1 and T_2) and emissivities (ε_1= ε_2=1) of the two walls, and the absorption coefficients (K_a) of the intervening medium. The non-dimensional blackbody flux at any optical thickness 't' (where $t = K_a\, y$, y being the distance from wall 1) is given by Eq. (E1) as

$$e_b^*(t) = \frac{e_b(t) - e_{b2}}{e_{b1} - e_{b2}} \tag{E1}$$

The value of e_b^* at the temperature of wall 1 is $e_b^*(T_1)$ =1 and the value of e_b^* at the temperature of wall 2 is $e_b^*(T_2)$ = 0. Figure E1 shows the comparison between present developed model and that in (Heaslet & Warming, 1965); clearly the two closely match for various values of absorption coefficients.

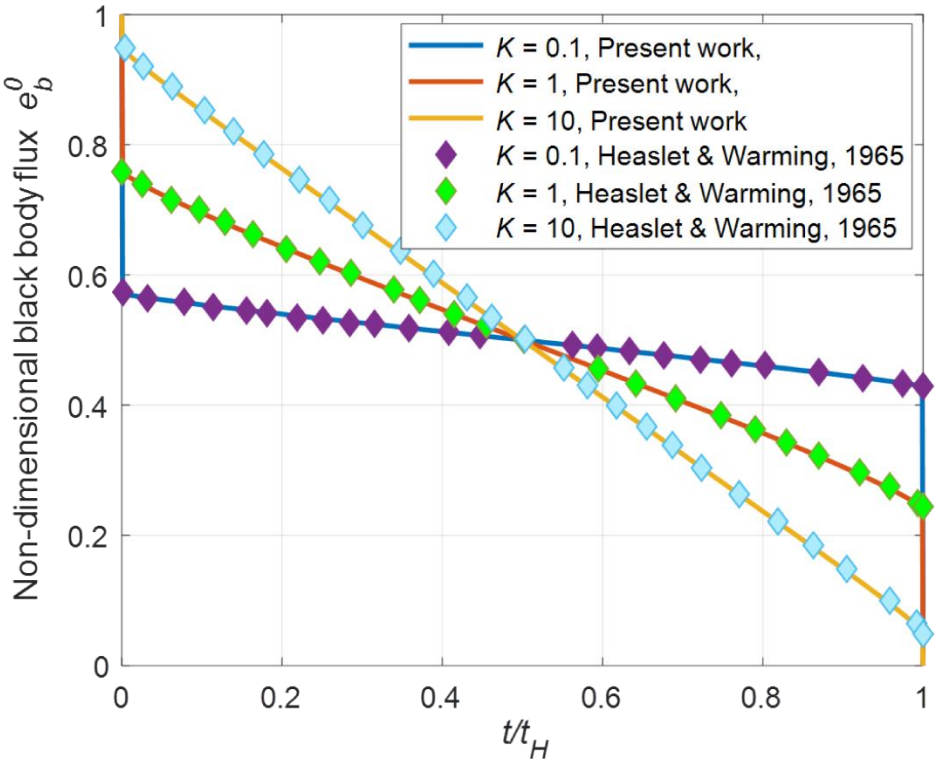

Fig. E1: Comparison of non-dimensional temperature profile for a gray slab in radiative equilibrium for different values of optical thickness with the results of (Heaslet & Warming, 1965).

Validation of numerical model for surface absorption-based receivers

To validate the numerical model developed for surface absorption-based receivers, the obtained results were compared with those obtained from ANSYS®. A channel length of 4 meters and width of 5cm has been considered with a black surface at the top (exposed to ambient conditions, i.e., no enveloping cover). Solar radiation (5000Wm^{-2}) falls on the top surface of the channel, absorbing all radiation and heating up, thus in turn heating the fluid flowing through the channel. The initial temperature of the fluid and the ambient temperatures are both assumed to be 293K.

The average velocity is adjusted such that the global Peclet number [defined by Eq.(E2)] is equal to 20000 (~Re = 5).

$$Pe = \frac{Du_{avg}H}{a} \tag{E2}$$

where 'a' is thermal diffusivity.

The flow is assumed to be laminar and fully developed [described by Eq. (E3)], such that,

$$u(y) = u_{in}(y) = 6u_{avg}\left[\left(\frac{y}{H}\right) - \left(\frac{y}{H}\right)^2\right] \tag{E3}$$

Temperature distribution was obtained for both cases. Figure E2 shows a comparison of temperature distribution of both cases along the channel length at various channel heights. Both the results are in agreement with each other thus validating the numerical approach for finding the temperature distribution in a surface absorption-based receiver.

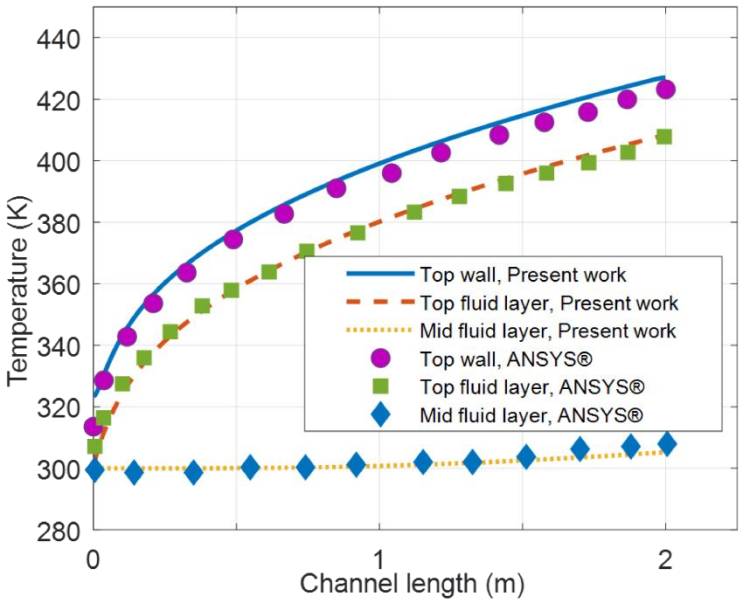

Fig. E2: Comparison of temperature distribution at different channel heights as obtained from the developed numerical model and those obtained from *ANSYS® Academic Research Mechanical, Release 18.1.*

F: Validation of numerical models used in the study of natural convection

To validate the mathematical model, the simulation was carried out for semi-transparent fluids filled in a two-dimensional cavity heated volumetrically through radiation incident from the side and the results were compared with those of Webb & Viskanta, 1987. Fig. F1(a) presents the schematic of the study by Webb. Radiation is incident normally on the transmitting wall on the left, the right wall is assumed isothermal. The top and bottom walls are adiabatic. The other parameters are as follows: $Ra = 10^6$, $Pr = 6$, $AR = 2$, $Bi^* = 0$.

Fig. F1(b) shows the dimensionless temperature (T^*) at midline ($Y = 1$) along the width of cavity (X) for different values of optical thickness of the fluid ($E = 0.1$, $E = 1$, $E = 10$). As can be seen, the results obtained from the present model are in very good agreement with the ones obtained by Webb thus validating the present model.

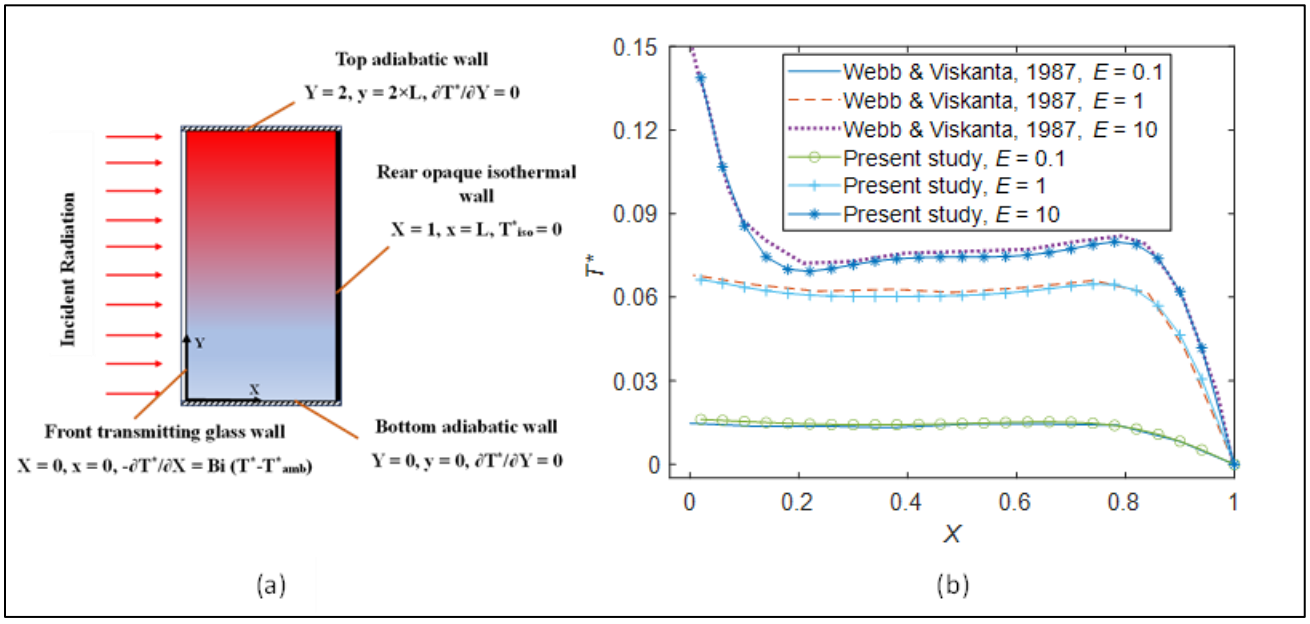

Fig. F1: (a) Schematic showing the configuration studied by Webb and Viskanta, 1987, and (b) comparison of results obtained from the present developed model with that reported by Webb and Viskanta, 1987.

G: Grid independence test used in the study of natural convection in cavities

(a). Cavity heated from side

A grid independence test was carried out to assess the optimal resolution of the grid. The mesh size was changed beginning from a coarse one to a finer one till the results did not change significantly on account of grid size. The grid independence test was performed with grid sizes 20×20, 30×30, 40×40, 50×50 and 60×60. The graph below (Figure G1) shows the mid-line temperature at X=0.5 for the different grid sizes for the base case (Ra=10^8, Pr=10 and E=2). Grid size 50×50 was selected for the generation of results for this study as optimum results are obtained with sufficient accuracy and reasonable computational time.

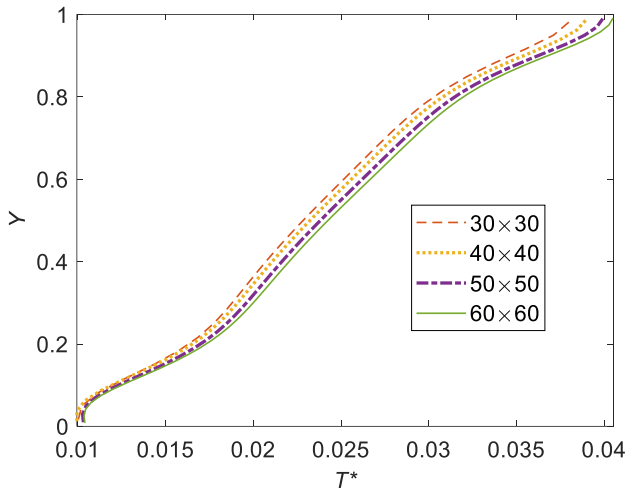

Fig. G1: Grid independence test at different grid sizes for cavity heated from side.

(b). Cavity heated from bottom

A grid independence test was carried out prior to running the codes for the base case taken in the study to assess the optimal resolution of the grid. The mesh size was changed beginning from a coarse grid to a finer one till the results did not change significantly on account of grid size. The grid independence test was performed with grid sizes 20×20, 30×30, 40×40, 50×50 and 60×60. The graph below (Fig. G2) shows the mid-line temperature at X=0.5 for the different grid sizes for the base case (Ra=10^5, Pr=10 and E=2). It is seen that the difference is inconspicuous at grid sizes 50 and 60. Grid size 50×50 was selected for the generation of results for this study.

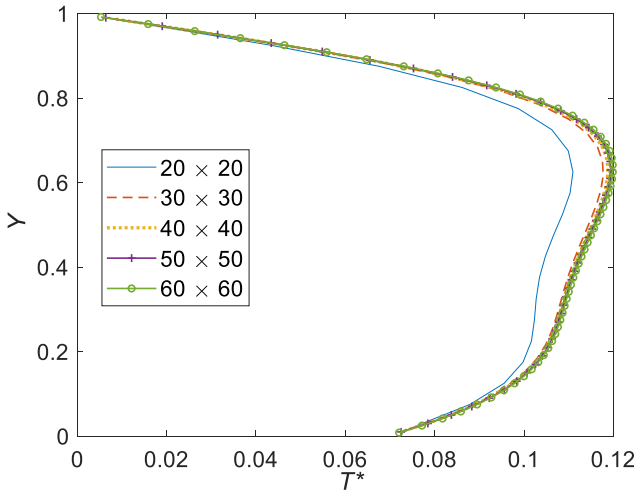

Fig. G2: Grid Independence test at different grid sizes for cavity heated from bottom.

Nomenclature and Glossary

English Symbols:

A	Area
a	Thermal diffusivity [m^2s^{-1}]
AR	aspect ratio
B	coefficient of volumetric expansion [K^{-1}]
Bi^*	modified Biot number [$= hL/k_g$]
c_p	specific heat [J kg^{-1} K^{-1}]
D	density [kgm^{-3}]
d	characteristic dimension for nanoparticles [= 30nm]
E	optical thickness[$=K \times L$]
e_b	black body flux [Wm^{-2}]
F	flux at specific x- co-ordinate [$=G_0 e^{-Kx}$]
f_v	volume fraction of nanoparticles
G_0	flux incident at glass wall [Wm^{-2}]
g	gravitational acceleration [ms^{-2}]
H	height of conduit [= 0.07m]
$\mathscr{H}$	heat function [W-m]
h	convection heat transfer coefficient [W/m^2K]
I_o	initial intensity of radiation [$Wm^{-2}sr^{-1}$]
I	intensity of radiation after travelling a distance 's' [$Wm^{-2}sr^{-1}$]
J	input variables
K	coefficient of absorption or extinction
k	thermal conductivity [W m^{-1} K^{-1}]
L	Length of the channel [=8m] (forced convection)/ cavity (natural convection)
m	normalized refractive index
n	refractive index

O output variables

p pressure [Nm^{-2}]

P dimensionless pressure [$=pL^2/\rho_0\alpha_l^2$]

Pe Peclet number

Pr Prandtl Number [$=\upsilon/a$]

q^* dimensionless flux at isothermal wall

Q^* dimensionless cumulative flux at isothermal wall

Q_e extinction efficiency

q heat flux [Wm^{-2}]

Re Reynolds Number

Ra^* modified Rayleigh number [$=L^4 g\beta G_0/\upsilon\ \alpha_l\ k$]

S solar irradiance [Wm^{-2}]

s distance travelled by radiation [m]

T temperature [K]

T_0 ambient temperature [K]

T^* dimensionless temperature[$=(T-T_0)\ k_f/F_0\ L$]

t time [s]

t^* dimensionless time [$=ta_l/L^2$]

t_1 thickness of the top plate of the channel [= 0.02m]

u velocity in x-direction [ms^{-1}]

U dimensionless velocity in X-direction [$=uL/\alpha_l$]

v velocity in y-direction [ms^{-1}]

V dimensionless velocity in Y-direction [$=vL/\alpha_l$]

x x co-ordinate [m]

X dimensionless x co-ordinate [$=x/L$]

y y co-ordinate [m]

Y dimensionless y co-ordinate [$=y/L$]

Greek Symbols:

α absorptivity

β size parameter

δ half-angle subtended by sun

ε emissivity

$\boldsymbol{\xi}$ energy

η efficiency

θ optical depth

κ optical constant

λ wavelength

μ dynamic viscosity [kg m^{-1} s^{-1}]

υ kinematic viscosity [m^2s^{-1}]

ϕ cosine of direction in which radiation is travelling

ρ reflectivity

σ Stefan-Boltzmann constant [$= 5.67 \times 10^{-8}$ $Wm^{-2}K^{-4}$]

τ transmissivity

ψ angle of incidence/ stream function [m^2s^{-1}]

Subscript:

a absorption

amb ambient

avg average

b black body

bf basefluid

carn Carnot

cm comprehensive model

e extinction

eff effective

ex exit

f basefluid

g glass

in inlet temperature

l liquid

loss loss

max maximum value

nf nanofluid

np nanoparticles

over overall

rec receiver

sc scattering

sm simplified model

sw solar weighted

vac vacuum

y position along conduit depth

1 top plate of the conduit (plate 1)

2 cover plate (plate 2)

3 bottom plate of the conduit (plate 3)

λ spectral

$\perp$ perpendicular

$\parallel$ parallel

II second law

Superscript:

j number of reflections

+ direction of propagation from top to bottom

- direction of propagation from bottom to top

Abbreviations and acronyms:

DASC	Direct absorption solar collector
SAR	Surface absorption-based receiver
VAR	Volumetric absorption-based receiver
BS-HM	Black surface-heat mirror receiver design
G-G	Glass-glass receiver design
G-HM	Glass-heat mirror receiver design
SSS-ATM	Solar selective surface-atmosphere receiver design
SSS-G	Solar selective surface-glass receiver design

References

[1]. Amber, Ityona, and T. S. O'Donovan. "Heat transfer in a molten salt filled enclosure absorbing concentrated solar radiation." *International Journal of Heat and Mass Transfer* 113 (2017): 444-455.

[2]. Amber, Ityona, and T. S. O'Donovan. "Natural convection induced by the absorption of solar radiation: A review." *Renewable and Sustainable Energy Reviews* 82 (2018): 3526-3545.

[3]. Azad, F. H., and M. F. Modest. "Evaluation of the radiative heat flux in absorbing, emitting and linear-anisotropically scattering cylindrical media." (1981): 350-356.

[4]. Bednarz, Tomasz P., Chengwang Lei, and John C. Patterson. "Unsteady natural convection induced by diurnal temperature changes in a reservoir with slowly varying bottom topography." *International Journal of Thermal Sciences* 48, no. 10 (2009): 1932-1942.

[5]. Bejan, Adrian. *Convection heat transfer*. John wiley & sons, 2013.

[6]. Bonab, H.B. and Javani, N., 2019. Investigation and optimization of solar volumetric absorption systems using nanoparticles. *Solar Energy Materials and Solar Cells*, *194*, pp.229-234.

[7]. Choi, Tae Jong, Seok Pil Jang, and M. A. Kedzierski. "Effect of surfactants on the stability and solar thermal absorption characteristics of water-based nanofluids with multi-walled carbon nanotubes." *International Journal of Heat and Mass Transfer* 122 (2018): 483-490.

[8]. Coates, Michael J., and John C. Patterson. "Unsteady natural convection in a cavity with non-uniform absorption of radiation." *Journal of Fluid Mechanics* 256 (1993): 133-161.

[9]. Cregan, V. and Myers, T.G., 2015. Modelling the efficiency of a nanofluid direct absorption solar collector. *International Journal of Heat and Mass Transfer*, *90*, pp.505-514.

[10]. Duffie, J.A. and Beckman, W.A., 2013. *Solar engineering of thermal processes*. John Wiley & Sons.

[11]. Dutta, Pradip. "High temperature solar receiver and thermal storage systems." *Applied thermal engineering* 124 (2017): 624-632.

[12]. Ebrahimnia-Bajestan, E., Moghadam, M.C., Niazmand, H., Daungthongsuk, W. and Wongwises, S., 2016. Experimental and numerical investigation of nanofluids heat transfer characteristics for application in solar heat exchangers. *International Journal of Heat and Mass Transfer*, *92*, pp.1041-1052.

[13]. Fan, M., Liang, H., You, S., Zhang, H., Zheng, W. and Xia, J., 2018. Heat transfer analysis of a new volumetric based receiver for parabolic trough solar collector. *Energy*, *142*, pp.920-931.

[14]. Farrow, D. E., and J. C. Patterson. "On the response of a reservoir sidearm to diurnal heating and cooling." *Journal of Fluid Mechanics* 246 (1993): 143-161.

[15]. Farrow, D. E., and J. C. Patterson. "The daytime circulation and temperature structure in a reservoir sidearm." *International Journal of Heat and Mass Transfer* 37, no. 13 (1994): 1957-1968.

[16]. Freedman, Justin P., Hao Wang, and Ravi S. Prasher. "Analysis of nanofluid-based parabolic trough collectors for solar thermal applications." *Journal of Solar Energy Engineering* 140, no. 5 (2018).

[17]. Gorji, T.B. and Ranjbar, A.A., 2016. A numerical and experimental investigation on the performance of a low-flux direct absorption solar collector (DASC) using graphite, magnetite and silver nanofluids. *Solar Energy*, *135*, pp.493-505.

[18]. Hattori, T., J. C. Patterson, and C. Lei. "Study of unsteady natural convection induced by absorption of radiation based on a three-waveband attenuation model." In *Journal of Physics: Conference Series*, vol. 530, no. 1, p. 012036. IOP Publishing, 2014.

[19]. Hattori, Tae, John C. Patterson, and Chengwang Lei. "Mixing in internally heated natural convection flow and scaling for a quasi-steady boundary layer." *Journal of Fluid Mechanics* 763 (2015a): 352-368.

[20]. Hattori, T., J. C. Patterson, and C. Lei. "Scaling and direct stability analyses of natural convection induced by absorption of solar radiation in a parallelepiped cavity." *International Journal of Thermal Sciences* 88 (2015b): 19-32.

[21]. Hazra, S. K., M. Michael, and T. K. Nandi. "Investigations on optical and photo-thermal conversion characteristics of BN-EG and BN/CB-EG hybrid nanofluids for applications in direct absorption solar collectors." *Solar Energy Materials and Solar Cells* 230 (2021): 111245.

[22]. Heaslet, M.A. and Warming, R.F., 1965. Radiative transport and wall temperature slip in an absorbing planar medium. *International Journal of Heat and Mass Transfer*, *8*(7), pp.979-994.

[23]. Heaslet, Max A., and Robert F. Warming. "Theoretical predictions of radiative transfer in a homogenous cylindrical medium." *Journal of Quantitative Spectroscopy and Radiative Transfer* 6.6 (1966): 751-774.

[24]. Hewakuruppu, Y.L., Taylor, R.A., Tyagi, H., Khullar, V., Otanicar, T., Coulombe, S. and Hordy, N., 2015. Limits of selectivity of direct volumetric solar absorption. *Solar Energy*, *114*, pp.206-216.

[25]. Hewakuruppu, Y. L., 2016. *Investigating the potential of developing a selective nanofluid-based direct absorption solar collector* (Doctoral dissertation, UNSW).

[26]. IEA, 2013. Electricity generation by source, World 1990-2017, Electricity Information. https://webstore.iea.org/electricity-information-2019 (accessed on11th November 2019).

[27]. IEA, 2019. Total primary energy supply (TPES) by source, World 1990-2017, World Energy Balances. https://www.iea.org/statistics/ (accessed on11th November 2019).

[28]. IPCC, 2023: *Climate Change 2023: Synthesis Report.* A Report of the Intergovernmental Panel on Climate Change. Contribution of Working Groups I, II and III to the Sixth Assessment Report of the Intergovernmental Panel on Climate Change [Core Writing Team, H. Lee and J. Romero (eds.)]. IPCC, Geneva, Switzerland, (in press).

[29]. Jain, Shubham, et al. "Thermal energy storage for solar energy." *Fundamentals and Innovations in Solar Energy* (2021): 167-215.

[30]. Kefayati, Gholamreza. "Internally heated convection of viscoplastic fluids in enclosures using a lattice Boltzmann method." *Physics of Fluids* 35, no. 1 (2023): 013108.

[31]. Khullar, V., Tyagi, H., Phelan, P.E., Otanicar, T.P., Singh, H. and Taylor, R.A., 2012. Solar energy harvesting using nanofluids-based concentrating solar collector. *Journal of Nanotechnology in Engineering and Medicine*, *3*(3), p.031003.

[32]. Khullar, V., Tyagi, H., Hordy, N., Otanicar, T.P., Hewakuruppu, Y., Modi, P. and Taylor, R.A., 2014. Harvesting solar thermal energy through nanofluid-based volumetric absorption systems. *International Journal of Heat and Mass Transfer*, *77*, pp.377-384.

[33]. Khullar, V., Tyagi, H., Otanicar, T.P., Hewakuruppu, Y.L. and Taylor, R.A., 2018a. Solar selective volumetric receivers for harnessing solar thermal energy. *Journal of Heat Transfer*, *140*(6), p.062702.

[34]. Khullar, V., Mahendra, P. and Mittal, M., 2018b. Applicability of heat mirrors in reducing thermal losses in concentrating solar collectors. *Journal of Thermal Science and Engineering Applications*, *10*(6), p.061004.

[35]. Kim, D. M., and R. Viskanta. "Effect of wall conduction and radiation on natural convection in a rectangular cavity." *Numerical Heat Transfer* 7, no. 4 (1984): 449-470.

[36]. Kimura, Shigeo, and Adrian Bejan. "The “heatline” visualization of convective heat transfer." (1983): 916-919.

[37]. Krishnamurti, Ruby. "Convection induced by selective absorption of radiation: a laboratory model of conditional instability." *Dynamics of atmospheres and oceans* 27, no. 1-4 (1998): 367-382.

[38]. Ladjevardi, S.M., Asnaghi, A., Izadkhast, P.S. and Kashani, A.H., 2013. Applicability of graphite nanofluids in direct solar energy absorption. *Solar Energy*, *94*, pp.327-334.

[39]. Larson, D. W., and R. Viskanta. "Transient combined laminar free convection and radiation in a rectangular enclosure." *Journal of Fluid Mechanics* 78, no. 1 (1976): 65-85.

[40]. Lee, S.H., Choi, T.J. and Jang, S.P., 2016. Thermal efficiency comparison: Surface-based solar receivers with conventional fluids and volumetric solar receivers with nanofluids. *Energy*, *115*, pp.404-417.

[41]. Lei, Chengwang, and John C. Patterson. "A direct stability analysis of a radiation-induced natural convection boundary layer in a shallow wedge." *Journal of Fluid Mechanics* 480 (2003): 161-184.

[42]. Lei, C., and J. C. Patterson. "Natural convection in a reservoir sidearm subject to solar radiation: experimental observations." *Experiments in Fluids* 32, no. 5 (2002a): 590-599.

[43]. Lei, Chengwang, and John C. Patterson. "Natural convection in a reservoir sidearm subject to solar radiation: a two-dimensional simulation." *Numerical Heat Transfer: Part A: Applications* 42, no. 1-2 (2002b): 13-32.

[44]. Lei, Chengwang, and John C. Patterson. "Unsteady natural convection in a triangular enclosure induced by absorption of radiation." *Journal of Fluid Mechanics* 460 (2002c): 181-209.

[45]. Lenert, A., 2010. *Nanofluid-based receivers for high-temperature, high-flux direct solar collectors* (Masters dissertation, Massachusetts Institute of Technology).

[46]. Lenert, A. and Wang, E.N., 2012. Optimization of nanofluid volumetric receivers for solar thermal energy conversion. *Solar Energy*, *86*(1), pp.253-265.

[47]. Lepot, Simon, Sébastien Aumaître, and Basile Gallet. "Radiative heating achieves the ultimate regime of thermal convection." *Proceedings of the National Academy of Sciences* 115.36 (2018): 8937-8941.

[48]. Liu, Xing, et al. "Volumetric solar steam generation enhanced by reduced graphene oxide nanofluid." *Applied Energy* 220 (2018): 302-312.

[49]. Mao, Yadan, Chengwang Lei, and John C. Patterson. "Unsteady natural convection in a triangular enclosure induced by absorption of radiation–a revisit by improved scaling analysis." *Journal of Fluid Mechanics* 622 (2009): 75-102.

[50]. Maron, N., 1990. Optical properties of fine amorphous carbon grains in the infrared region. *Astrophysics and Space Science*, *172*(1), pp.21-28.

[51]. Minea, A.A. and El-Maghlany, W.M., 2018. Influence of hybrid nanofluids on the performance of parabolic trough collectors in solar thermal systems: recent findings and numerical comparison. *Renewable energy*, *120*, pp.350-364.

[52]. Modest, Michael F., and Sandip Mazumder. *Radiative heat transfer*. Academic press, 2021.

[53]. Modest, M. F., and F. H. Azad. "The influence and treatment of Mie-anisotropic scattering in radiative heat transfer." (1980): 92-98.

[54]. Moroni, M., and A. Cenedese. "Penetrative convection in stratified fluids: velocity and temperature measurements." *Nonlinear processes in Geophysics* 13, no. 3 (2006): 353-363.

[55]. Mukhopadhyay, Achintya, Xiao Qin, Suresh K. Aggarwal, and Ishwar K. Puri. "On extension of “heatline” and “massline” concepts to reacting flows through use of conserved scalars." *ASME J of Heat Transfer-Transactions of the ASME* 124, no. 4 (2002): 791-799.

[56]. Onyegegbu, S. O. "Solar radiation induced natural convection in stagnant water layers." *Energy conversion and management* 30, no. 2 (1990): 91-100.

[57]. Kazaz, Oguzhan, et al. "Heat transfer characteristics of fluids containing paraffin core-metallic shell nanoencapsulated phase change materials for advanced thermal energy conversion and storage applications." *Journal of Molecular Liquids* (2023): 122385.

[58]. O’Keeffe, G.J., Mitchell, S.L., Myers, T.G. and Cregan, V., 2018. Modelling the efficiency of a nanofluid-based direct absorption parabolic trough solar collector. *Solar Energy*, *159*, pp.44-54.

[59]. Otanicar, T.P., Phelan, P.E., Prasher, R.S., Rosengarten, G. and Taylor, R.A., 2010. Nanofluid-based direct absorption solar collector. *Journal of renewable and sustainable energy*, *2*(3), p.033102.

[60]. Pordanjani, Ahmad Hajatzadeh, et al. "Nanofluids: Physical phenomena, applications in thermal systems and the environment effects-a critical review." *Journal of Cleaner Production* 320 (2021): 128573.

[61]. Price, H., Lu¨ pfert, E., Kearney, D., Zarza, E., Cohen, G., Gee, R. and Mahoney, R., 2002. Advances in parabolic trough solar power technology. *J. Sol. Energy Eng.*, *124*(2), pp.109-125.

[62]. Ravi, M. R., R. A. W. M. Henkes, and C. J. Hoogendoorn. "On the high-Rayleigh-number structure of steady laminar natural-convection flow in a square enclosure." *Journal of Fluid Mechanics* 262 (1994): 325-351.

[63]. Ryhming, Inge L. "Radiative transfer between two concentric spheres separated by an absorbing and emitting gas." *International Journal of Heat and Mass Transfer* 9.4 (1966): 315-324.

[64]. Rose, B. A. J., et al. "Investigations into nanofluids as direct solar radiation collectors." *Solar Energy* 147 (2017): 426-431.

[65]. Rapp, Bastian E. "Chapter 9-fluids." *Microfluidics: Modelling, mechanics and mathematics* s 243 (2017): 263.

[66]. Rubin, M., 1985. Optical properties of soda lime silica glasses. *Solar energy materials*, *12*(4), pp.275-288.

[67]. Saidur, R., Meng, T.C., Said, Z., Hasanuzzaman, M. and Kamyar, A., 2012. Evaluation of the effect of nanofluid-based absorbers on direct solar collector. *International Journal of Heat and Mass Transfer*, *55*(21-22), pp.5899-5907.

[68]. Sharaf, O.Z., Al-Khateeb, A.N., Kyritsis, D.C. and Abu-Nada, E., 2018a. Direct absorption solar collector (DASC) modeling and simulation using a novel Eulerian-Lagrangian hybrid approach: Optical, thermal, and hydrodynamic interactions. *Applied energy*, *231*, pp.1132-1145.

[69]. Sharaf, O.Z., Kyritsis, D.C. and Abu-Nada, E., 2018b. Impact of nanofluids, radiation spectrum, and hydrodynamics on the performance of direct absorption solar collectors. *Energy conversion and management*, *156*, pp.706-722.

[70]. Sharaf, O.Z., Kyritsis, D.C., Al-Khateeb, A.N. and Abu-Nada, E., 2018c. Effect of bottom surface optical boundary conditions on nanofluid-based DASC: Parametric study and optimization. *Solar Energy*, *164*, pp.210-223.

[71]. Sharaf, Omar Z., et al. "Ultrastable plasmonic nanofluids in optimized direct absorption solar collectors." *Energy Conversion and Management* 199 (2019): 112010.

[72]. Sharaf, O.Z., Taylor, R.A. and Abu-Nada, E., 2020. On the colloidal and chemical stability of solar nanofluids: From nanoscale interactions to recent advances. *Physics Reports*.

[73]. Singh, Apoorva, Manish Kumar, and Vikrant Khullar. "Comprehensive modeling, simulation and analysis of nanoparticles laden volumetric absorption based concentrating solar thermal systems in laminar flow regime." *Solar energy* 211 (2020): 31-54.

[74]. Singh, Apoorva, Manish Kumar, and Vikrant Khullar. "An investigation into the thermo-fluid behavior of volumetrically heated cavities irradiated from the side." *International Journal of Thermal Sciences* 192 (2023): 108420.

[75]. Singh, Inderpreet, Satbir Singh Sehgal, and Vikrant Khullar. "Nanofluid Filled Enclosures: Potential Photo-thermal Energy Conversion and Sensible Heat Storage Devices." *arXiv preprint arXiv:2203.06602* (2022).

[76]. Singh, Inderpreet, Satbir Singh Sehgal, and Vikrant Khullar. "Modeling and analysis of heat transfer and fluid flow mechanisms in nanofluid filled enclosures irradiated from below." *International Journal of Thermal Sciences* 183 (2023): 107852.

[77]. Singh, N. and Khullar, V., 2019. Efficient Volumetric Absorption Solar Thermal Platforms Employing Thermally Stable-Solar Selective Nanofluids Engineered from Used Engine Oil. *Scientific reports*, *9*(1), pp.1-12.

[78]. Singh, Nirmal, and Vikrant Khullar. "Experimental and theoretical investigation into effectiveness of ZnO based transparent heat mirror covers in mitigating thermal losses in volumetric absorption based solar thermal systems." *Solar Energy* 253 (2023): 439-452.

[79]. Sparrow, E. M., C. M. Usiskin, and H. A. Hubbard. "Radiation heat transfer in a spherical enclosure containing a participating, heat-generating gas." (1961): 199-206.

[80]. Stagg, B.J. and Charalampopoulos, T.T., 1993. Refractive indices of pyrolytic graphite, amorphous carbon, and flame soot in the temperature range 25 to 600 C. *Combustion and flame*, *94*(4), pp.381-396.

[81]. Tao, Wen-Quan, Ya-Ling He, and Lei Chen. "A comprehensive review and comparison on heatline concept and field synergy principle." *International Journal of Heat and Mass Transfer* 135 (2019): 436-459.

[82]. Taylor, R.A., Phelan, P.E., Otanicar, T.P., Walker, C.A., Nguyen, M., Trimble, S. and Prasher, R., 2011. Applicability of nanofluids in high flux solar collectors. *Journal of Renewable and Sustainable Energy*, *3*(2), p.023104.

[83]. Tyagi, H., Phelan, P. and Prasher, R., 2009. Predicted efficiency of a low-temperature nanofluid-based direct absorption solar collector. *Journal of solar energy engineering*, *131*(4), p.041004.

[84]. Veeraragavan, A., Lenert, A., Yilbas, B., Al-Dini, S. and Wang, E.N., 2012. Analytical model for the design of volumetric solar flow receivers. *International Journal of Heat and Mass Transfer*, *55*(4), pp.556-564.

[85]. Verevochkin, Yu G., and S. A. Startsev. "Numerical simulation of convection and heat transfer in water absorbing solar radiation." *Journal of Fluid Mechanics* 421 (2000): 293-305.

[86]. Wang, Kongxiang, Yan He, Zhiheng Zheng, Jingqiong Gao, Ankang Kan, Huaqing Xie, and Wei Yu. "Experimental optimization of nanofluids based direct absorption solar collector by optical boundary conditions." *Applied Thermal Engineering* 182 (2021): 116076.

[87]. Webb, B. W., and R. Viskanta. "Analysis of radiation-induced natural convection in rectangular enclosures." *Journal of Thermophysics and Heat Transfer* 1, no. 2 (1987): 146-153.

[88]. Webb, B. W., and R. Viskanta. "Radiation-induced buoyancy-driven flow in rectangular enclosures: experiment and analysis." (1987): 427-433.

[89]. Wu, Hongbo, Runsheng Tang, Zhimin Li, and Hao Zhong. "A mathematical procedure to estimate solar absorptance of shallow water ponds." *Energy conversion and management* 50, no. 7 (2009): 1828-1833.

[90]. Zhao, Lin, et al. "Harnessing heat beyond 200 C from unconcentrated sunlight with nonevacuated transparent aerogels." *ACS nano* 13.7 (2019): 7508-7516.

List of Publications

Published in peer reviewed (SCI) journals:

1) Singh, Apoorva, Manish Kumar, and Vikrant Khullar. "Comprehensive modeling, simulation and analysis of nanoparticles laden volumetric absorption based concentrating solar thermal systems in laminar flow regime." *Solar Energy* 211 (2020): 31-54.

2) Singh, Apoorva, Manish Kumar, and Vikrant Khullar. "An investigation into the thermo-fluid behavior of volumetrically heated cavities irradiated from the side." *International Journal of Thermal Sciences* 192 (2023): 108420.

To be communicated

3) Singh, Apoorva, Manish Kumar, and Vikrant Khullar. " Parametric investigation into Rayleigh Benard convection induced by volumetric heating."